

**WASM: Minerals, Energy and Chemical Engineering**

**Assessment of Archie Parameters in Shale: An Experimental Approach**

**Zhiqi Zhong**

**This thesis is presented for the Degree of**

**Doctor of Philosophy**

**of**

**Curtin University**

**May 2021**

# Declarations

To the best of my knowledge and belief, this thesis contains no material previously published by any other person except where due acknowledgment has been made.

This thesis contains no material which has been accepted for the award of any other degree or diploma in any university.

Signature: \_\_\_\_\_

Date: \_\_\_\_\_

---

# Abstract

Unconventional resources such as shale gas have attracted attention worldwide. Understanding the rock electrical-controlling factors is critical for well-log interpretation in shale formations. However, formation electrical models applying on the well-log interpretation for conventional reservoirs have proven not accurately transferable for shale formations due to the inaccurate selection of Archie's parameters. Although Archie's parameters (e.g, cementation exponent,  $m$ ) have been established for typical reservoirs such as clean sandstone and carbonate, only limited studies have been conducted on shale due to its complex conductive mechanism and pore structure.

This study aims to derive the Archie cementation exponent,  $m$ , its pressure sensitivity, and its pore water salinity influences in shale from the experimental works. Three main aspects are considered (1) shale petrophysical properties, including mineralogical composition, total organic carbon content, and pore structure characterization; (2) excessive conductivity arising from the strong Cation Exchange Capacity (CEC) property of clays' particle surface; (3) changes of petrophysical properties and excessive conductivity under various external factors including confining pressure and pore water salinity.

Shale samples in this study are from Canning and Cooper Basin, Australia; and Western Gulf Basin, America. After cleaning, the studied shale samples were fully saturated under hydrostatic pressure with brine with different salinity before conducting electrical resistivity and nuclear magnetic resonance (NMR) measurements. The resistivity measurements at 1kHz were conducted under ambient and reservoir conditions. NMR was measured to obtain the total and effective porosity (excluding clay-bound water volume), pore size distribution (PSD), and to detect the presence of any residual oil after the cleaning process.

The Archie's cementation exponent,  $m$ , for shale was determined under 250g/l pore water salinity, where the influences of clay particles on the surface conductivity can be neglected. The Archie's  $m$  was found to be a pressure-sensitive parameter in shale due to its compliant pore nature. Archie's  $m$ , porosity, and electrical resistivity show similar variation trends at different confining pressure, resulting from the closure of microfractures at 500 psi; the narrowing of mesopores/macropores at 500–3500 psi; and some limited changes due to pore-throat reduction beyond 3500 psi. This finding was supported by the observation of characteristic frequency under the increasing pressure based on the POLARIS model.

---

Furthermore, the non-monotonical increment of Archie's  $m$  under increasing pore water conductivity suggests a minor effect of CEC on Archie's  $m$  for shale. The phenomenon can be explained by the volume averaging approach as the strong local electrical field within the pore throat while negligible in the dead-ends at high salinity cases, and uniform dispersion of the local electrical field at low salinity cases with a less significance of surface conductivity.

In conclusion, this study introduces that the shale's pressure-sensitive cementation exponent can be calculated at different confining stress,  $p$ , by equation  $m_p = (2.483)P^{0.011}$ . The calculated cementation exponent is positively correlated to the proportion of meso/macropores and negatively correlated to quartz content. This study provides recommended experimental procedures for the acquisition of Archie's  $m$ , leading to improved accuracy for water saturation calculation from well-logs for shale reservoirs.

---

## Acknowledgments

This Ph.D. journey has been the most challenging, exciting, and life-changing experience for me. I could never finish this journey without those people who guide me, help me, support me, encourage me, and care about me.

First of all, I would like to express my most sincere gratitude to my supervisor Prof. Reza Rezaee. Back in 2017, I was so confused at the crossroad of my life after Master graduation and reluctant to live a life that was so predictable within the future 30 years. I appreciate the opportunity you offered me to change my life. As a supervisor, you tolerate my mistakes, teach me critical thinkings, build my academic skills, provide me suggestions, lead my way and correct my study directions. As more than a supervisor, your carings and helps for both me and my wife were our biggest supports to get over our hardest time during the Covid-19 when our baby was born. I also want to thank my co-supervisor Dr. Mohammad Sarmadivaleh for the tutorial of experimental apparatus in my earlier Ph.D. stages. Thanks to my co-supervisor Dr. Matthew Josh, who spent lots of time on sample preparation and academic discussion with me. Thanks to Dr. Esteban Lionel for the tutorials of all the available experimental apparatus, the convenience for the experiments, and the side-by-side editing of my first paper leading me to a better understanding of paper drafting. Thank you, Dr. Sam Xie, for sharing the helpful writing experience for the research.

Special thanks to my friends from Unconventional Gas Research Group (UGRG): Dr. Hongcai Wang, Dr. Jie Zou, Dr. Yujie Yuan, Dr. Jamiu Ekundayo, Dr. Lukman Johnson, Mr. Xuekai Li, Mr. Muhammad Atif Iqbal, and Mr. Partha Pratim Mandal. Thank you Hongcai and Jie for acting as a bigger brother guides me on academic aspects and supports me in daily life. Thank you Yujie for your tutorial on NMR and your information helped me meet Eminem. Thank you, Atif, for the cooperation on the topic. I enjoy the day we worked together. I appreciate Xuekai for your lifelong advice, Partha for your kindness in sharing your experimental results, Lukman and Jamiu for your help on Rock-eval and Python. I would like to extend my thanks to my colleagues. Mr. Gonzalo Mauricio Ceron Lopez, thank you for your help on the experiment and the friendly jokes. Dr. Liming Qin for the help on well-log interpretation and life experiences. Thank your Dr. Lingping Zeng, Dr. Yongqiang Chen, Mr. Runhua Feng, Miss. Shuo Liu, Mr. Kaishuo yang for the help from work and happiness from everyday life.

---

I would like to acknowledge my other friends for sharing the wonderful time during my Ph.D. in no particular order: Xingguang Xu, Shican Liu, Tongcheng Han, Yunhu Lu, Zhengyangzi Wang, Wei Tan, Panfeng Liu, Fuping Li, Yubing Liu, Jiabin Liang, Wenshuai Li, Yihuai Zhang, Yang Yang, Zhikun Su, Zixing Qin, Guanghan Chu, Yuqing Chen, Pei Li, Jiang Jia, Yadong Zhang, Emad Al-Khdheawi, Eghan Arjomand, Mohsen Ghasemi, Cut Aja Fauziah, Ruby Lo, Surudee Bunpitakgate, Nichole Sik, Junfang Zhang, Chengrui-Star Zhang, Qixu-Bh Yuan, Ning Ye, Yunfeng Zhang, Yiru Zhao, Michael Verrall, Kui Tong, Ruixue Wang, Faaiz Al-Shajalee, Kai Wang, Le Liang, Siqi Chen.

Last but not least, I would like to express my thanks to my wife Minzhen Li, who sacrificed her study and precious time to be with our son. Thanks to my parents and relatives for the emotional supports. Special thanks to Dr. Vivienne Cass, for treating our boy like your own. Thanks for the time you spend with us when nobody was around to help.

---

# Table of contents

Declarations.....	ii
Abstract .....	iii
Acknowledgments.....	v
Table of contents .....	vii
List of Figures .....	x
List of Tables.....	xiv
List of Publications .....	xv
Chapter 1 Introduction .....	1
1.1 Significance and motivation.....	2
1.2 Thesis objectives .....	6
1.3 Structure of the thesis .....	6
Chapter 2 Sample characteristics and methods.....	9
2.2 Samples and sample preparations .....	10
2.2.1 Sample characteristics .....	10
2.2.2 Sample preparation.....	10
2.2.3 Pore water selections.....	12
2.3 Methods.....	13
2.3.1 Saturation procedure .....	13
2.3.2 Nuclear magnetic resonance (NMR).....	14
2.3.3 Impedance measurement .....	16
2.3.4 Rock-eval pyrolysis.....	18
2.3.5 Electrical models .....	19
Chapter 3 Determination of Archie’s cementation exponent for shale reservoirs .....	22
3.1 Introduction .....	23
3.2 Methodology .....	23
3.3. Results .....	25
3.3.1 NMR porosity analysis.....	25
3.3.2 NMR $T_1$ - $T_2$ Spectrum of oil signature .....	28
3.3.3 Resistivity and Archie’s parameter calculation in ambient and reservoir conditions .....	29
3.4 Discussion .....	31

---

3.4.1 Influence of residual oil.....	31
3.4.2 Influence of induced fractures.....	31
3.4.3 Influence of clay-bound water.....	32
3.4.4 Variation of Archie's parameter $m$ .....	33
3.5 Conclusion.....	36
Chapter 4 The pressure dependence of Archie's cementation exponent for shale reservoirs.....	37
4.1 Introduction.....	38
4.2 Methodology.....	39
4.2.1 Samples preparation and experimental procedure.....	39
4.2.2 Effective porosity calculation.....	40
4.2.3 POLARIS model.....	41
4.3 Results.....	42
4.3.1 Sample weight monitoring under pressure.....	42
4.3.2 NMR and saturation porosity.....	43
4.3.3 Pore size distribution variation under different confining pressure.....	45
4.3.4 NMR $T_1T_2$ spectrum for residual oil detection.....	46
4.3.5 Resistivity and formation factor stress sensitivity.....	47
4.4 Discussion.....	50
4.4.1 Effective porosity from saturation and NMR methods.....	50
4.4.2 Pore size distribution variation under different pressure.....	50
4.4.3 Stress sensitivity of resistivity.....	52
4.5 Conclusion.....	56
Chapter 5 The salinity dependence of electrical conductivity and Archie's cementation exponent for shale.....	57
5.1 Introduction.....	58
5.2 Volume averaging approach theory.....	59
5.3 Methodology.....	62
5.4. Results.....	63
5.4.1 Effective porosity calculation.....	63
5.4.2 Nuclear magnetic resonance (NMR).....	64
5.4.3 Electrical conductivity and apparent formation factor.....	64
5.5 Discussion.....	66
5.5.1 The variation of electrical conductivity at different salinities.....	66
5.5.2 The variation of apparent formation factor at different salinities.....	68

---

5.5.3 The variation of Archie's cementation exponent $m$ at different salinities ....	69
5.5.4 Limitations .....	72
5.6 Conclusion.....	73
Chapter 6 Application for Archie cementation exponent in well-log interpretations of shale reservoirs .....	74
6.1 Introduction .....	75
6.2 Results .....	76
6.2.1 Shale composition .....	76
6.2.2 Resistivity, formation factor, and Archie's cementation exponent.....	76
6.2.3 Pore-size distribution (PSD).....	78
6.3 Discussion and conclusion .....	79
6.3.1 Effects of shale composition on Archie's cementation exponent .....	79
6.3.2 Effects of PSD on Archie's cementation exponent.....	80
6.3.3 Total porosity and effective porosity based cementation exponent .....	82
6.3.4 Water saturation (SW) calculation .....	84
Chapter 7 Conclusion.....	86
7.1 Conclusions of studies.....	87
7.2 Recommendations for future research.....	90
References .....	92
Appendix .....	101

---

## List of Figures

<b>Figure 1.1</b> Electrical conductivity and resistivity of common rocks (adapted from <a href="https://em.geosci.xyz">https://em.geosci.xyz</a> ).....	3
<b>Figure 2.1</b> Example of weight changes as a function of time from the sample Th24 during 49 days under 2000 psi brine exposure. All the tested samples reached their maximum saturation during the first week. ....	14
<b>Figure 2.2</b> A-Resistance measurement rig for the ambient condition; B-Resistance measurement rig for reservoir condition .....	17
<b>Figure 2.3</b> The resistivity variation with time for the sample Th45 under 2800 psi confining pressure.....	18
<b>Figure 2.4</b> Variation of $F_a/F$ with $R_w$ for four specified values of $Q_v$ (in equiv litre-1), according to the hypothetical petrophysical model (Worthington, 1993). ....	21
<b>Figure 3.1</b> CEC of Calcigel® as measured by the Cu-trien method. NaCl (wt%) is the solid content of NaCl in the Calcigel®/NaCl mixture. The theoretical decrease in CEC represents a decrease in the CEC based on the diluted weight of bentonite (Bohác et al., 2019). ....	24
<b>Figure 3.2</b> Experimental flow chart for porosity and electrical resistivity measurement .....	25
<b>Figure 3.3</b> NMR porosity and pore size distribution of the shales collection under ambient conditions after brine saturation. Th23 (light blue) and Th40 (dark orange) are uncleaned oil-shales while the other Theia#1 samples are oil-cleaned NMR data. ....	26
<b>Figure 3.4</b> Example of NMR porosity and pore size distribution under room conditions (blue curve) and 2800 psi confining pressure (orange curve) for the oil-cleaned shale Th24 brine saturated...	27
<b>Figure 3.5</b> NMR $T_1$ - $T_2$ spectrum of the uncleaned sample, Th23, and cleaned sample, Th39. ....	29
<b>Figure 3.6</b> Simplified schematic of electrical charges distribution on the clay mineral surface and pore channel: A-Diffuse double layer of water molecules at the smectite surface (McPhee et al., 2015); B-Conductance path and clay ion mobility in shale pore channel.....	33
<b>Figure 3.7</b> Formation factor relationship with effective porosity on Theia#1 (circle symbols) and Encounter#1 (square symbols) saturated shales collection under ambient and reservoir conditions. Forcing log-log fit line intercepts y-axis at effective porosity =1 and $F=1$ for both ambient and reservoir conditions. Due to the existence of residual oil in Th23 detected from NMR $T_1$ $T_2$ mapping, this sample (grey circle) is excluded from the fitting curve. The Grey dashed line represents the average $m$ from Theia#1 oil shales and the black dashed line presents the average $m$ from	

---

Encounter#1 gas shales. The apparent averaged Archie's $m$ from the whole shales collection (black line) is calculated at 2.48 and 2.70 under ambient and reservoir conditions respectively. ....	35
<b>Figure 4.1</b> Sample normalised weight monitoring under increasing confining pressures in Group 1 up to 8500 psi. The black curves correspond to a power-law fitting of the data. ....	43
<b>Figure 4.2</b> Comparison of effective porosity between NMR and saturation methods at ambient conditions for Group 1 samples after undergoing confining pressure experiments (i.e. brine expelled from shale compaction/creep).....	44
<b>Figure 4.3</b> NMR $T_2$ spectrum of Group 1 samples (Th24, Th25) measured under ambient conditions after undergoing different confining pressures.....	45
<b>Figure 4.4</b> NMR $T_2$ spectrum of Group 2 samples (Th17, Th23, Th28) measured under ambient conditions on saturated state and after 8500 confining pressure.....	46
<b>Figure 4.5</b> NMR T1-T2 spectrum of the Left) uncleaned sample, Th17, and Right) cleaned sample, Th28. The circled area in the Th17 NMR T1-T2 spectrum exhibits a weak signal relating to the presence of residual oil which is not apparent for sample Th28.....	47
<b>Figure 4.6</b> Electrical impedance results under confining pressure in Group 2 samples: (A) Reactance spectrum under different confining pressure; (B) Mean characteristic frequency under different confining pressures.....	48
<b>Figure 4.7</b> Resistivity and formation factor under increasing confining pressure for all tested samples. Tested samples show similar variation trends with a rapid increase under low pressure and slower changes under higher confining pressure.....	49
<b>Figure 4.8</b> Normalized resistivity under different confining pressure. There is a monotonic increase in normalized resistivity with increasing confining pressure. The increase in normalized resistivity occurs rapidly from 0–500 psi confining pressure but then the rate of increase is less from 500–8500 psi. ....	53
<b>Figure 4.9</b> Archie cementation exponent $m$ under increasing confining pressure for cleaned samples (no residual oil). The increase in cementation exponent $m$ is rapid from 0–500 psi confining pressure but then the rate of increase is less from 500–8500 psi.....	54
<b>Figure 5.1</b> The non-linear behavior between the conductivity of saturated cores and its pore water. The dashed line is the extension of the asymptotic line at high salinities called Archie's line in this paper. The tested data below Archie's line. Data from Waxman and Smits (1968).....	61
<b>Figure 5.2</b> A-Normalised potential $Ib$ distribution under high salinity conditions. The local electrical field is strong within the pore throat while negligible in the dead-ends; B-Normalised potential $I_s$ distribution under low salinity conditions. Figures from (Revil et al., 2018a) .....	61

<b>Figure 5.3</b> Pore-size distribution by NMR $T_2$ spectrum for the studied samples.....	64
<b>Figure 5.4</b> The electrical conductivity of saturated samples $C_0$ (S/m) at different pore water salinity $C_w$ (S/m). The sample conductivity increases monotonically with increasing pore-water conductivity for all of the samples, and in some cases (Th24, and Th25) the relationship is more rapid as the pore water conductivity increases from 5–7 S/m but rolls off at higher pore-water conductivity.....	66
<b>Figure 5.5</b> The calculated apparent formation factor $F_a$ (unitless) under different pore water conductivity, $C_w$ (S/m). The samples typically exhibit two distinct conduction regimes. In the vicinity of $C_w = \sim 7\text{--}10\text{S/m}$ , the relationship between the Apparent formation factor and the Pore-water conductivity transition from a decreasing relationship to an increasing relationship. For each sample, the transition occurs at a different pore water conductivity. For sample EF1 this transition occurs at $C_w = 10$ S/m (relatively high) and for Th39 it is not apparent within the measurement range.....	67
<b>Figure 5.6</b> The variation of Archie’s cementation exponent at different pore water salinity. Archies cementation exponent $m$ is decreasing with increasing pore-water salinity up to a transition value of typically $C_w = 7\text{--}10$ S/m, above which $m$ is monotonically increasing with increasing pore water conductivity. The transition value of $C_w$ is different for each sample, but the Eagle Ford sample, EF1 exhibits the highest transition $C_w$ of $\sim 10$ S/m. The expected relationship between cementation exponent and pore-water conductivity should be monotonically increasing (similar to the red line presented) if the presence of CEC associated with clays were in fact the dominating the bulk conduction. ....	71
<b>Figure 6.1</b> The pore-size distribution by NMR. ....	77
<b>Figure 6.2</b> The calculated proportion of micropores (<1 ms), mesopores (1–20 ms), and macropores(20–100 ms) defined by NMR.....	78
<b>Figure 6.3</b> Correlations between A-quartz proportion and Archie’s $m$ ; B-total clay proportion and Archie’s $m$ ; C-illite proportion and Archie’s $m$ ; D-TOC and Archie’s $m$ . Set A includes samples Th24, Th25, Th37D, Th39D, Th40 (black square and black dashed line). Set B is for samples Th45, En4441, En4455, En4457 (grey square and grey dashed line). ....	80
<b>Figure 6.4</b> Correlations between the proportion of micropores, mesopores and macropores with Archie’s $m$ . ....	81
<b>Figure 6.5</b> The Archie cementation exponent derived based on total porosities shows higher values than those calculated by effective porosities in Figure 4.9. Either of these calculated $m$ values can	

---

be used depending on what type of porosity (total or effective) has been used for the water saturation calculation.....83

**Figure 6.6** The water saturation calculation by applying Archie cementation exponent on Simandoux and Waxman & Smits equations. The water saturation prediction of the Simandoux equation fits the measured water saturation from lab work (yellow dots). .....85

---

## List of Tables

<b>Table 2.1</b> Studied shale sample characteristics .....	11
<b>Table 2.2</b> XRD composition of the studied shale samples .....	12
<b>Table 3.1</b> NMR porosity (in %) summary from the sample collection. Comparison between whole porosity at maximum saturation and matrix porosity (i.e. without microfracture signal at $T_2 > 100\text{ms}$ ).....	28
<b>Table 3.2</b> Summary of formation factor, resistivity and Archie's cementation exponent $m$ for the Theia#1 and Encounter#1 shales in ambient and reservoir conditions. Archie's $m$ was computed from two methods: * from $a = 1$ in equation 2.2; and ** from $F-\Phi$ log-log plot by refining the trendline by the point ( $\log F = \log \Phi = 1$ ). Formation water resistivity ( $R_w$ ) for all samples is 0.042 ohm-m. Data on samples Th37 & Th39 are not available (NA) due to damage.....	30
<b>Table 4.1</b> Sample dimensions, weights at dry and saturated states, and calculated porosity considering brine density of 1.145 g/cc. ....	42
<b>Table 4.2</b> Effective porosity ( $\Phi$ ) using NMR and saturation methods on the shale collection. ....	44
<b>Table 5.1</b> Shale mineralogy .....	63
<b>Table 5.2</b> Dimensions, weight, and saturation porosity of the studied samples.....	63
<b>Table 5.3</b> Summary of resistivity and apparent formation factor for samples saturated with different pore water salinities. Eagle Ford sample presents higher resistivity and correspondingly apparent formation factor than other samples.....	65
<b>Table 5.4</b> Calculated Archie's cementation exponent .....	71
<b>Table 6.1</b> Rock-eval data for tested samples .....	76
<b>Table 6.2</b> The resistivity, Formation Factor and Archie's cementation exponent at 250,000 ppm NaCl under 2800 psi confining pressure .....	77

# List of Publications

(Publications forming parts of the thesis as standalone chapters)

## Chapter 3

**Zhiqi Zhong**, Reza Rezaee, Lionel Esteban, Matthew Josh, Runhua Feng, Determination of Archie's cementation exponent for shale reservoirs; an experimental approach, Journal of Petroleum Science and Engineering, Volume 201, 2021, 108527, ISSN 0920-4105

## Chapter 4

**Zhiqi Zhong**, Lionel Esteban, Reza Rezaee, Matthew Josh, Runhua Feng, The Pressure Dependence of the Archie Cementation Exponent for Samples from the Ordovician Goldwyer Shale Formation in Australia, SPE Journal, SPE-J1-11

## Chapter 5

**Zhiqi Zhong**, Reza Rezaee, Matthew Josh, Lionel Esteban, Mohammad Sarmadivaleh, The salinity dependence of Archie's cementation exponent for shale reservoirs. Journal of Petroleum Science and Engineering, Under Review.

---

# **Chapter 1**

## **Introduction**

---

---

## 1.1 Significance and motivation

The last few decades have witnessed a boom in fossil fuel exploration worldwide and its promotion as part of the rapid development of the global industrial economy ([Musa et al., 2018](#)). However, the consumption of fossil fuel to meet the demand of the human being's everyday life is limited by its non-renewable nature. Additionally, the usage of fossil fuels causes severe global warming problems and poses threats to human society ([Wang et al., 2018](#)). Given this, many countries have begun to explore unconventional resources, with shale gas believed to be among the most environmentally friendly ([Rezaee, 2015](#); [Sohag et al., 2019](#)). The influence of shale gas has increased markedly since the successful exploitation in the United States in around 2006 ([McGlade et al., 2013](#)), since when other countries (e.g., Canada, Australia, China) have launched their own shale gas exploration initiatives.

To better support shale reservoir evaluation, petrophysical research is needed to describe the relationships between geophysical observations (electrical resistivity, elastic velocity, gamma-ray signals, etc.) and the subsurface reservoir properties of rocks (lithology, porosity, permeability, pore pressure, pore fluid saturation and types, temperature, etc.). Well-logging and laboratory measurements are the two main methods of investigation. Well-logging data can be used to predict geophysical properties through petrophysical modelling, while laboratory measurements directly provide the petrophysical information from the experiments. Well-logging data indicate the averaged reservoir information on a large scale, sometimes with the mixed lithological layers (i.e., laminated shale sandwiched within the sandstone) ([Ellis and Singer, 2007](#)). Therefore, in some cases, accurate prediction of petrophysical parameters from well-logging is difficult. In contrast, laboratory measurement avoids this difficulty by selecting small samples with defined lithology. These laboratory measurements provide precise petrophysical properties for particular rock types, support the investigation of rock petrophysical mechanism and eventually point the way to validate existing models from one rock type for others and to form new applicable models.

As a common petrophysical parameter recorded in well-logs, resistivity in shale is more complex than resistivity in clean formations. Shale resistivity is strongly associated with the mineral component, brine concentration, and distribution of clay minerals in the rock ([Doveton, 2014](#); [Kadkhodaie and Rezaee, 2016](#); [Kennedy and Herrick, 2012](#); [Ramirez, 1990](#); [Silva et al., 2018](#); [Yue and Tao, 2013](#)). Figure 1.1 shows the electrical resistivities and conductivities of common rock types. Clays and shales demonstrate lower electrical resistivity than sands and sandstones. The

electrical property of rocks filled with saltwater alters as the pore spaces provide an electrically conductive channel (Wong et al., 1984). The first and the most commonly invoked research on rock resistivity to combine different petrophysical properties (porosity and fluids saturation) is Archie's equation (Archie, 1942). The input of Archie's equation includes the porosity, electrical resistivity of the pore water and saturated rock, and Archie's parameters relating to the structure of pore channels such as cementation exponent and tortuosity factor. Archie's equation has been accepted as an industry standard for determining water saturation in well-log interpretation. The original equation is for clay-free rocks and considers formation water as the only conducting medium in the rock. For clay-bearing formations, Archie-based equations are currently used in the industry – such as the Simandoux model (Simandoux, 1963), Indonesia model (Leveaux and Poupon, 1971), Fertl model (Fertl, 1975), dual water model (Clavier et al., 1984) are based on Archie's equation or utilise Archie's parameters in saturation models. The main reason for the development of these models is the reduced accuracy of Archie's equation in shaly formations due to excessive conductivity exerted by the presence of the clays.

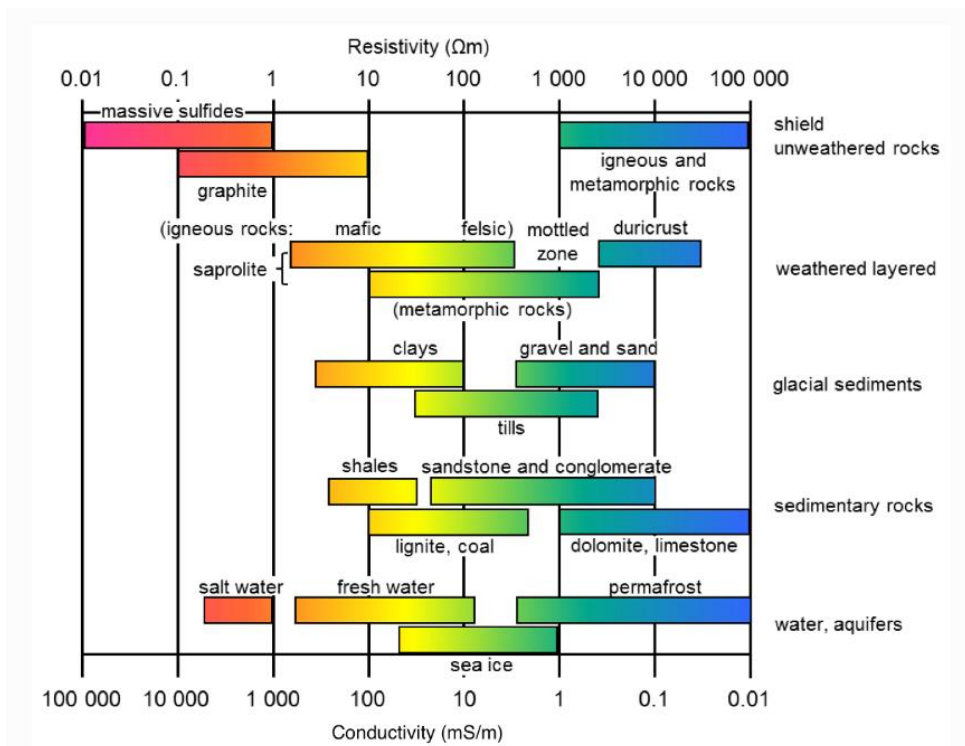


**Figure 1.1** Electrical conductivity and resistivity of common rocks (adapted from <https://em.geosci.xyz>)

The main uncertainty of Archie's equation for shale reservoirs relates to clay surface conductivity as a transport for electrons, on top of transport through the bulk pore fluid. Revil et al. (1998) argue

---

that pore fluid and fluid/grain interface are two channels for the rock conductivity and also suggest that three contributions characterise surface conductivity: (i) The conductivity of the electrical diffuse layer – the contribution of the diffuse layer to the total surface conductivity can usually be neglected; (ii) conduction of the Stern layer – the significance of the electrical conduction within the Stern layer is various at low salinities ( $10^{-6}$  to  $10^{-3}$  mol/L), but the conductivity of the Stern layer becomes independent of salinity at high salinity levels; and (iii) the mineral surface – the surfaces of the mineral are conductive channels, and this part of the contribution is also independent of salinity. Shaly sandstones are believed to have higher conductivity than clean sandstone ([Doveton, 2014](#); [Ramirez, 1990](#)), due to the free charges of clay minerals within the silica layers ([Ruhovets and Fertl, 1982](#)). This behaviour occurs due to the negative charges at the clay surfaces, which strongly attract water molecules and form an irreversible film – so-called clay-bound water (CBW). Additionally, the strong CEC of clays provides an extra increment in the overall surface conductivity ([Doveton, 2014](#)). CEC is defined to measure the ion adsorption capability of minerals and is also utilised to describe the conductivity of fluid/grain interface ([Carroll, 1959](#); [Clerke and Martin, 1994](#); [Fertl and Chilingarian, 1990](#); [Hendershot et al., 1993](#); [Worthington, 1985](#)). This electrical property is strongly related to the specific surface area (SSA) because a smaller size of grains leads to a larger amount of charges per unit mass of the grain surfaces ([Patchett, 1975](#)). Therefore, given the inherent larger size of quartz particles, the CEC of quartz is usually neglected in sandstone compared to the CEC of other, much smaller clay minerals, especially occurring in shales ([Ellis and Singer, 2007](#)). Thus, neglecting the CEC effect in shaly sandstones and shale cases leads to an underestimation of rock conductivity. Several formulas have been developed to describe the electrical contribution of CEC. The best-known modified Archie's formulas are the Waxman-Smits equation ([Waxman and Smits, 1968](#)) and the dual water saturation equation ([Clavier et al., 1984](#)). These equations include the parameter  $Q_v$  (CEC per unit pore volume) and have proven to have a higher log interpretation accuracy than the original Archie's equation in shaly-sandstone formations. The  $Q_v$  or CEC value is mostly obtained in the laboratory via various methods, including divalent cation electrodes ([Chiu et al., 1990](#)), methylene blue adsorption ([Kahr and Madsen, 1995](#)) and others. When the salinity of pore fluid is high enough, the pore fluid electrical conductivity becomes the dominant contribution ([Revil et al., 1998](#)). This means the electrical conductivity of the clay surface provided by the CEC effect is too small to be considered when the pore fluid salinity is high. However, the importance of clay particle, especially for its surface conductivity, to the shale electrical conductivity at normal formation water salinity (20,000ppm-30,000ppm) is still unknown.

---

Besides, the electrical property of clay particles, pyrite, and kerogen are important in shale conductivity. The organic-rich samples with higher TOC show higher resistivities, while samples with higher pyrite show lower resistivities regardless of their dispersion ([Xuben Wang et al., 2016](#)). [Wang et al. \(2017\)](#) tested the organic-rich shale samples from the nano/micro scales and discussed the contribution of pyrite and mature kerogen under different relative humidity situations. Up to date, the studies of the effect of shale components (except clay particles) are still limited.

In addition, the electrical contribution of different pore structures in shale is a very important subject. The relationship of the electrical property and rock pore structure could be described by the cementation exponent  $m$  (a dimensionless factor) in Archie's equation, which is believed to vary with the shape and size of grain particles for different rock types ([Friedman, 2005](#); [Jackson et al., 1978](#)). For the pore system, interconnect (effective) and isolated (ineffective) pores are classified as two main pore spaces within the sedimentary rocks. Pores are usually large and effective leading to high rock porosity and permeability in sandstone. While shale is defined as a fine-grained sedimentary rock formed from a mixture of clay-sized minerals (around 4  $\mu\text{m}$  in diameter) and silt-size particles, with low porosities, low permeability and very small pore sizes, with a wide range of pore size distribution ([Folk, 1974](#)). Pores in shale are less effective and can be divided into three main categories: micropores (< 2 nm), mesopores (2–50 nm), and macropores (> 50 nm) ([Rouquerol et al., 1994](#)). The characteristic of shale pore structure are currently investigated on several different methods including low-pressure  $\text{CO}_2$  adsorption to characterise the micropores ([Clarkson et al., 2013](#); [Scherdel et al., 2010](#)); low-pressure  $\text{N}_2$  adsorption to characterise the mesopores and macropores ([Labani et al., 2013](#)); mercury injection capillary pressure (MICP) to define the porosity of interconnected pores for pore size 3.6 nm–1 mm ([Comisky et al., 2011](#); [Sen Wang et al., 2016](#)); and nuclear magnetic resonance (NMR) to detect the total water signals in tested samples and how they are distributed within pores ([Al Hinai et al., 2014](#); [Dillinger and Esteban, 2014](#); [Rezaee et al., 2012](#)). Microscopy techniques, for example, transmission electron microscopy (TEM) and scanning electron microscopy (SEM), are practical methods for pore channel observation, petrographic analysis and porosity estimation ([Sigal, 2015](#)). The pore structure and pore size distribution have been widely investigated for shale, however, only limited studies joint the shale electrical property with its pore structure characteristics.

External factors such as pressure and temperature can also affect the electrical property. Temperature reduces electrical resistivity by accelerating the electron transfer of the electrolyte instead of the rock matrix ([Nottenburg et al., 1979](#)), indicating the temperature effects on the shale electrical property should be the same as that on sandstone. As to the pressure influences, shale resistivity

---

increases with increasing confining pressure due to the closure of cracks ([Johnston, 1987](#); [Wallace, 1965](#)), while the changes in resistivity observed are less than those for sandstones of similar porosities ([Yale, 1984](#)). The closure of cracks and narrowing of pores for shale under the pressure is not necessarily to be the same as sandstone due to the compliant nature of clay particles, while this has been only limited mentioned in the current studies.

## 1.2 Thesis objectives

The target of this research is to systematically study the controlling factors of shale electrical resistivity. The following steps are proposed:

- Use NMR, XRD, and Rock-Eval to characterise shale pore structure properties and composition;
- Design a referable experimental procedure to test shale resistivity;
- Quantitatively describe Archie's cementation exponent ( $m$ ) for shale with and without considering the effects of surface conductivity.
- Examine the effects of confining pressure and pore fluid salinities on  $m$ ;
- Examine the effects of rock composition and pore size distribution on shale electrical conductivity;
- Apply the derived  $m$  in different water saturation models.

## 1.3 Structure of the thesis

A total of eight chapters are included to address the objectives mentioned above:

**Chapter 1** introduces the topic and provides descriptions of the research background, gaps, objectives, and thesis structure.

**Chapter 2** describes sample characteristics, sample preparations, study methods, apparatus, experimental procedures and conditions for all the tests. The experimental procedures are designed differently based on research purpose. Additionally, the fundamental electrical model is introduced in this chapter.

---

**Chapter 3** discusses the experimental difference between conventional rocks and shale samples from the electrical measurement aspect and determines Archie's cementation exponent for shale reservoirs. A series of samples were cleaned during the sample preparation to remove the residual oil, while a few samples were not cleaned for comparison. A thorough cleaning is needed for shale samples due to the high resistivity of residual oil, which leads to the overestimation of Archie's parameters. To minimise the CEC effects, the high salinity of brine is used for saturation. The saturation time was tracked and verified as a solid reference for further tests on other samples. NMR was tested to indicate the total porosity, clay-bound water volume, pore size distribution, and the trace of residual oil. The resistivity of the shales was measured under atmospheric conditions (including 50 psi axial pressure for better sample-electrode surface contact) and reservoir conditions (2800 psi confining pressures) to minimise microfractures. The averaged computed Archie's  $m$  exponent was found to be 2.48 under ambient conditions and increased to 2.70 under reservoir conditions using formation factor  $F$  – porosity  $\Phi$  log-log method. Archie's  $m$  is a pressure-dependent parameter and increases with pressure (or depth) at 11% on both tested shales under the same reservoir conditions. It is believed to be related to stress-sensitive clay minerals compliance.

**Chapter 4** tests how and why pressure affects Archie's cementation exponent. The surface conductivity was excluded to simplify the study. Resistivity and porosity measurements were performed under a series of confining pressure (500–8500 psi). Nuclear magnetic resonance (NMR) was used to obtain porosity and pore size distribution and to detect the presence of residual oil. Both resistance and reactance of the complex impedance were recorded to determine the resistivity of samples at 1 kHz and to substantiate the pore size distribution changes based on the POLARIS model. The variation in shale resistivity and Archie's  $m$  under different pressure conditions is explained by the closure of microfractures at 500 psi; the narrowing of mesopores/macropores at 500–3500 psi; and limited changes beyond 3500 psi. This study indicates that, unlike typical reservoirs, Archie's  $m$  is sensitive to shale's depth of burial due to the soft nature of its pore system. An equation is developed to predict Archie's  $m$  under different pressures after the closure of microfractures.

**Chapter 5** discusses the extent to which CEC affects Archie's  $m$ . In this study, we controlled CEC effects by comparing Archie's  $m$  under different pore water salinities. Shale samples were dried and re-saturated at different pore water salinities, and the porosity and pore size distribution of the saturated samples were measured using NMR. The electrical conductivity was measured at 2800 psi confining pressure to simulate reservoir conditions. The effective porosity was determined by

---

comparing the sample weight at the dry and fully saturated states. We find limited changes in Archie's cementation exponent  $m$  at different salinities. We believe CEC only has limited effects on Archie's  $m$  in shale samples; the effects of changes in the pore electrical channel outweigh the CEC effects for shales, as explained by the volume averaging approach.

**Chapter 6** examines the effect of organic matter richness, clay content, pore size distribution on the electrical resistivity of shale samples. The relationship between Archie's cementation exponent and controlling factors is qualitatively characterised. The accuracy of water saturation calculations is compared by the Archie cementation exponents derived by total porosity and effective porosity. The Waxman & Smits equation overestimates the water saturation, while the Simandoux equation shows better water saturation prediction matching to the experimental results of the as-received samples by using the same inputs. Simandoux equation with Archie(mT),  $n=2$ , and total porosity is recommended in well-log interpretation.

**Chapter 7** provides the conclusion of the study.

---

## **Chapter 2**

# **Sample characteristics and methods**

---

---

This chapter reviews the current knowledge of electrical theories and testing methods and presents detailed descriptions of the sample preparation and the experimental methodology for shale samples.

## **2.2 Samples and sample preparations**

### **2.2.1 Sample characteristics**

A total of 18 shale samples were analysed in these experimental studies: (i) 13 samples from the Ordovician Goldwyer Formation of the Canning Basin, Australia; (ii) 4 samples from Permian Roseneath and Epsilon shales and Murteree shale of Encounter#1 (REM) from the Cooper Basin, Australia; and (iii) 1 sample from Eagle Ford shale (EF1) from the outcrop of Western Gulf Basin, America. Tables 2.1 and 2.2 show the characteristics and mineralogical composition for all tested samples. For the Goldwyer samples, plug samples and disc samples from the same depth were collected to meet different experimental needs. Goldwyer and REM samples are illite-rich and smectite-poor samples due whereas EF1 is a carbonate-rich shale.

### **2.2.2 Sample preparation**

All the samples were selected with no visible cracks. Goldwyer samples are oil shales from which six plug samples (Th24, Th25, Th28, Th37, Th39, Th45) were selected to be cleaned with toluene and methanol (ratio 3:1) under 70°C to remove any residual hydrocarbon and salt. The disc samples and three remaining Goldwyer plugs (Th17, Th23, Th40) were kept as-is for comparison purposes. As REM samples are gas shales with no oil, and EF1 is an outcrop sample, there was no requirement for sample cleaning. The Theia#1 samples were considered clean once the colour of the chemical mixture remained crystal clear (i.e. no more dissolved oil), which usually took around two months. Unfortunately, despite our effort to maintain the integrity of the samples, few horizontal fractures along the bedding planes developed during the cleaning process. All the samples were dried in an oven under 60°C over at least 48 hours to remove any residual chemicals and pore water before the saturation procedure. Note that at such a temperature, the clay-bound water (CBW) is retained while movable and weakly bound water is removed from the samples ([Testamanti and Rezaee, 2017](#); [Yuan et al., 2018](#)).

**Table 2.1** Studied shale sample characteristics

Shale formation	Sample ID	Depth (m)	Plug diameter (mm)	Plug length (mm)	Plug volume (cm <sup>3</sup> )	Dry Weight (g)	Brine saturated weight (g)
GOLDWYER	Th17	1472.13	38.38	28.51	32.98	80.74	83.88
	Th23	1508.89	38.3	26.08	30.05	73.3	75.55
	Th24	1510.54	38.41	51.26	59.4	144.02	148.82
	Th24D	1510.54	38.38	10.22	11.8	28.79	29.79
	Th25	1512.7	38.3	30.05	34.62	84.66	87.79
	Th25D	1512.7	38.38	10.39	12.08	29.36	30.31
	Th28	1520.42	38.38	28.03	32.43	82.41	85.31
	Th37	1554.73	38.35	50.08	57.85	140.3	145.37
	Th37D	1554.73	38.38	10.38	12.19	29.3	30.29
	Th39	1563.3	38.35	43.27	49.98	120.34	125.25
	Th39D	1563.3	38.38	10.25	12	29.1	30.08
	Th40	1570.83	38.4	31.2	36.13	89.53	92.17
Th45	1591.9	38.42	31.34	36.33	88.71	93.44	
REM	En4441	3279	38.34	8.58	9.91	26.2	26.4
	En4451	3390	38.42	8.78	10.18	27.32	27.45
	En4455	3494.19	38.1	8.8	10.03	26.12	26.25
	En4457	3499.9	38.07	8.85	10.07	26.11	26.22
Outcrop	EF1	N/A	37.8	11.1	12.46	31	31.25

**Table 2.2** XRD composition of the studied shale samples

Sample ID	Quartz (%)	Kaolinite (%)	Illite/Mica (%)	Smectite (%)	Chlorite (%)	Total Clay (%)	Carbonate (%)	Pyrite (%)	Other minerals (%)
Th17	17.42	3.43	55.8	N/A	10.99	70.2	N/A	N/A	12.37
Th23	14.94	0.14	35.5	0.69	N/A	36.3	32.02	2.28	14.46
Th24	18.34	0.3	24.3	0.98	5.64	31.3	35.57	2.32	12.51
Th25									
Th28	11.89	0.1	44.3	0.39	10.69	55.5	10.69	0.1	21.87
Th37	21.61	0.15	45.5	0.71	N/A	46.3	14.21	2.42	15.43
Th39	18	1	56	N/A	3	60	7	3	12
Th40	17.09	0.65	49.5	N/A	N/A	50.1	12.29	2.25	18.25
Th45	17.7	0.16	40.7	0.88	N/A	41.7	9.64	3.33	27.6
En4441	24	9	48.5	4.5	1	63	N/A	N/A	13
En4451	23	12	45	5	1	63	N/A	N/A	14
En4455	50	8	29	3	N/A	40	N/A	N/A	10
En4457	42	7	27	3	N/A	37	N/A	N/A	21
EF1	11	2	2	N/A	3	7	78	1	3

### 2.2.3 Pore water selections

NaCl was used to prepare the pore fluid as it is one of the most common types of salt in reservoirs, and the conductivity of almost all other anions and cations can be converted into equivalent conductivity of Na<sup>+</sup> and Cl<sup>-</sup>. As to the salinity, it varied across different experiments (i.e. 35g/l, 50g/l, 70g/l, 120g/l, and 250g/l). The lowest salinity was selected as seawater salinity (35g/l or 35,000 ppm), while the highest salinity (250g/l or 250,000 ppm) was chosen for two main reasons: (i) CEC effects; the effects of clay conductivity can be minimised when using a very high salinity brine, e.g., 200,000 ppm or greater salinity; and (ii) critical salt concentration (CSC) ([Keelan and McGinley, 1979](#)) which is described as a salinity threshold in water-sensitive sandstone. The clay particles are released from the pore walls when the salinity is below the CSC values ([Khilar and Fogler, 1984](#)). Although CSC only exists in the case of monovalent cations, this phenomenon can be effectively prevented by using high salinity brine. According to ([Khilar and Fogler, 1984](#)) the

---

threshold for NaCl is around 4g/l, which is lower than seawater salinity and, of course, much lower than the salinity required to minimise CEC effects.

## 2.3 Methods

### 2.3.1 Saturation procedure

All the plugs were air-vacuumed for 24 hours inside in-house saturation cells before injection and saturation at 2000 psi hydrostatic confining pressure using an ISCO syringe pump to maintain constant fluid pressure inside the saturation cells. Although many authors have used 2000 psi pressure to saturate shale samples ([Chakraborty et al., 2017](#); [Kuila et al., 2014](#)), there is limited information about the details of the saturation and, especially, about the time length for the saturation process. This study tracked the weight of the samples over time during the saturation process. In this study, five of the Theia#1 samples (Th23, Th24, Th25, Th37, Th45) were saturated and weighed every 7 days. The hydrostatic pressure was applied or removed from the saturation cells progressively with the pump at a rate of 100 psi/minute to avoid damaging the shale structures. The surfaces of samples were wiped out with damp paper to remove excess brine before taking the weight measurement. Figure 2.1 presents the weight change of a representative sample, Th24, which increased to its maximum saturated weight in the first week, with no further mass intake in the following weeks; the slight changes in the following weeks can be explained as measurement errors due to the rock surface water wiping, sample handling, and scale sensitivity. Based on the sample weight monitoring during saturation (Figure 2.1), it is believed that up to 2 weeks is sufficient to reach maximum saturation of the tested shales under 2000 psi hydrostatic pressure. Other samples were then saturated for up to 14 days based on the sample size.

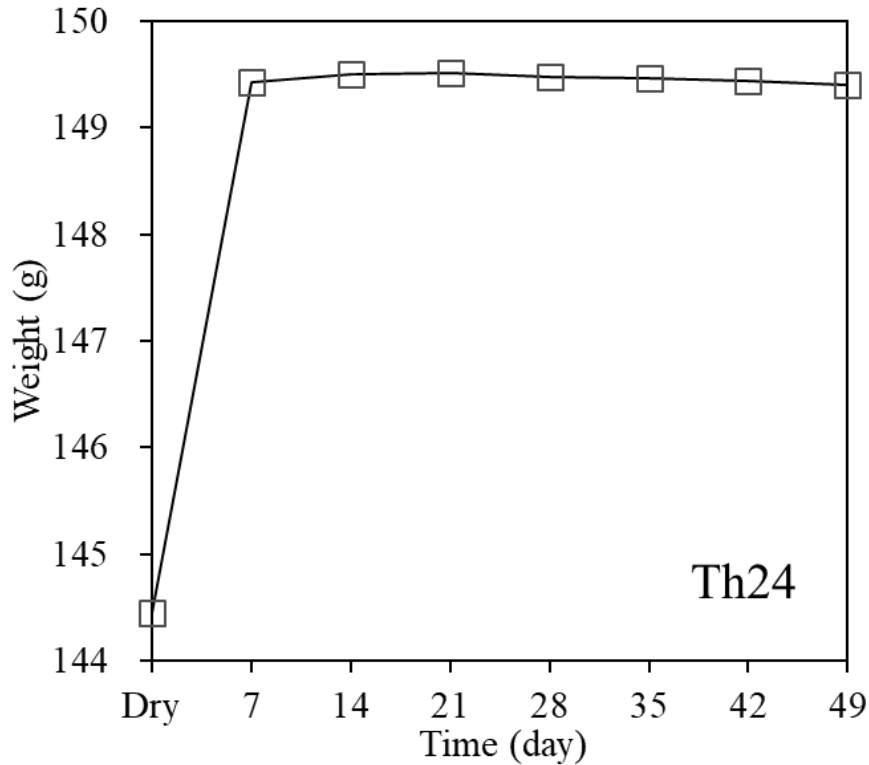


**Figure 2.1** Example of weight changes as a function of time from the sample Th24 during 49 days under 2000 psi brine exposure. All the tested samples reached their maximum saturation during the first week.

### 2.3.2 Nuclear magnetic resonance (NMR)

Nuclear magnetic resonance (NMR) was used for porosity measurement from  $T_2$  distribution, and  $T_1$ - $T_2$  mapping was recorded to detect potential residual hydrocarbons in the oil-shale samples (Theia#1). The three primary methods for testing porosity include NMR, mercury injection (MICP), and helium gas injection pycnometer. [Yuan and Rezaee \(2019\)](#) discuss the result of these three major porosity testing methods for different shale samples, and their results indicate that NMR porosity values are the most reliable of these three approaches due to the volume of CBW and wider detection of the pore size range. MICP and helium gas methods also have the disadvantage of running on dry samples, leading to potential cracks and damage to the samples. Since this study requires samples to be saturated and considers the CBW, NMR was chosen for investigating porosity.

The NMR  $T_2$  spectrum of shales can be divided into three pore sizes population corresponding to micropores ( $T_2 < 1$  ms), mesopores (1–20 ms), and macropores ( $T_2 > 20$  ms), among which  $T_2 > 100$ ms can be regarded as a fracture signal ([Song and Kausik, 2019](#); [Tang et al., 2016](#); [Zhang](#)

---

[et al., 2017](#)). Effective porosity (or movable water) can be derived from the saturated shales' NMR porosity by removing the CBW contribution (or irreducible water) assuming a shaly-sandstone concept. Although some publications ([Dunn et al., 2002](#); [Fleury et al., 2013](#); [Fleury and Romero-Sarmiento, 2016](#); [Tan et al., 2015](#)) state that it is hard to distinguish effective porosity from ineffective porosity using NMR on unconventional reservoir rocks, CBW as a marker to separate effective porosity from total porosity is easily identified due to its fast NMR  $T_2$  time ([Kausik et al., 2016](#); [Konoshonkin and Parnachev, 2015](#); [Ramirez et al., 2011](#)). [Testamanti and Rezaee \(2017\)](#) performed more specific NMR  $T_2$  measurements on dried samples under different temperatures and concluded that  $T_2$  cutoffs  $< 0.25$ ms can be regarded as CBW signals. In this study, we calculated the  $T_2$  signals below 0.25 ms and excluded these signals as the volume of CBW to compute the effective porosity. NMR porosity measurement from  $T_2$  distribution was performed on the saturated samples before and after resistivity measurement under room conditions, using a 2 MHz Magritek Rock Core Analyzer at Curtin University. Note that samples' post-resistivity measurement underwent 2800 psi confining pressure. The NMR  $T_2$  spectrum was measured using Carr, Purcell, Meilboom and Gill (CPMG) pulse sequence ([Carr and Purcell, 1954](#); [Kenyon et al., 1995](#); [Meiboom and Gill, 1958](#)), with 100  $\mu$ s inter-echo spacing (TE), 10,000 ms inter-experiment delay, 5000 number of echoes and a minimum of 200 signal-to-noise ratio (SNR). The NMR  $T_1$ - $T_2$  spectrum measurement, as an efficient method to distinguish residual oil and brine, was utilised using a 2 MHz GeoSpec2 from Oxford-GIT at CSIRO with 114  $\mu$ s inter-echo spacing (TE), 500 ms inter-experiment delay, and 4389 number of echoes, and a minimum 100 SNR.

Two different relaxation time phenomena were recorded,  $T_1$  (longitudinal relaxation time corresponding to the magnetisation recovery of  $H^1$  that is particularly sensitive to energy exchange between spins and surrounding lattice) and  $T_2$  (transverse relaxation time corresponding to the magnetisation decay and related to loss of spin phases of  $H^1$ ).  $T_1$  is, therefore, more sensitive to the big molecules bonded to  $H^1$  such as carbon-based materials (hydrocarbon, hydroxyls), while  $T_2$  is most sensitive to  $H^1$  content only, mostly disregarding any molecular binding effect. Using these  $T_1$  and  $T_2$  physical differences to our advantage, the  $T_1$ -to- $T_2$  ratio is equal to 1 with brine in rocks and increases  $> 1$  when organic components such as bitumen or oil occur ([Khatibi et al., 2019](#); [Mehana and El-monier, 2016](#)) making  $T_1$ - $T_2$  NMR mapping an ideal tool for fluid detection in shales, especially for oil ([Fleury and Romero-Sarmiento, 2016](#); [Washburn et al., 2015](#)).

---

### 2.3.3 Impedance measurement

The impedance of the samples was measured with an Autolab PGSTAT30 potentiostat/galvanostat (Metrohm) in the potentiostat mode using 1 V in the frequency range from 0.1 Hz to 1 kHz, to determine the complex impedance ( $Z$ ). When the impedance stabilised at the targeted pressure, the resistance ( $R$ ) was calculated using the equation  $R = |Z| \cos \theta$  at 1kHz frequency, where the phase ( $\theta$ ) meets its lowest value ( $\theta < 5^\circ$ ). The reactance ( $X$ ) was recorded over the whole frequency range (0.1–1000kHz) using equation  $X = |Z| \sin \theta$ . The resistivity was computed from the resistance measurement knowing the sample surface and sample length as:

$$\rho = (R.A)/L \quad (2.1)$$

where  $\rho$  is the resistivity (in ohm.m),  $A$  is the sample-electrode interface section area (in  $m^2$ ) and  $L$  is the distance between the two electrodes corresponding to the sample length (in m).

#### 2.3.3.1 Resistivity measurement at ambient conditions

Under ambient conditions, the sample was wrapped in cling film to prevent water evaporation during measurement. To improve the sample interface coupling with the electrode platen, a small constant axial pressure of 50 psi was applied using an oil-hydraulic pump before recording resistivity (Figure 2.2A). The cling film was also used as the insulator to prevent the current from leaking through the hydraulic metal piston body. (Figure 2.2A). Axial loading data was monitored every 5 seconds and the impedance data were measured by the spectrometer more than 7 times per second. The impedance values under room condition and 50 psi axial loading were validated when the spectrometer was reading stable impedance data over 5 minutes. The impedance data at 1 kHz were then used to calculate the sample resistivity.

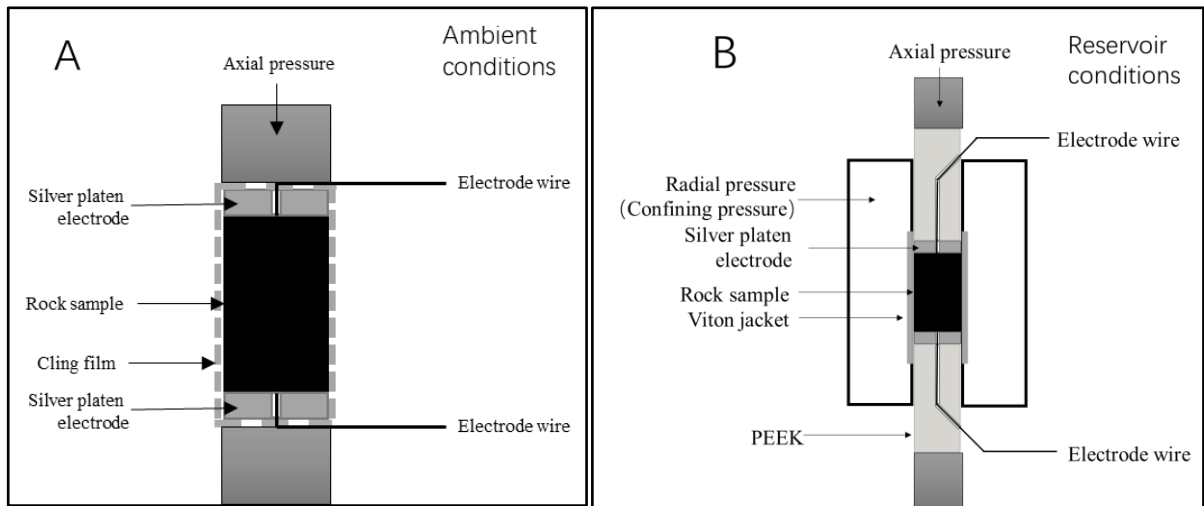


**Figure 2.2** A-Resistance measurement rig for the ambient condition; B-Resistance measurement rig for reservoir condition

### 2.3.3.2 Resistivity measurement at confining pressure conditions

For the electrical resistivity test under confining pressure conditions, the sample was placed between silver electrode platens in contact on the sample end surfaces and then inserted into a Viton jacket and placed in a pressure vessel between two axial hydraulic pistons separated by PEEK plugs for electrical insulation. A small axial load of 50 psi was applied to ensure sample–electrode coupling (Figure 2.2-B). The confining pressure was slowly increased to different conditions at 50 psi/min using an ISCO syringe pump while the impedance was recorded every 10 seconds until stabilisation using the same settings as for the electrical resistivity measurement at ambient conditions. Figure 2.3 presents an example of time-dependent resistivity measurement under reservoir conditions for oil-cleaned brine-saturated Th45. The data indicated a fast resistivity increase in the first 200 minutes from 19.5 to 24 ohm.m; before slowly stabilising after 900 minutes (or 14 hours) at 26 ohm-m. Therefore, 14 hours was further utilised as a standard time for the rest of the samples to measure resistivity under increasing confining pressures.

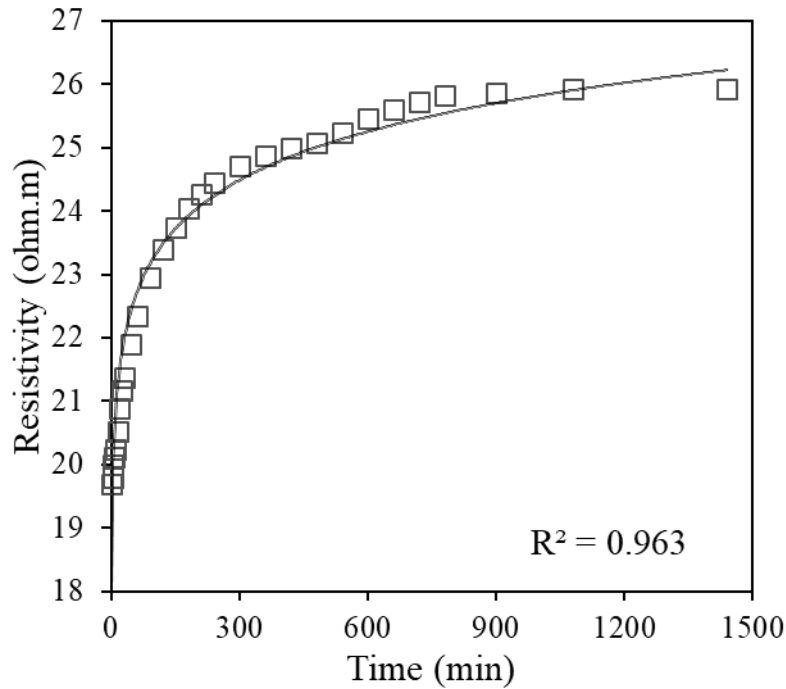


**Figure 2.3** The resistivity variation with time for the sample Th45 under 2800 psi confining pressure

### 2.3.4 Rock-eval pyrolysis

Rock-eval pyrolysis is a well-established method for the rock characterisation of organic matter and provides information about hydrocarbon content, hydrocarbon generation potential, kerogen type and maturity ([Espitalié et al., 1977](#); [Peters, 1986](#)). This method was initially used for the rapid test on the sediments to characterise the organic matter and to provide further information about the hydrocarbon generation potential, kerogen type and maturity. The method can also be used to identify heavy oils, estimate API gravity and characterise reservoir qualities ([Jones et al., 2004](#); [Jones and Tobey, 1999](#)). During the development of shale exploration, the method was programmed to characterise oil shale and investigate the immature soil organic matter or biomass ([Beti and Ring, 2019](#); [Carvajal-Ortiz and Gentzis, 2018](#); [Romero-Sarmiento et al., 2016](#); [Sebag et al., 2018](#); [Soucémariadin et al., 2018](#)).

Before measurements, the crushed shale samples with a weight of around 80 mg were settled in stainless steel crucibles with fritted top and bottom. Samples were then heated in a nitrogen atmosphere and the generation of hydrocarbon was continuously recorded by a flame ionisation detector (FID). Rock-eval pyrolysis was then carried out on Rock-Eval VI<sup>®</sup> analyser (manufactured by Vinci<sup>®</sup> Technologies).

The resulting programs exhibited two main peaks: an early S1 peak (mg HC/g) was detected during isothermal heating at 300°C, corresponding to free-hydrocarbons present in the rock, equivalent to extractable organic matters; and an S2 peak (mg HC/g) was detected at 650°C resulting from the thermal cracking of heavier and long-chain hydrocarbons for the remaining hydrocarbon potential (kerogen). The method was finalised by combustion (oxidation) of the residual fragments recovered after pyrolysis. The temperature corresponding to the peak of hydrocarbon generation during heating to 650°C is known as the Tmax, which strongly depends on the type and maturity of the kerogen (Jarvie and Tobey, 1999). Total organic carbon (TOC) content, which represents the richness of organic matter, is derived from two fractions: (1) the convertible fraction, which represents the hydrocarbons already generated (S1) and the hydrocarbons potential (S2); and (2) the residual fraction, which is oxidised dead carbon and does not contain potential to generate hydrocarbons. Kerogen can be classified into three types, using the van Krevelen diagram (Tissot and Welte, 1984). HI is the normalised hydrogen content remaining in source shales, while OI is the normalised oxygen content presenting in kerogen.

### 2.3.5 Electrical models

Archie's equation (Archie, 1942) is well-known and widely applied in the field of petrophysics. The general form is as follow:

$$F = \frac{R_0}{R_w} = \frac{a}{\phi^m} \quad (2.2)$$

where the formation factor ( $F$ ) is related to the resistivity of the rock fully saturated with brine ( $R_0$ ) normalised to the brine resistivity used to saturate the rock ( $R_w$ ). Formation factor ( $F$ ) is therefore a constant value for every sample, independent of brine salinity. Archie extended the formation factor formula as a function of porosity ( $\Phi$ ), cementation exponent ( $m$ ) and tortuosity factor ( $a$ ).

The general form of Archie's equation for the water saturation ( $S_w$ ) calculation can be expressed as equation (2.3) where  $n$  is the saturation exponent and  $R_t$  is the partially saturated rock resistivity such that  $R_t$  equals  $R_0$  when fully saturated.

$$S_w = \sqrt[n]{\frac{a}{\phi^m} \times \frac{R_w}{R_t}} \quad (2.3)$$

In this research, as all the samples are fully saturated with brine ( $S_w=1$ ), saturation exponent  $n$  is neglected and  $R_t$  equals  $R_0$ , which is defined as the resistivity of a 100% saturated sample. However,

this equation is only applicable to clay-free or clean formations. The second contribution, surface conductivity, was observed to play an important role (Figure 2.2), especially in shaly formations ([Patnode and Wyllie, 1950](#); [Wyllie and Southwick, 1954](#)). For the shaly formations, the quantities of apparent formation factor ( $F_a$ ) and intrinsic formation factor ( $F$ ) are related through Waxman and Smits's equation ([Waxman and Smits, 1968](#)) :

$$F_a = \frac{R_0}{R_w} = \frac{F}{1+BQ_vR_w} \quad (2.4)$$

where  $Q_v$  is the cation exchange capacity (CEC) per unit pore volume of the rock in units of equivalent litre<sup>-1</sup>,  $B$  is the equivalent conductant of CEC in units of mho m<sup>-1</sup> litre equiv<sup>-1</sup>, and  $F_a$  is the apparent formation factor.

The difference between  $F$  and  $F_a$  in this equation is indicated as parameter  $BQ_v$ , which represents the conductivity of the CBW on the mineral surface. It is recognised that CBW functions differently to free water in rock electrical conductivity ([McPhee et al., 2015](#)). For free water, electrical conductivity is controlled by its salinity, whereas CBW is believed to be anion-free water, which means this type of water has no salinity ([Hill et al., 1979](#)). The electrical conductivity of CBW is controlled by the cation exchange on clay mineral surfaces ([Clavier et al., 1984](#); [Waxman and Smits, 1968](#)) and named parameters  $BQ_v/F$  in equation 2.4. As shown in Figure 2.4 ([Worthington, 1993](#)),  $F$  approaches  $F_a$  when  $Q_v$  or  $R_w$  is low.  $Q_v$  is mainly decided by the volume and types of clay mineral and varies in different samples, while  $R_w$  is much easier to control. At low salinities, the dominant electrical current paths are pore spaces and mineral water interfaces ([Revil et al., 1998](#)), while the main path shifts to pore water only when the pore water salinity becomes high. Under high salinity conditions, since the CEC is becoming negligible, the apparent formation factor ( $F_a$ ) is closer to the intrinsic formation factor ( $F$ ). Therefore, intrinsic formation factors can be derived by the slope of the rock conductivity to pore water conductivity plot on the lineal trend part under the high salinity area ([Coperey et al., 2019](#); [André Revil et al., 2014](#); [Revil, Soueid Ahmed, et al., 2018](#)). ([Keelan and McGinley, 1979](#)) mention that intrinsic and apparent formation factors were considered equal at a pore water salinity of 200,000 ppm or greater. In this case, equation 2.2 and 2.4 can be written as:

$$F_a = F = \frac{a}{\phi^m} \quad (2.5)$$

Equation 2.6 is a modified version of Equation 2.5. Based on this equation, the tortuosity factor ( $a$ ) can be determined from the intercept of the negatively sloping best-fit line with the y-axis of  $F-\Phi$  log-log plot at  $\Phi=1$ , and the cementation factor  $m$  is its negative slope.

$$\log F = \log a - m \log \Phi \quad (2.6)$$

The value of  $a$  and  $m$  depends on several factors such as the cementation condition, pore geometry, pore tortuosity, clay type, and distribution, the content of conductive minerals and organic matter ([Archie, 1942](#); [Nabawy et al., 2010](#)).

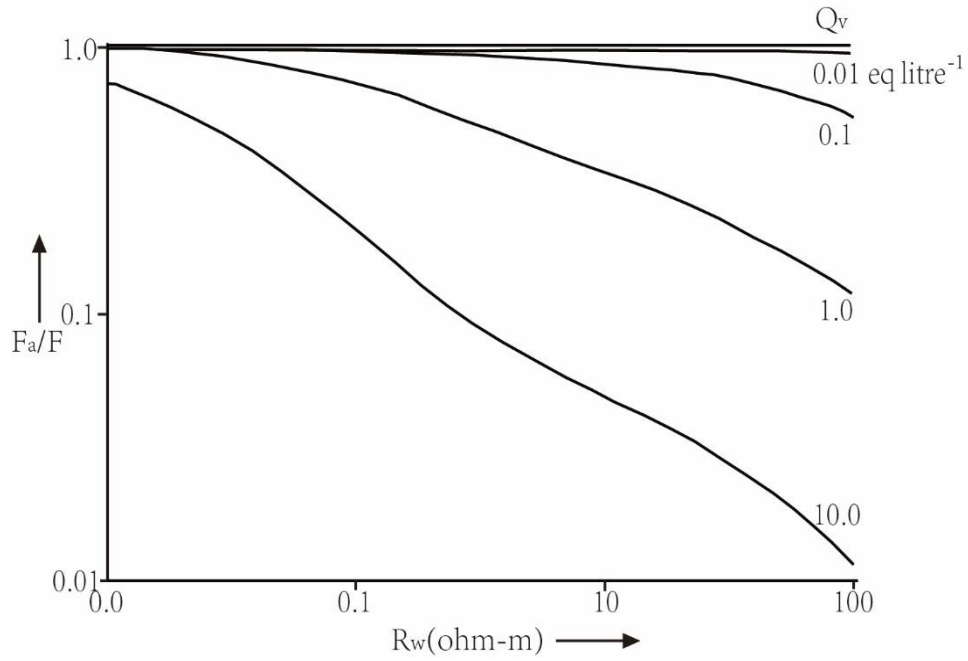


**Figure 2.4** Variation of  $F_a/F$  with  $R_w$  for four specified values of  $Q_v$  (in equiv litre<sup>-1</sup>), according to the hypothetical petrophysical model ([Worthington, 1993](#)).

---

## **Chapter 3**

# **Determination of Archie's cementation exponent for shale reservoirs**

---

---

## 3.1 Introduction

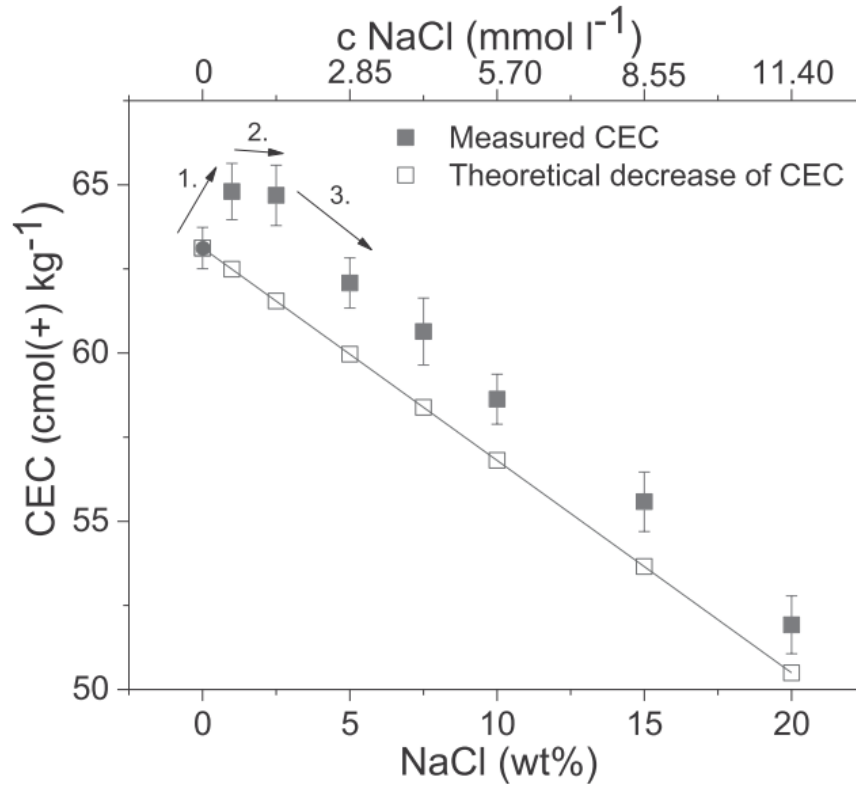
Archie's cementation exponent is a parameter that describes the number and size of the opening pores as well as their pore geometry ([Salem and Chilingarian, 1999](#)). This parameter exhibits wide variations between one to infinity from a mathematical sense, while refined between 1.3 to 3 in practical based on lithology, porosity, and compaction degree ([Keller and Carmichael, 1982](#); [Wyllie and Rose, 1950](#)). As to shale formations, Archie's cementation exponent is difficult to derive not only because of the complex nature of shale but also the existence of surface conductivity (CEC) disturbs the evaluation of the electrical contribution by the pore channels filled with water. Fortunately, the contribution of surface conductivity becomes negligible when pore water salinity goes high ([Revil et al., 1998](#)), showing an inverse correlation between CEC and salinity as indicated in Figure 3.1 ([Bohác et al., 2019](#)). Therefore, Archie's cementation exponent could be derived after isolating the electrical contribution of surface conductivity.

This study aims to present a standard experimental procedure to deal with shale formations and to document the general intrinsic Archie's parameter  $m$  considering the strong CEC effects on the apparent resistivity. The evaluation is based on the resistivity of samples saturated with a high salinity of NaCl brine solution under reservoir conditions to close potential induced microfractures from sample preparation. Transversal relaxation time  $T_2$  distribution from nuclear magnetic resonance (NMR) acquisition is combined with  $T_1$ - $T_2$  spectrum NMR measurement to address the porosity derivation for Archie's parameters computation.

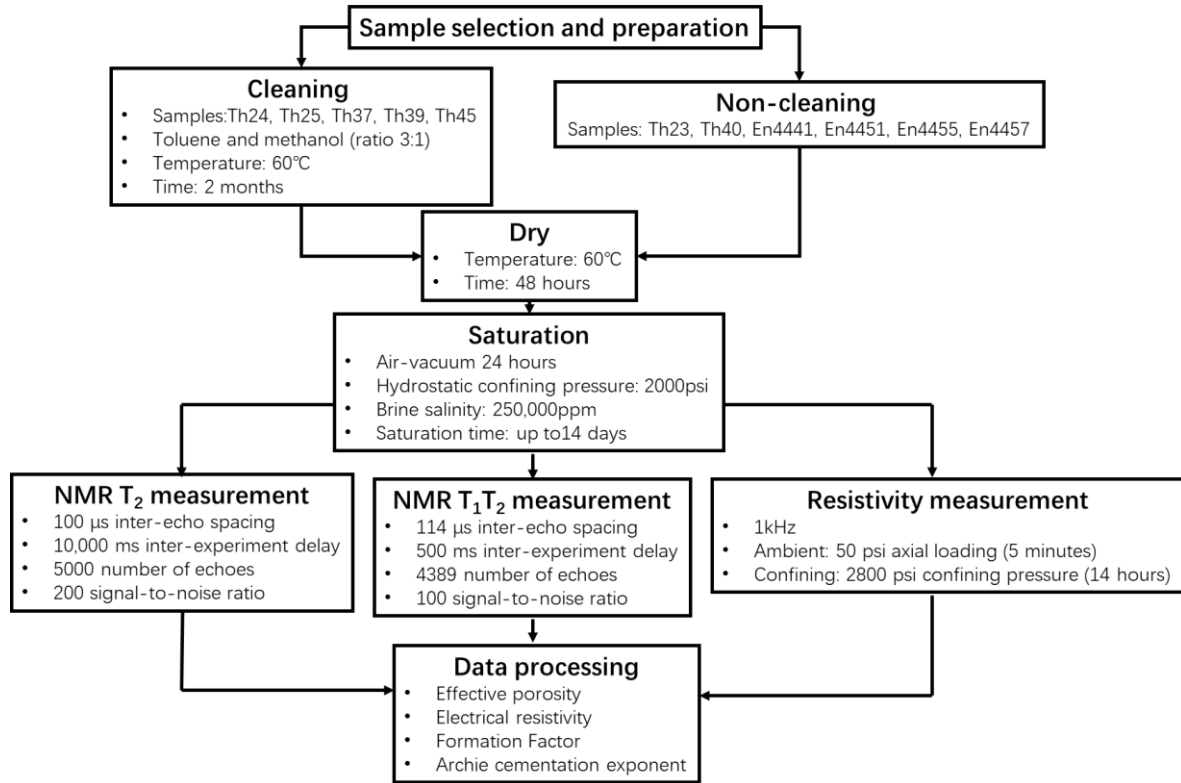
## 3.2 Methodology

Figure 3.2 shows the experimental flow chart for the porosity and electrical resistivity measurements. A total of 11 unpreserved shales were recovered normal to bedding: (i) 7 samples from Ordovician Goldwyer Formation of Theia#1 from the Canning Basin, Australia, from a depth of about 1500 m, and (ii) 4 samples from Permian Roseneath shale, Epsilon Formation and Murteree shale of Encounter#1 (REM) from the Cooper Basin, Australia, from a depth of around 3450 m (Table 2.1). Based on Theia#1 sample depth recovery and three measured principal stresses in the Canning Basin ([Bailey and Henson, 2019](#)), the reservoir pressure condition was computed at about 2800 psi. We chose to apply such reservoir conditions to both tested shale formations (Goldwyer and REM) in this study. Notably, NMR at 2800 psi was for samples after the confining

stress but measured at ambient conditions. X-ray diffraction shows all the samples are illite-rich shale (Table 2.2). Theia#1 samples contain 14.94–21.61 wt% quartz, 24.3–55.8 wt% mixed illite, a negligible amount of kaolinite and smectite (Database of Government of Western Australia Department of Mines, Industry Regulation and Safety). The Encounter#1 shales' average mineral composition is 25 wt% quartz, 10 wt% kaolinite, 35 wt% mixed-layer illite–mica, and 17 wt% mixed-layer illite–smectite ([Josh et al., 2016](#)).



**Figure 3.1** CEC of Calcigel® as measured by the Cu-trien method. NaCl (wt%) is the solid content of NaCl in the Calcigel®/NaCl mixture. The theoretical decrease in CEC represents a decrease in the CEC based on the diluted weight of bentonite ([Bohác et al., 2019](#)).



**Figure 3.2** Experimental flow chart for porosity and electrical resistivity measurement

## 3.3. Results

### 3.3.1 NMR porosity analysis

NMR  $T_2$  distribution was measured immediately after sample saturation. The NMR porosity of Theia#1 samples (post-oil treated, except Th23 and Th40) showed a higher porosity value, ranging from 11.67% to 16.58%. The Encounter#1 samples showed a much lower range, from 4.12% to 6.62%. Figure 3.3 illustrates the NMR pore size distribution curve for all the samples studied. As expected in shales, the CBW and microporosity from the  $T_2$  spectrum with  $T_2 < 3$  ms is the dominant population. Previous studies mentioned that the cracks and larger voids filled with fluid can be detected by  $T_2 > 100$  ms on tight sandstone (Li et al., 2016), and this finding is also applicable for shales (Song and Kausik, 2019). In our case, uncleaned samples (Th23 and Th40) show less signal beyond 100 ms, while signals in this area are much higher for oil-cleaned samples (Figure 3.3). Table 3.1 compares the cumulative porosity and matrix porosity (i.e. ignoring the signal from induced cracks at  $T_2 > 100$  ms) for all the samples. Induced fractures and other microfractures porosity determined using NMR for the uncleaned and cleaned samples in Theia#1 increase the original porosity to about 0.23% and 0.49% on average respectively.

Although the cumulative NMR  $T_2$  curve provides the porosity of fully saturated samples, only the effective porosity (i.e. movable water) is required for equation 2.2. Comparisons of NMR  $T_2$  distribution between ambient and 2800 psi confining pressure show a negligible porosity reduction ( $\ll 5\%$ ) for most of the samples studied (Table 3.1). Most of the porosity reduction is located on  $T_2 > 100$  ms where it quasi-disappeared (Figure 3.4). The CBW volume fraction ( $T_2 < 0.25$  ms) remains unchanged under reservoir pressure, indicating that CBW is not stress-sensitive, at least up to the reservoir stress condition of 2800 psi.

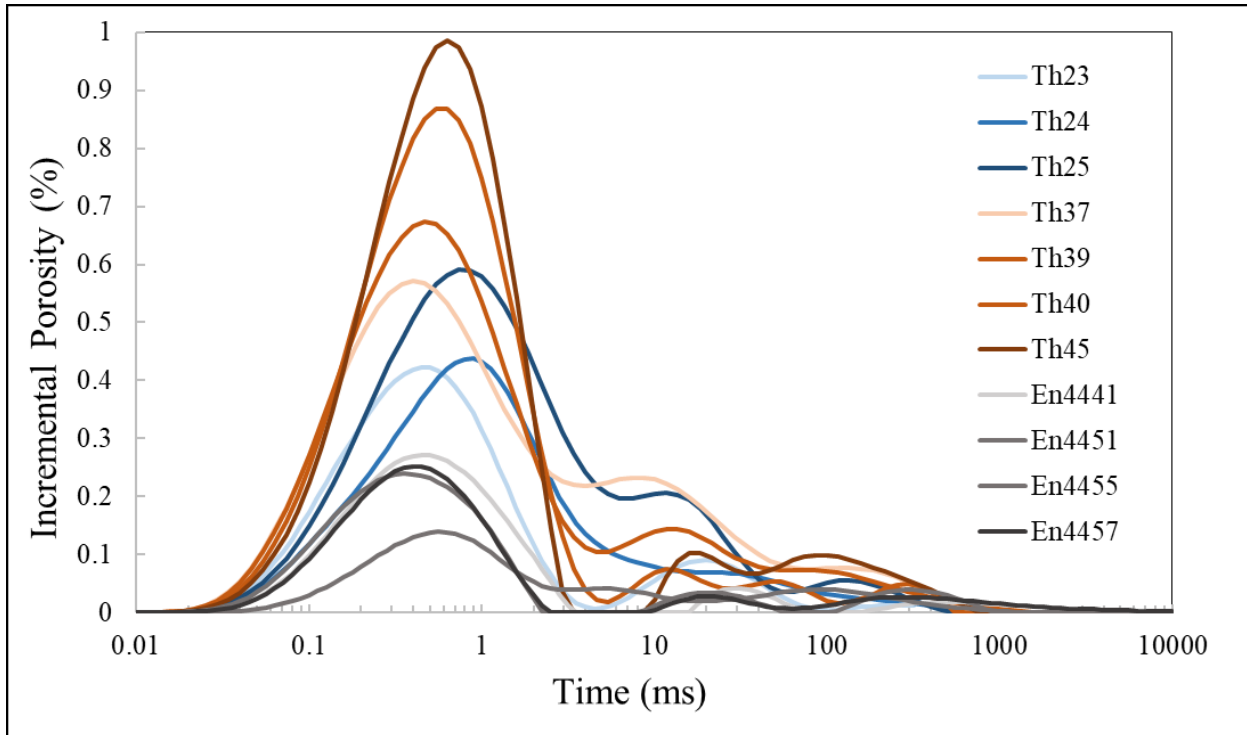


**Figure 3.3** NMR porosity and pore size distribution of the shales collection under ambient conditions after brine saturation. Th23 (light blue) and Th40 (dark orange) are uncleaned oil-shales while the other Theia#1 samples are oil-cleaned NMR data.

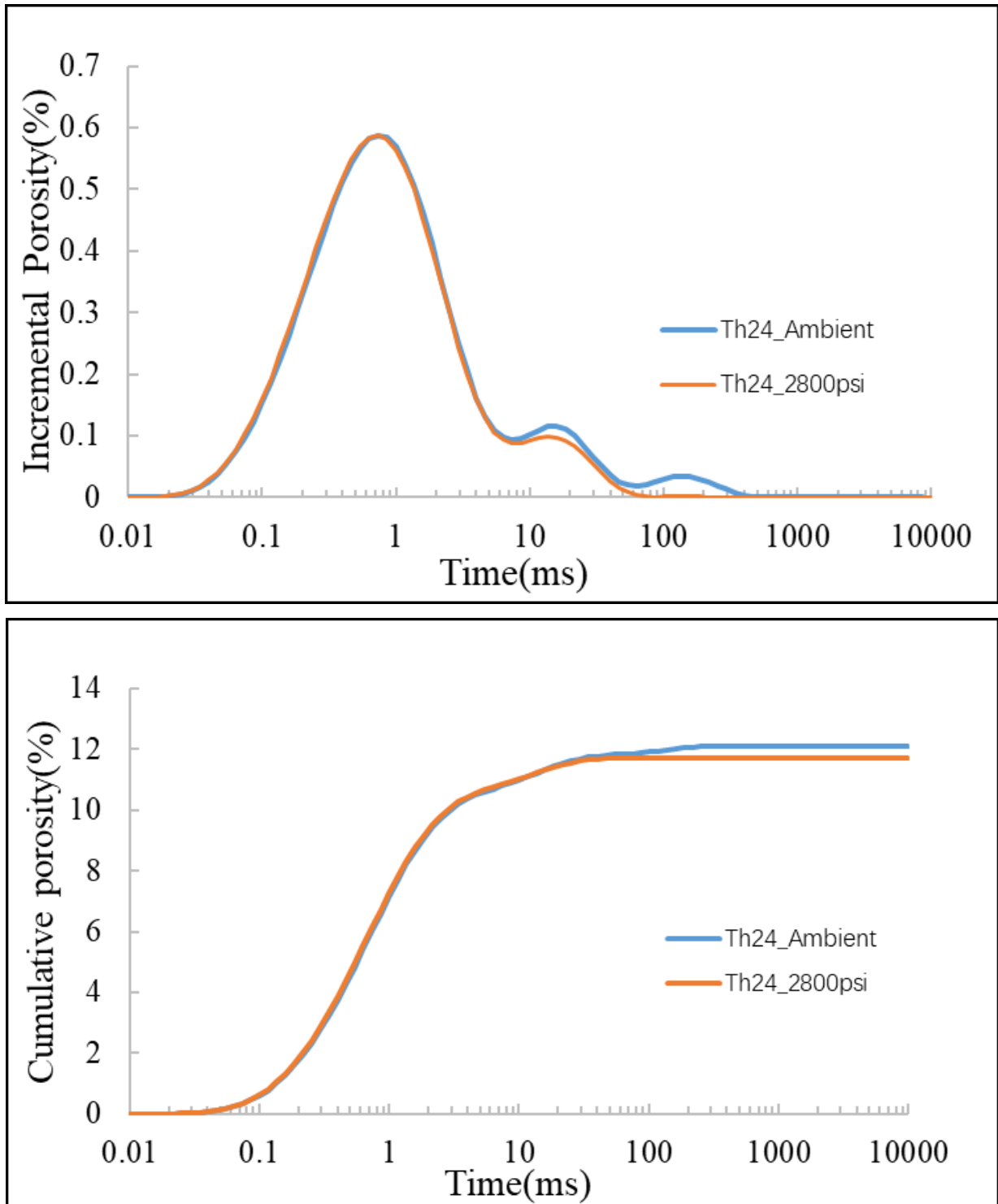


**Figure 3.4** Example of NMR porosity and pore size distribution under room conditions (blue curve) and 2800 psi confining pressure (orange curve) for the oil-cleaned shale Th24 brine saturated.

**Table 3.1** NMR porosity (in %) summary from the sample collection. Comparison between whole porosity at maximum saturation and matrix porosity (i.e. without microfracture signal at  $T_2 > 100\text{ms}$ )

Sample ID	NMR porosity @ambient condition	NMR matrix porosity @ambient condition	NMR porosity @ reservoir condition	Microfracture Porosity ( $T_2 > 100\text{ms}$ )	NMR CBW @ ambient and reservoir conditions ( $T_2 < 0.25\text{ms}$ )
Th23	11.67	11.49	11.33	0.18	3.8
Th24	12.3	12	11.8	0.3	2.31
Th25	13.84	13.5	13.03	0.34	2.21
Th37	14.85	14.25	14.26	0.6	3.71
Th39	14.62	14.11	(Sample broken)	0.51	3.84
Th40	15.28	14.95	14.81	0.33	3.82
Th45	16.58	15.89	15.04	0.69	3.62
En4441	6.62	6.3	6.2	0.32	1.87
En4451	4.12	3.74	3.8	0.38	0.65
En4455	6	5.54	5.49	0.46	2.08
En4457	5.87	5.32	5.28	0.55	1.78

### 3.3.2 NMR $T_1$ - $T_2$ Spectrum of oil signature

In the  $T_1$ - $T_2$  NMR spectrum map, the X- and Y-axis represent  $T_2$  and  $T_1$  relaxation times respectively, with  $T_1$ -to- $T_2$  ratio = 1 (diagonal line of the plot) when only liquid water occurs, and moving to higher ratio values when hydrocarbon signatures (oil/gas) are occurring. NMR  $T_1$ - $T_2$  mapping was conducted to check residual oil removal efficiency from the cleaning treatment. Figure 3.5-A shows the  $T_1$ - $T_2$  NMR spectrum for the uncleaned sample, Th23, and Figure 3.5-B for the cleaned sample, Th39, where the colour from blue to red represents the relative increasing incremental water volume intensity recorded in the shales. The circled light blue area in Figure 3.5-A indicates the presence of residual oil in either organic pores and/or inorganic pores in the sample with a  $T_1$ -to- $T_2$  ratio  $\gg 10$  (Kausik et al., 2016; Khatibi et al., 2019), while no such hydrocarbon signature is recorded in the cleaned sample (Figure 3.5-B). For the samples from Encounter#1, residual oil was not detected by NMR.

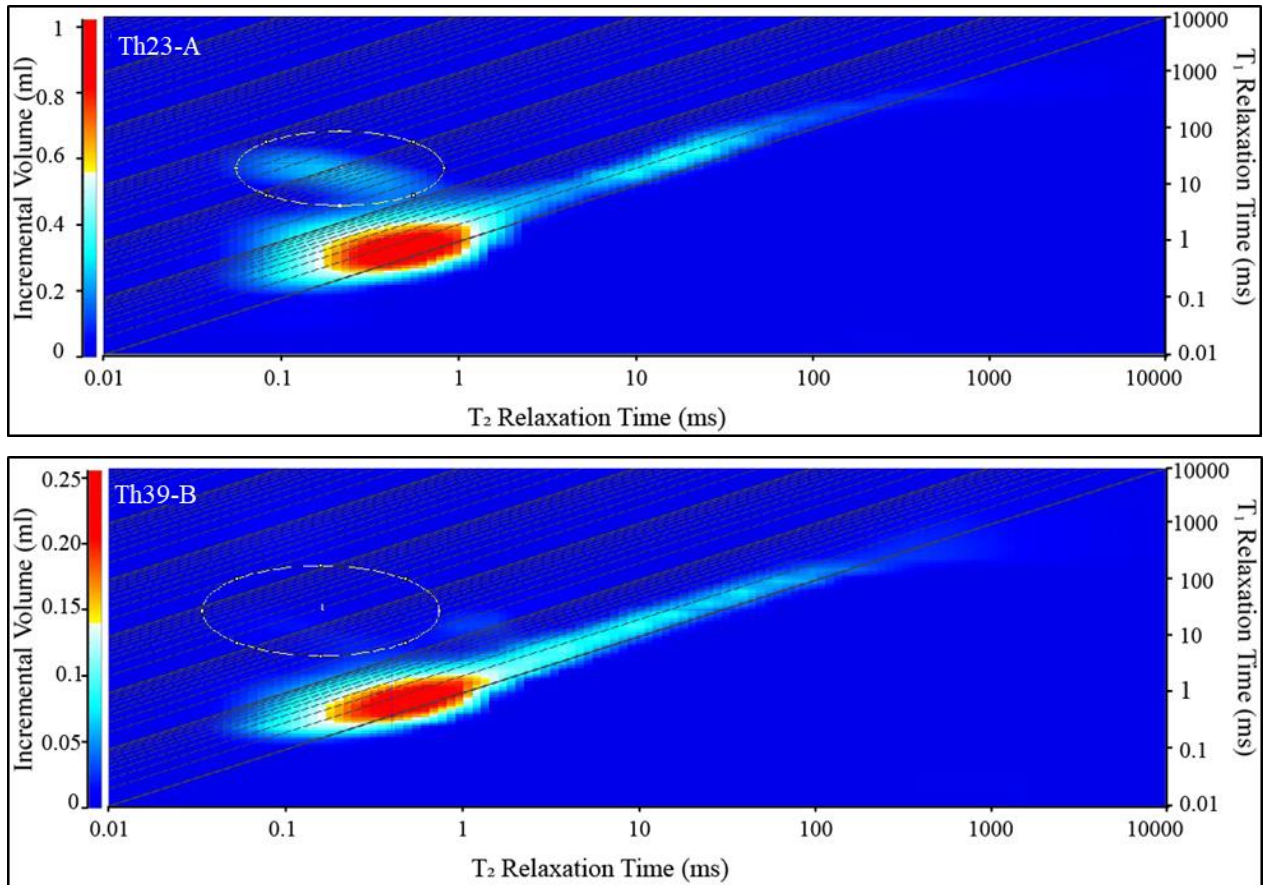


**Figure 3.5** NMR  $T_1$ - $T_2$  spectrum of the uncleaned sample, Th23, and cleaned sample, Th39.

### 3.3.3 Resistivity and Archie's parameter calculation in ambient and reservoir conditions

Table 3.2 presents both measured resistivity at ambient conditions (with a small 50 psi axial pressure for electrode-sample coupling) and 2800 psi confining pressure (reservoir condition). Under ambient conditions, the shales with higher porosities (i.e. Theia's samples) are associated with lower resistivities, and so a lower formation factor [ $F$  ranges from 325 to 634; with an exception at 2428], while shales with the lowest porosities (i.e. Encounter's samples) record higher resistivities and a higher formation factor [ $F$  ranges from 1300 to 2600].

Two approaches were used for the derivation of Archie's parameters. The first approach is to use tortuosity factor  $a = 1$  and derives the cementation exponent ( $m$ ) by applying Equation 2.2; the results are summarised in Table 3.2. Under ambient conditions, the lowest  $m$  is recorded in Encounter#1 at around  $m \sim 2.3 \pm 0.18$  on average and the highest values are calculated in Theia#1 at  $m \sim 2.79 \pm 0.16$ . Those values increase  $\sim 11\%$  under reservoir conditions on both tested shales.

The second approach plots the  $F-\Phi$  in the log-log scale to determine the negative slope ( $m$ ) of the best-fitted curve through the dataset. The intercept of this negative slope indicates the tortuosity factor ( $a$ ). To validate the conditions of equation 2.2, this curve must intercept  $F = \Phi = 1$  (Figure 3.). Encounter#1 samples (black dashed line) indicate  $m = 2.30$  at ambient conditions and increase to 2.55 at reservoir conditions, while Theia#1 samples (grey dashed line) show higher values than Encounter#1 shales at  $m = 2.76$  and 3.07 under ambient and reservoir conditions respectively.

A strong and rapid resistivity increase was observed for samples Th37 and Th39. This resulted from the poor connection between the electrode and the samples, which may have been caused by damage to the sample under confining pressure. This coupling issue is supported by the cracked sample, Th39 (which prohibited further NMR testing), and caused severe surface damage to sample Th37 post resistivity testing. Therefore, the resistivity of Th37 and Th39 was not included in the following analysis (labelled NA in Table 3.2).

**Table 3.2** Summary of formation factor, resistivity and Archie's cementation exponent  $m$  for the Theia#1 and Encounter#1 shales in ambient and reservoir conditions. Archie's  $m$  was computed from two methods: \* from  $a = 1$  in equation 2.2; and \*\* from  $F-\Phi$  log-log plot by refining the trendline by the point ( $\log F = \log \Phi = 1$ ). Formation water resistivity ( $R_w$ ) for all samples is 0.042 ohm-m. Data on samples Th37 & Th39 are not available (NA) due to damage.

Sample ID	AMBIENT CONDITIONS				RESERVOIR CONDITIONS			
	$R_o$ (ohm-m)	F	$m^*$	$m^{**}$	$R_o$ (ohm-m)	F	$m^*$	$m^{**}$
Th23	101.6	2428.38	3.04		269.03	6429.92	3.39	
Th24	26.52	633.73	2.76		57.64	1377.68	3.07	
Th25	24.15	577.29	2.91		42.4	1013.41	3.11	
Th37	17.07	407.94	2.67	2.55	NA	NA	NA	3.07
Th39	13.59	324.76	2.54		NA	NA	NA	
Th40	19.67	470.2	2.8		40.29	963.02	3.11	
Th45	17.2	411.12	2.87		25.93	619.68	2.96	
En4441	108.99	2604.95	2.52		217.58	5200.26	2.73	
En4451	54.4	1300.22	2.06	2.3	128.58	3073.18	2.32	2.76
En4455	105.85	2529.81	2.33		234.37	5601.5	2.55	
En4457	95.18	2274.85	2.31		266.5	6369.57	2.61	

---

## 3.4 Discussion

### 3.4.1 Influence of residual oil

The residual oil was detected in the uncleaned Theia sample Th23 using the  $T_1$ – $T_2$  spectrum map (Figure 3.5). Evidence presented in Table 3.2 indicates that the formation factor of Th23 is typically 4 to 8 times higher than that of the other samples from the same formation (i.e. Theia), representing a significant influence on rock resistivity despite a small residual oil content. Residual oil is a non-conductive material occupying the pore spaces and blocking the conductive channels, leading to an overestimation of the rock resistivity, formation factor and thus Archie's parameter  $m$ . Therefore, for greater accuracy, a thorough cleaning procedure is recommended for samples collected from reservoir formations albeit at the risk of further damaging samples on already damaged samples from improper hydration preservation after their recovery.

### 3.4.2 Influence of induced fractures

Induced fractures in unpreserved shales are inevitably intensified during cleaning and re-saturation procedures. These fractures increase the inaccuracy of test results in both resistivity and porosity measurements. The NMR porosity investigated by the NMR  $T_2$  spectrum found that uncleaned samples did not record an NMR signal at  $T_2 > 100$ ms, while cleaned samples did record NMR signals. Such NMR signals at  $T_2 > 100$  ms can be confidently ascribed to microfractures or macropores based on previous works ([Li et al., 2016](#); [Song and Kausik, 2019](#)). All the fractures caused by cleaning procedures and saturation procedures are found along the bedding plane. As shown in Table 3.1, NMR revealed that the contribution of those microfractures at  $T_2 > 100$  ms after saturation represents around 1.8% and 3.3% of the maximum saturated porosity on uncleaned and cleaned Theia#1 samples respectively. The cleaning treatment enhances microfracture development in oil-shales but the overall impact remains negligible with respect to uncleaned shales.

Under reservoir conditions, the induced microfractures are highly sensitive to confining pressure. During resistivity measurement under reservoir conditions, the closing fractures expel water from the shales but re-open when the pressure is released. Because the shales have low permeability, the re-opening fractures did not have time to refill with water before running NMR under ambient conditions. This is supported by the disappearance of the long  $T_2 > 100$  ms post resistivity under reservoir conditions (Figure 3.3). The change in NMR porosity from closing microfractures is, therefore, more intense on cleaned shales, which developed more microfractures from the

---

toluene/methanol treatment (up to 5% variation from the original porosity). It is therefore recommended that shale porosity under reservoir conditions be used in Archie's  $m$  calculation to avoid the influence of induced microfractures from cleaning and saturation processes.

Although 50 psi axial pressure was applied for better electrode–sample coupling during electrical conductivity measurement at so-called ambient conditions (i.e. 14.7 psi confining pressure), there was no evidence indicating that all the horizontal fractures were fully closed. This means that in ambient conditions conductivity of the samples might be overestimated since excess water is still filling in the incompletely closed fractures.

### 3.4.3 Influence of clay-bound water

Clay-bound water has a significant influence on both electrical conductivity and porosity calculation in this study. Figure 3.6 illustrates the CBW layer and its contribution to the electrical conductivity in the shale channel model. In this study, we injected high-salinity brine into the shales to limit the CEC, and thereby the additional conductance channel created by the cation exchange at the clay mineral surface. Exclusion of CBW volume fraction from the porosity is recommended for more accurate effective porosity calculation in Archie's equation ([Hill et al., 1979](#)). As shown in Table 3.1, the CBW volume ranges from 1.8% to 3.8% absolute value (or 16–33% contribution to total NMR porosity), except for sample En4451 which shows a low CBW volume compared with other samples, possibly due to lower clay content. This range is similar to the CBW tested on dried samples where published results range from 2% to 3.86% ([Testamanti and Rezaee, 2017](#)) and 1.64% to 3.02% ([Yuan et al., 2018](#)). By neglecting the CBW and using total NMR cumulative porosity for the calculation of Archie's  $m$ , the results would incorrectly increase by up to 4 and lead to average 15% variations for the  $m$  calculation. Therefore, not only the surface conductivity of CBW but also the volume of CBW should be considered in the calculation.

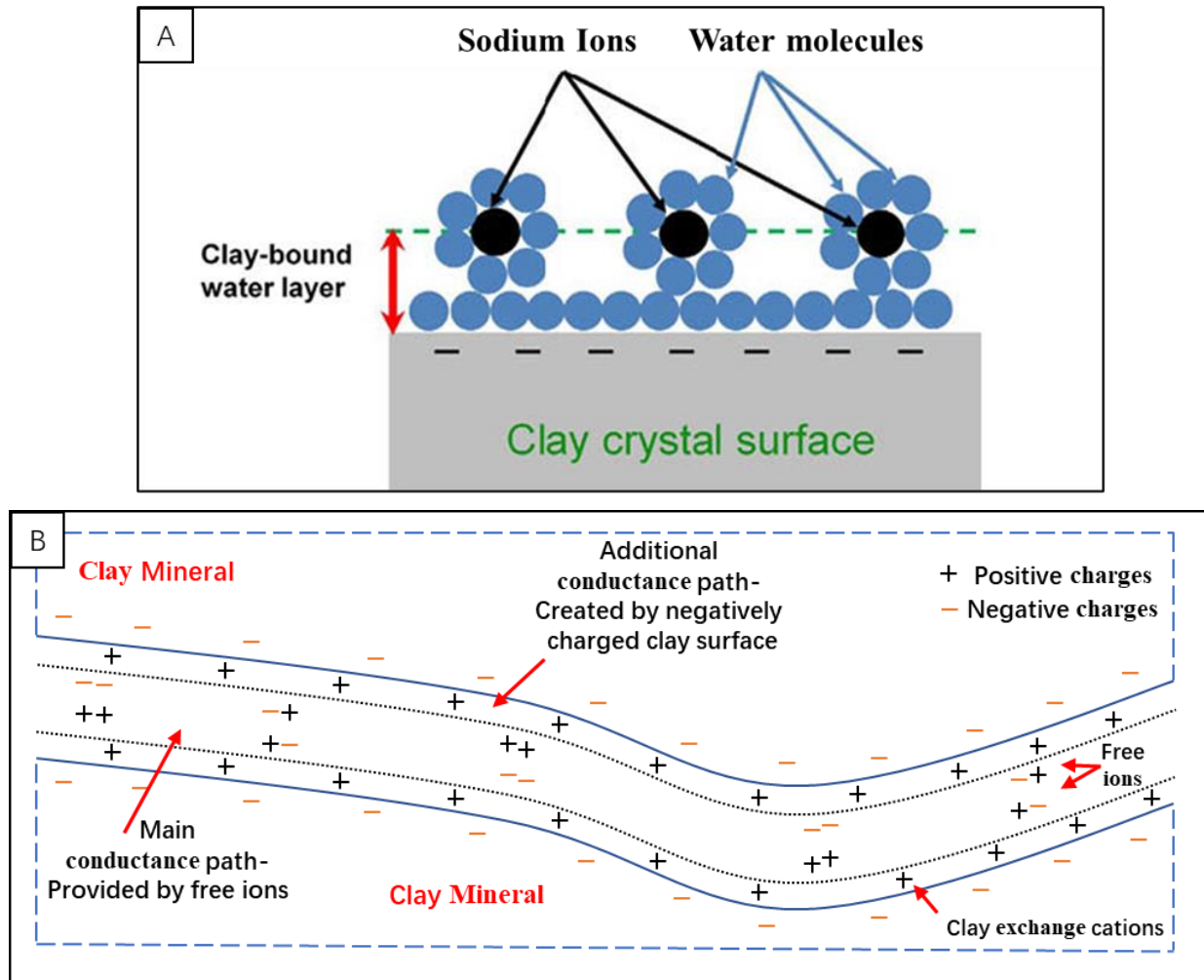


**Figure 3.6** Simplified schematic of electrical charges distribution on the clay mineral surface and pore channel: A-Diffuse double layer of water molecules at the smectite surface (McPhee et al., 2015); B-Conductance path and clay ion mobility in shale pore channel.

### 3.4.4 Variation of Archie's parameter $m$

As expected, the effective porosity evolves is inversely proportional to the formation factor; the highly effective porosity in Theia#1 samples shows low formation factors; in Encounter#1 samples with low effective porosity records a higher formation factor (Table 3.2). Higher porosity statistically increases the chances of more connected spaces and/or channels to increase the electrical conductivity of shale samples when filled with brine.

The averaged Archie's  $m$  shows similar values between both methods (i.e. Archie's equation 2.2 or  $F$ - $\Phi$  log-log plot; Table 3.2). Theia#1 records higher  $m$  than Encounter#1 due to the occurrence of oil traces despite thorough cleaning and being below NMR detectability (Figure 3.5). Sample Theia Th23 (the grey point on Figure 3.7) has a higher residual oil content, as recorded from NMR

---

$T_1$ – $T_2$  (Figure 3.5), leading to a much higher formation factor and so a higher apparent  $m$  value out of the trend. This outlier sample was excluded for the  $m$  calculation in Theia#1 shales. Additionally, the existence of residual oil in Theia#1 shales supports the hypothesis of irreversible change of the clay surface wettability, which becomes hydrophobic, limiting surface conductivity from brine and leading to higher  $m$ .

The averaged  $F$ - $\Phi$  log-log Archie's  $m$  from the complete shales collection (Theia#1 and Encounter#1) is around 2.48 under ambient conditions and increases to 2.70 under reservoir conditions (Figure 3.7). It is apparent that Archie's  $m$  is very stress-sensitive in shales; it increased to about 11% (using both Archie's  $m$  methods of calculation) from ambient to reservoir conditions in both tested formations despite having different porosity and/or effective porosity. As shown in Figure 3.4, the  $T_2$  signals representing microfractures were eliminated after the electrical resistivity test at 2800 psi. Signals decreased from 1–100ms, representing mesopores and macropores, while the signals below 1 < ms for micropores overlapped ([Song and Kausik, 2019](#); [Zhang et al., 2017](#)). This means that all the microfractures and some of the mesopores and macropores were closed under the pressure, leading to an increase in electrical resistivity, while the effects of micropores on rock resistivity under pressure are not obvious, as shown by the almost identical  $T_2$  signals under ambient and reservoir conditions. Since both gas- and oil-tested shales have similar clay content (50–60%), we believe that Archie's  $m$  stress dependency is directly controlled by pore structure changes related to the clay content no matter the porosity. Further experiments are still required to test how the stress sensitivity of Archie's  $m$  evolves with different reservoir pressure conditions. The variations of  $m$  within each shale formation are < 10% and might reflect the complexity of the pore topology from varying clay and organic matter contents ([Delle Piane et al., 2018](#); [Josh et al., 2016](#); [Josh et al., 2019](#)). Organic matter is especially complex in hydrocarbon-rich shales, with resistivity changing with the organic matter maturity. However, the quantitative relationship between the mineralogy and resistivity, as well as the relationship with petrophysical and mechanical properties (pore size distribution, SSA, CEC, etc.), remains poorly understood due to a lack of experimental data.

Compared with the values for Archie's  $m$  reported by other authors, Archie's  $m$  of this study is relatively higher. The  $m$  values of gas shale reservoirs derived from well-log interpretation were around 1.6 to 1.7 ([Quirein et al., 2010](#)), while in oil shale reservoirs  $m$  was measured at below 2 ([Dashtian et al., 2015](#); [Luffel and Guidry, 1992](#)), and was found to be around 1.6 in a laboratory experiment ([Malekimostaghim et al., 2019](#)). Those lower  $m$  values could be explained by the pore water salinity used being too low to limit the CEC effect, which leads to a lower formation factor

( $F$ ) and consequently a lower Archie's  $m$  from their log interpretations. This is supported by the  $m$  derivation experiment on shaly-sandstone with different salinity of brine (Kurniawan, 2005), which indicated an increasing  $m$  value with the increase of brine salinity.

Alreshedan and Kantzas (2016) published a study of the modelling of petrophysical and electrical properties of sandstone based on an experiment that explained why Archie's  $m$  varies under different pore topologies. When reducing pore throat radius and pore coordination number (the number of pore throats per pore body), Archie's  $m$  will increase from 1.99 to 2.81 with little change in the porosity. The same behaviour was observed in our data, where  $m$  increased from 2.48 to 2.70 under reservoir conditions with limited change in porosity. In our case, the reservoir stress conditions applied to shales reduced the pore throat size, which is mostly related to the compliance of clay minerals, and led to an increase in  $m$ . It is therefore recommended to take into account the expected increase of  $m$  with depth (i.e. the increase of pressure) in any shale formation.

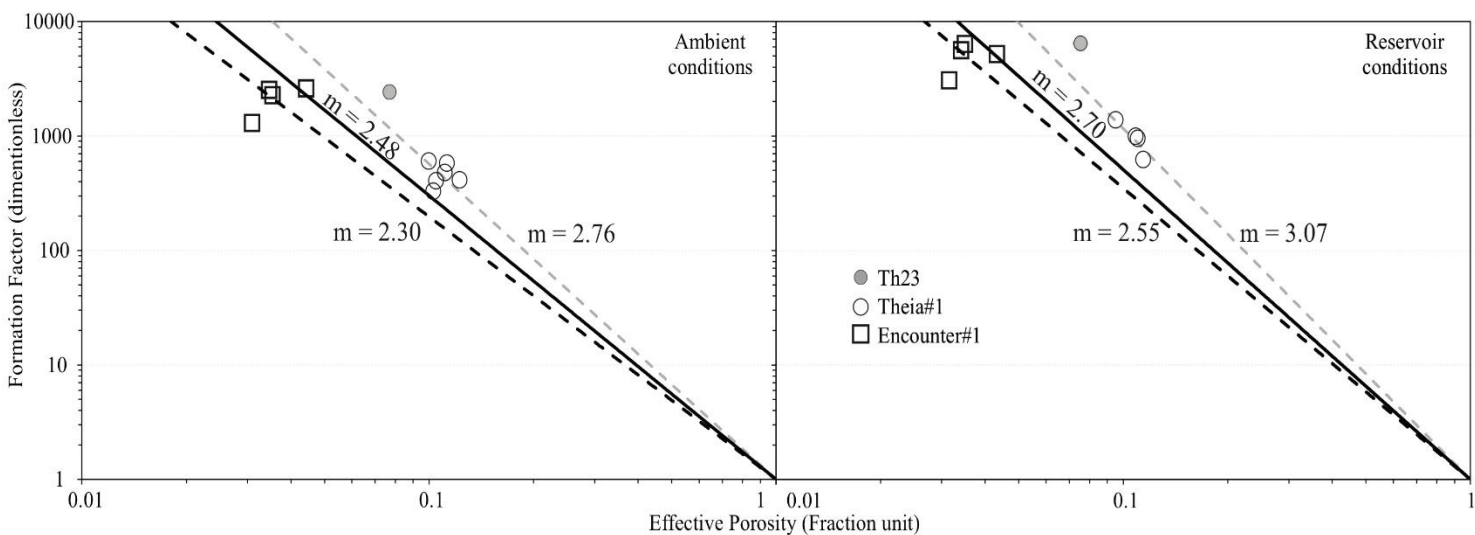


**Figure 3.7** Formation factor relationship with effective porosity on Theia#1 (circle symbols) and Encounter#1 (square symbols) saturated shales collection under ambient and reservoir conditions.

Forcing log-log fit line intercepts y-axis at effective porosity =1 and  $F=1$  for both ambient and reservoir conditions. Due to the existence of residual oil in Th23 detected from NMR  $T_1T_2$  mapping, this sample (grey circle) is excluded from the fitting curve. The Grey dashed line represents the average  $m$  from Theia#1 oil shales and the black dashed line presents the average  $m$  from Encounter#1 gas shales. The apparent averaged Archie's  $m$  from the whole shales collection (black line) is calculated at 2.48 and 2.70 under ambient and reservoir conditions respectively.

---

## 3.5 Conclusion

Determination of Archie's exponent  $m$  in shales is challenging due to clay surface conductivity, which dominates the resistivity response and prohibits proper measurement of the true resistivity. A new method to determine Archie's  $m$  for oil shales and a gas shale from Australia was tested. After a thorough cleaning of the shales using toluene and methanol solvents to remove residual oil and salts, a high-saline brine (250,000 ppm NaCl) was injected for two weeks under 2000 psi hydrostatic pressure to saturate the shales. The purpose of high salinity is to cancel, or at least reduce, strong cationic exchange capacity from clays and so remove the surface conductivity from clays. Nuclear magnetic resonance (NMR) was used to check the development of microfractures – which were found to be negligible (< 5%) – and to record the effective porosity used to compute Archie's  $m$ .

While saturated, the resistivity of the shales was measured under atmospheric conditions (including 50 psi axial pressure for better sample–electrode surface contact) and under reservoir conditions (2800 psi confining and axial pressures) to minimise microfractures. The averaged computed Archie's  $m$  exponent was found at 2.48 under ambient conditions increasing to 2.70 under reservoir conditions using formation factor  $F$  – porosity  $\Phi$  *log-log* method. Archie's  $m$  is a pressure-dependent parameter and increases with pressure (or depth) at 11% on both tested shales (despite being different shales) under the same reservoir conditions. It is believed to be related to stress-sensitive clay minerals compliance.

---

## **Chapter 4**

# **The pressure dependence of Archie's cementation exponent for shale reservoirs**

---

## 4.1 Introduction

Electrical resistivity is also stress-sensitive, with most resistivity changes occurring at the initial low pressure applied on the rock before slowly becoming less sensitive at higher pressures. This resistivity stress sensitivity follows an empirical expression ([Han, 2018](#); [Han et al., 2011](#); [Jing et al., 1989](#); [Jing et al., 1992](#); [Mahmood et al., 1991](#)):

$$\frac{1}{\sigma(P)} = \rho(P) = A + KP - B \exp(-DP) \quad (4.1)$$

where  $\sigma$  is the conductivity of the sample,  $\rho$  is the resistivity of samples,  $P$  is the effective pressure between the confining pressure and the pore pressure, and coefficients  $A$ ,  $K$ ,  $B$  and  $D$  are fitting parameters for rock conductivity measurement.

The exponential term of this equation was explained as the presence of the pores and cracks with different aspect ratios resulting from the variation in pore stiffnesses ([David and Zimmerman, 2012](#); [Tod, 2002](#); [Zimmerman, 1990](#)). Stiff and compliant pores have been recognised as the binary distribution of the pore structure of porous rocks ([Bernabe, 1991](#); [Kaselow and Shapiro, 2004](#); [Shapiro, 2003](#); [Shapiro and Kaselow, 2005](#)). Stiff pores in elasticity theory are spherical pores within a solid matrix that are believed to be less compressible. The volume of these pores decreases linearly with the increasing pressure. Compliant pores are more flattened and elongated in shape, showing an exponential decrease in volume under incremental pressure increase. In most cases, the pore space was believed to comprise stiff pores, and compliant pores were the main reason for the pressure sensitivity of electrical properties ([Dvorkin et al., 1995](#)).

In clay-rich shale formations, the pressure sensitivity of electrical properties may be expressed differently to homogeneous sandstone. The pores formed by clays are recognised as compliant pores due to the soft nature of clay particles. This type of pore occupies a larger proportion of the total pores in shales than in clay-poor samples, which may lead to different pressure sensitivity of electrical properties. The second reason is the excessive surface conductivity of clay minerals, the result of the cation exchange capacity (CEC). Currently, CEC is always regarded as a specific surface area (SSA)-related parameter controlled by the clay mineralogy of the sample ([Josh, 2014](#)) and treated within a constant value range in well-log interpretation by applying CEC-related equations, including Waxman & Smits and dual-water equations ([Clavier et al., 1984](#); [Waxman and Smits, 1968](#)). Limited experimental measurements exist in the literature on the relationship between confining pressure and electrical resistivity in shales.

---

The main purpose of this part of the study is to experimentally evaluate how the resistivity – and, correspondingly, Archie’s  $m$  – of shale samples varies with different pore geometry under different confining pressure conditions. To simplify this complex procedure, excessive mineral surface conductivity is limited by applying high-salinity brine ([Revil et al., 1998](#)). Therefore, the pore water within the connected pores is regarded as the only conductive channel in this study, and pore geometry variation under pressure sensitivity is indicated by the changes in rock resistivity.

## 4.2 Methodology

### 4.2.1 Samples preparation and experimental procedure

A total of 5 unpreserved oil/gas shale samples were collected from the Ordovician Goldwyer Formation in the Canning Basin, Australia. The X-ray diffraction tests indicate that all studied samples are illite-rich shale containing 11.89-18.34 wt% quartz, 24.3-55.8 wt% mixed illite and a negligible amount of kaolinite and smectite (Database of Government of Western Australia Department of Mines, Industry Regulation and Safety). Three of the samples (Th28, Th24, Th25) were cleaned with toluene and methanol (ratio 3:1) under 70°C in a soxhlet extractor to remove any residual hydrocarbon and salt. The toluene-methanol cleaning solution was regularly changed until it remained clear and transparent, corresponding to clean shales (i.e. no more oil dissolving in the cleaning solution). All the tested samples were then dried under 60°C for at least 48 hours before to saturate them with NaCl solution (250,000 ppm) for at least 7 days under 2000 psi hydrostatic pressure to achieve maximum saturation. The high salinity of the NaCl solution was selected to suppress the surface conductivity of clay minerals ([Keelan and McGinley, 1979](#)).

All of the samples were then separated into two groups with different NMR tests and impedance measurements for comparison. The experimental procedure for the Group 1 (Th24 and Th25) was as follows: (1) the impedance was first measured at ambient conditions (14.7 psi confining pressure) using a constant 1 V excitation voltage at 1 kHz using an LCR-819 spectrometer (Gw Instek Ltd.) in potentiostatic mode; (2) the sample was placed between silver electrode platens then inserted into a Viton jacket within a pressure vessel between two axial hydraulic pistons separated by PEEK plugs for electrical insulation. A small axial load of 50 psi was applied to ensure sample–electrode coupling (Figure. 2.2-B); (3) the confining pressure was slowly increased to 500 psi at 50 psi/min using an ISCO syringe pump, while the impedance was recorded every 10 seconds until stabilisation. Based on our previous study, 14 hours was proved to be sufficient to meet the impedance and stress stabilisation criteria; (4) the pressure was then reduced back to ambient

---

condition at 50 psi/min and the sample was removed from the pressure vessel, weighed and immediately tested for NMR  $T_2$ ; (5) the sample was put back into the pressure vessel as for step (2) to record its impedance under higher pressure. Procedures (3) to (5) were repeated under the following increasing pressure stages: 500 psi, 1000 psi, 1500 psi, 2500 psi, 3500 psi, 4500 psi, 6500 psi and 8500 psi.

To minimise manual errors in transferring samples during the experiment, samples Th17, Th23 and Th28 were used as Group 2 for more continuous impedance tests without taking samples out for the NMR tests. The first two procedures for Group 2 are the same as those mentioned for Group 1 before undergoing a more continuous impedance recording under the same confining pressure steps (i.e. 500 psi, 1000 psi, 1500 psi, 2500 psi, 3500 psi, 4500 psi, 6500 psi and 8500 psi), and the same stabilised time ( $\geq 14$  hours), without taking the sample out of the pressure vessel. By doing this, we sacrificed the sample weight variation measurements and NMR changes under different pressure stages. After the last impedance test under 8500 psi, the weight recording and NMR test were performed under room conditions. The impedance of the Group 2 samples (Th17, Th23, Th28) was analysed with an Autolab PGSTAT30 potentiostat/galvanostat (Metrohm) in the potentiostat mode using 1 V in the frequency range from 0.1 Hz to 1 kHz, to determine the complex impedance ( $Z$ ). Then the impedance was separated as the resistance and reactance for further calculation (equation 2.1).

#### 4.2.2 Effective porosity calculation

The effective porosity in shales is defined as the total porosity without clay-bound water (CBW) ([Bouton et al., 1996](#)). For the calculation of Archie's parameter, effective porosity is needed as an important input. In this study, two ways to derive the effective porosities are used: (i) saturation method and (ii) NMR method.

Saturation method: After reaching maximum saturation, all the samples were dried under 60°C to remove the movable water without affecting the CBW and clay mineral transformation ([Dewhurst et al., 2018](#); [Yuan et al., 2018](#)). In this case, only CBW remains after the 60°C drying process in the sample such as the pore water content differs between the maximum saturated state and 60°C dried state. The sample weight difference of these two states represents the effective porosity by considering the density of the pore fluid at 1.145 g/cm<sup>3</sup> (250,000 ppm NaCl at room conditions).

NMR method: it is challenging to accurately measure the CBW volume from NMR on brine-saturated shales due to potential signal overlap between CBW and weakly bound water from small inter-grain pores. The CBW was computed from a specific NMR  $T_2$  cutoff of 0.25 ms on the  $T_2$  spectrum of the fully saturated sample introduced by [Yuan et al. \(2018\)](#) and compared with the NMR  $T_2$  porosity of the same sample after undergoing 60°C drying process (i.e. only CBW signal remaining).

### 4.2.3 POLARIS model

The conductivity of the complex impedance of rock has been understood in terms of the polarisation effects of the Stern layer (the intimal electrical double layer attaching the grain surfaces). Researchers have described the relationship of characteristic relaxation time,  $\tau_0$ , to complex conductivity with the characteristic pore size,  $\Lambda$  ([Koch and Holliger, 2012](#); [Niu and Revil, 2016](#); [Revil and Florsch, 2010](#)) using the POLARIS model, which can be written as:

$$\tau_0 = \frac{\Lambda^2}{2D_{(+)}^s} \quad (4.1)$$

where  $D_{(+)}^s$  corresponds to the diffusion coefficient of the counterions in the Stern layer (in  $\text{m}^2 \cdot \text{s}^{-1}$ ). Equation 4.1 can be written as equation 4.2 when replacing  $\tau_0$  by the characteristic frequency determined from complex conductivity:

$$f_0 = \frac{1}{2\pi\tau_0} \quad (4.2)$$

Characteristic pore size  $\Lambda$  is usually applied as the median value or the peak value of the pore size distribution derived by MICP experiments ([A Revil et al., 2014](#)); cumulative porosity calculated from NMR can also be used to indicate the characteristic pore size ([Weller et al., 2010](#)).

The diffusion coefficient of the counterions in the Stern layer (parameter  $D$ ) is mainly controlled by the sample mineralogy, type and salinity of brine, and temperature ([Niu and Revil, 2016](#)). Since these factors remain unchanged for the same saturated samples under different pressure, a positive correlation between the characteristic frequency with pore size distribution can be derived from equation 4.2 ( $f_0 \propto \Lambda$ ).

## 4.3 Results

### 4.3.1 Sample weight monitoring under pressure

Table 4.1 shows the weight of the tested sample in the 60°C dried state and fully saturated state, indicating the amount of brine intake by the samples. For the first group, samples Th24 and Th25, the weights were tracked for each different confining pressure stage after 14 hours of stabilisation (Figure 4.1). The weight variation trend lines, with a good coefficient of determination ( $R^2$ ) for both samples, illustrate a rapid sample weight loss under low confining pressure up to 1000 psi (up to 0.3% lost), before decreasing much more slowly toward 8500 psi confining pressure (0.02% lost maximum).

**Table 4.1** Sample dimensions, weights at dry and saturated states, and calculated porosity considering brine density of 1.145 g/cc.

Groups	Sample ID	Diameter (mm)	Length (mm)	Vol (ml)	weight-60°C dry (g)	weight-fully saturated (g)	Brine intake (g)	Equivalent porosity from brine intake (%)
1	Th24	38.41	51.26	59.3	144.02	148.82	4.8	7.06%
	Th25	38.3	30.05	34.62	84.66	87.79	3.13	7.92%
2	Th17	38.38	28.51	32.98	80.74	83.88	3.14	8.31%
	Th23	38.3	26.08	30.05	73.3	75.55	2.25	6.54%
	Th28	38.38	28.03	32.43	82.41	85.31	2.9	7.80%

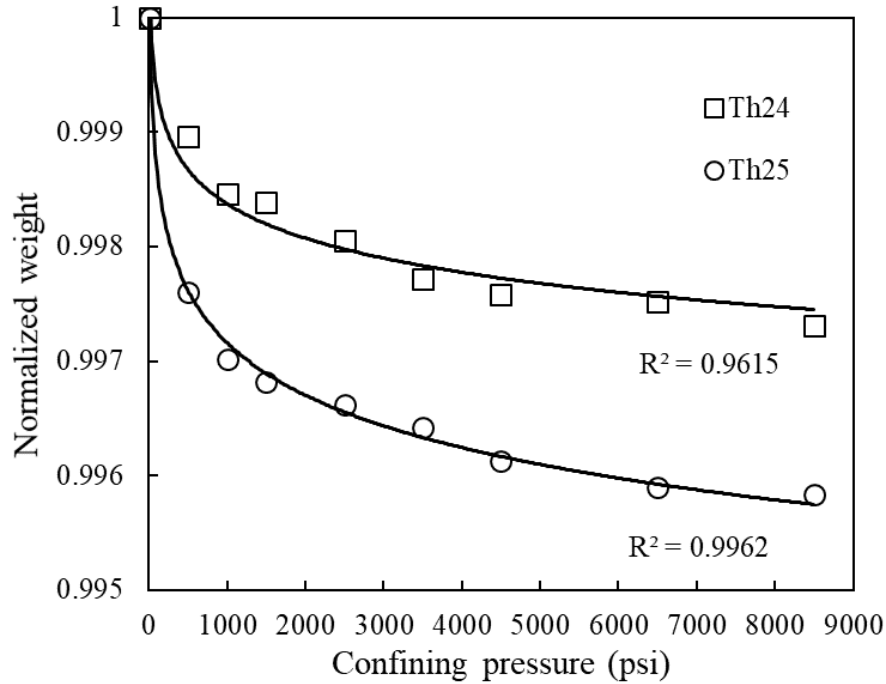


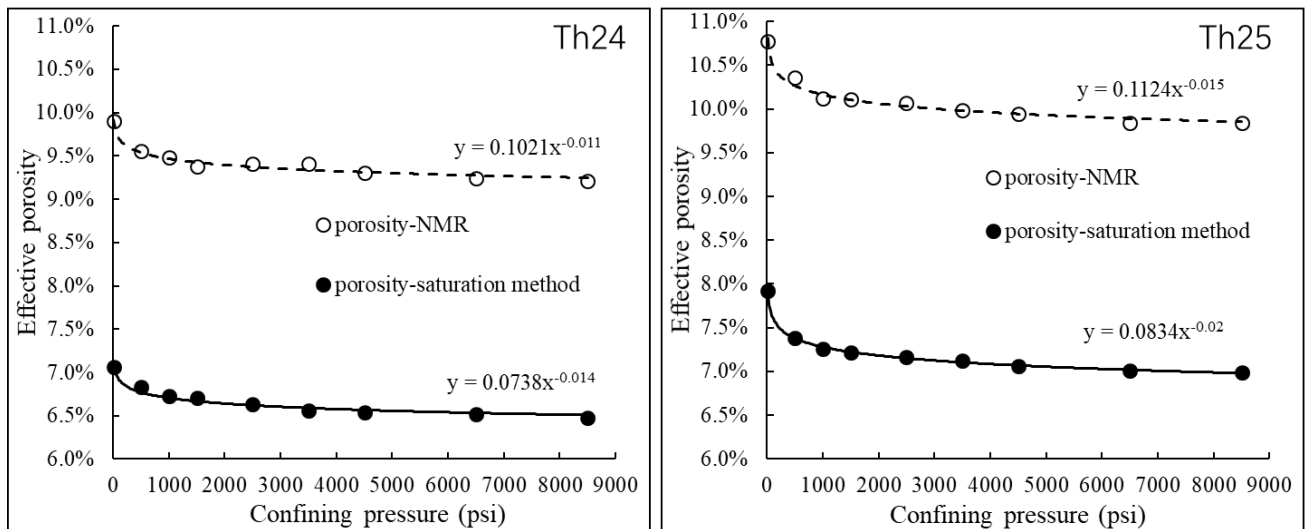
**Figure 4.1** Sample normalised weight monitoring under increasing confining pressures in Group 1 up to 8500 psi. The black curves correspond to a power-law fitting of the data.

### 4.3.2 NMR and saturation porosity

Table 4.2 shows the porosity difference between the NMR method and saturation method. The CBW defined by the total  $T_2$  spectrum cumulative porosity at 60°C dry states differs from the  $T_2$  spectrum cumulative porosity below 0.25 ms relaxation time at maximumly saturated states ( $\pm 1\%$ ). CBW is then excluded from the NMR total porosity to calculate the NMR effective porosity. Notably, the CBW remains the same for the saturated samples at different confining pressure due to its immovable nature; therefore, the same CBW volume is used to calculate effective porosity variation at different confining pressure (Table 4.2). Table 4.2 compares the effective porosity variation of samples Th24 and Th25. These variation trends are similar to the weight changes, while NMR effective porosities are all higher than effective porosities from the saturation method (Table 4.2 and Figure 4.2).

**Table 4.2** Effective porosity ( $\Phi$ ) using NMR and saturation methods on the shale collection.

Groups	Sample ID	NMR porosity-fully saturated	NMR porosity-60°C dry	NMR-CBW (0.25 ms)	Effective porosity from the NMR method		Effective porosity from saturation method	
					$\Phi$	$\Phi$	$\Phi$	$\Phi$
					@ambient	@8500 psi	@ambient	@8500psi
1	Th24	12.41%	2.51%	2.31%	9.90%	9.21%	7.06%	6.48%
	Th25	10.71%	2.96%	2.68%	10.77%	9.84%	7.92%	6.99%
2	Th17	13.72%	3.17%	3.85%	10.55%	9.76%	8.31%	7.30%
	Th23	11.74%	4.76%	3.74%	8.00%	7.52%	6.54%	5.81%
	Th28	13.68%	3.23%	3.57%	10.45%	9.13%	7.80%	6.97%

**Figure 4.2** Comparison of effective porosity between NMR and saturation methods at ambient conditions for Group 1 samples after undergoing confining pressure experiments (i.e. brine expelled from shale compaction/creep).

### 4.3.3 Pore size distribution variation under different confining pressure

The NMR  $T_2$  spectrum can be divided into three pore size populations corresponding to micropores ( $T_2 < 1$  ms), mesopores (1–20 ms), and macropores ( $T_2 > 20$  ms), with  $T_2 > 100$ ms regarded as fracture signals (Song and Kausik, 2019; Tang et al., 2016; Zhang et al., 2017). Figure 4.3 shows the changes in NMR pore size distribution measured at ambient conditions for samples from Group 1 after undergoing different pressures during the impedance measurement exercise. The same NMR pore size distribution graph is presented in Figure 4.4 for the Group 2 samples also measured under room conditions but only in a fully saturated state and after applying 8500 psi confining pressure. Figures 4.2 and 4.3 both indicate that the predominant NMR  $T_2$  population is centered around 1 ms regardless of the confining pressure applied on those samples, suggesting the micropores (and even smaller) are the major pore size in Ordovician Goldwyer shales. The volume changes of micropores at  $T_2 < 1$ ms from the amplitude signal are almost negligible under different confining pressure.  $T_2$  signal ranging between 1 ms and 100 ms, representing the mesopores and macropores, showed a volume reduction and the maximum amplitude shifting toward shorter  $T_2$  after applying 8500 psi confining pressure (dashed lines in Figure 4.4). The relatively strong  $T_2$  signal ( $> 100$  ms) recorded under ambient conditions and up to 500 psi confining pressure became barely detectable under higher confining pressures ( $> 500$  psi).

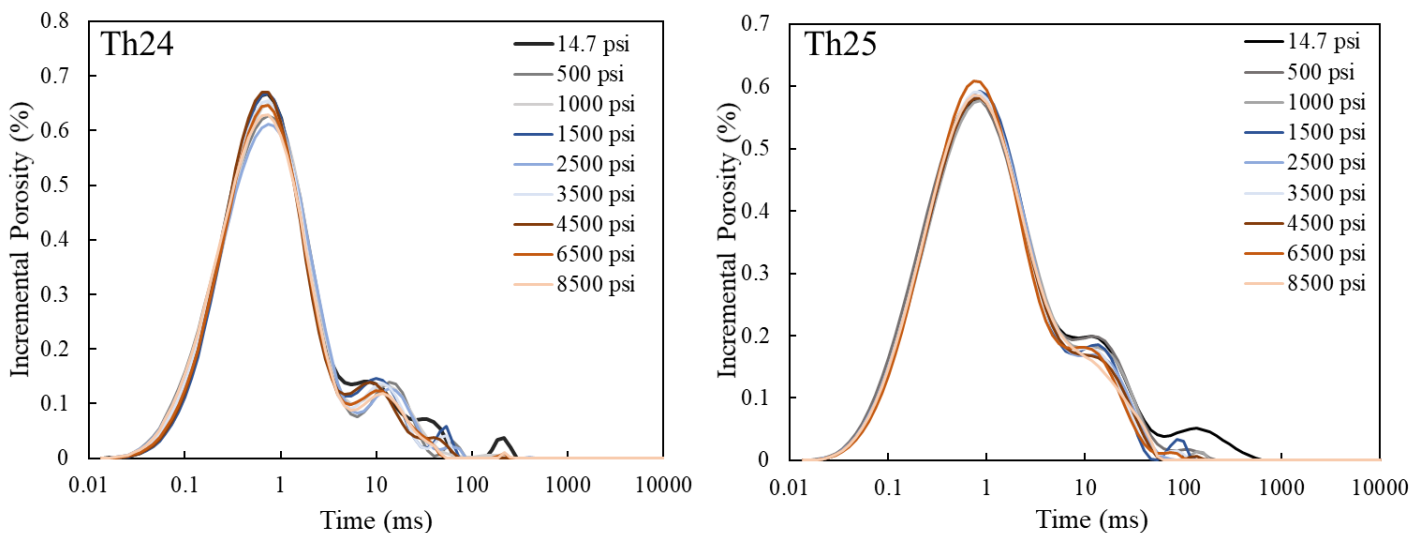


**Figure 4.3** NMR  $T_2$  spectrum of Group 1 samples (Th24, Th25) measured under ambient conditions after undergoing different confining pressures.

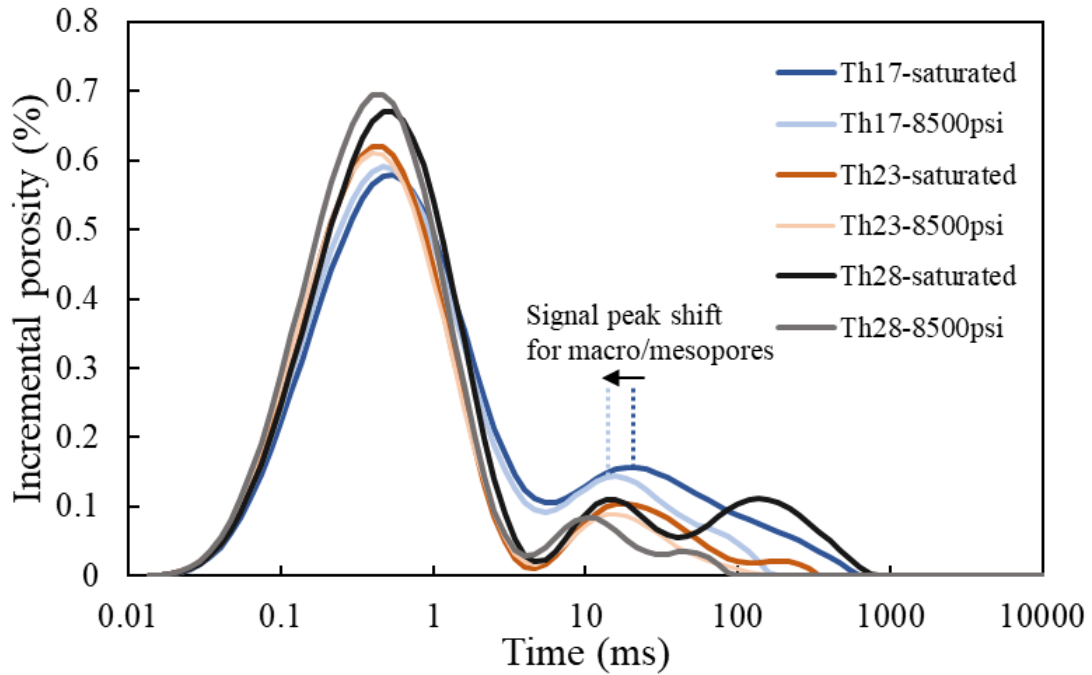


**Figure 4.4** NMR  $T_2$  spectrum of Group 2 samples (Th17, Th23, Th28) measured under ambient conditions on saturated state and after 8500 confining pressure.

#### 4.3.4 NMR $T_1T_2$ spectrum for residual oil detection

In the  $T_1$ – $T_2$  NMR spectrum map, the X- and Y-axes represent  $T_2$  and  $T_1$  relaxation times respectively, with a  $T_1$ -to- $T_2$  ratio = 1 (diagonal line of the plot) when only liquid water occurs. The  $T_1$ -to- $T_2$  ratio moves to higher values when hydrocarbon signatures (oil/gas) are present. NMR  $T_1$ – $T_2$  mapping was measured to track potential residual oil from both cleaned and uncleaned samples. Figure 4.5 shows the  $T_1$ – $T_2$  NMR spectrum for the uncleaned sample, Th17, and the cleaned sample, Th28; the colouring from blue to red represents the relative increasing incremental pore fluid volume intensity recorded in the shales. The circled light blue area for sample Th17 (Figure 4.5) indicates the presence of residual oil in either organic pores and/or oil in inorganic pores in the sample with a  $T_1$ -to- $T_2$  ratio  $\gg 10$  (Kausik et al., 2016; Khatibi et al., 2019); no such hydrocarbon signature is recorded in the cleaned sample (Th28), as indicated by the same oil signal background (dark blue in the circled area).

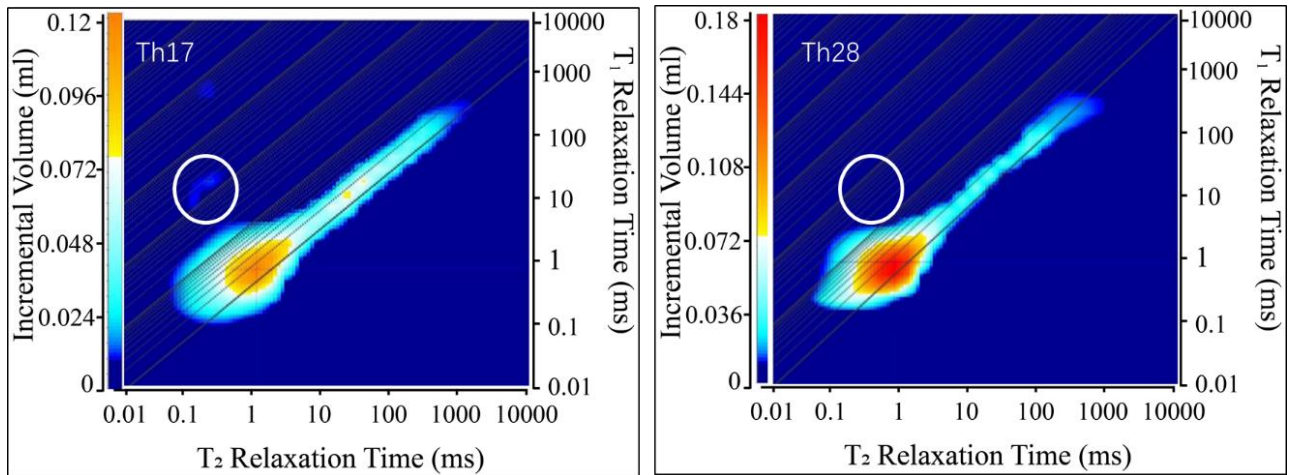


**Figure 4.5** NMR T1-T2 spectrum of the Left) uncleaned sample, Th17, and Right) cleaned sample, Th28. The circled area in the Th17 NMR T1-T2 spectrum exhibits a weak signal relating to the presence of residual oil which is not apparent for sample Th28.

### 4.3.5 Resistivity and formation factor stress sensitivity

#### 4.3.5.1 Characteristic impedance frequency

Figure 4.6-A records the reactance in the range of 0.1 Hz–1000k Hz at different confining pressures of the Group 2 samples (i.e. continuous impedance recording while changing the confining pressure). As defined in the POLARIS model, the characteristic frequency is the coordinate frequency with the lowest reactance value across the whole frequency range. However, the lowest value is not that obvious in Figure 4.6-A; therefore, we averaged the frequency of the four lowest reactances and regarded the averaged frequency as the characteristic frequency in this study. Figure 4.6-B illustrates the calculated characteristic frequency under different confining pressures. All the tested samples in Group 2 show the same decreasing trends under the increasing confining pressure up to ~ 1000 psi, and characteristic frequency remains stable at the increasing confining pressure.

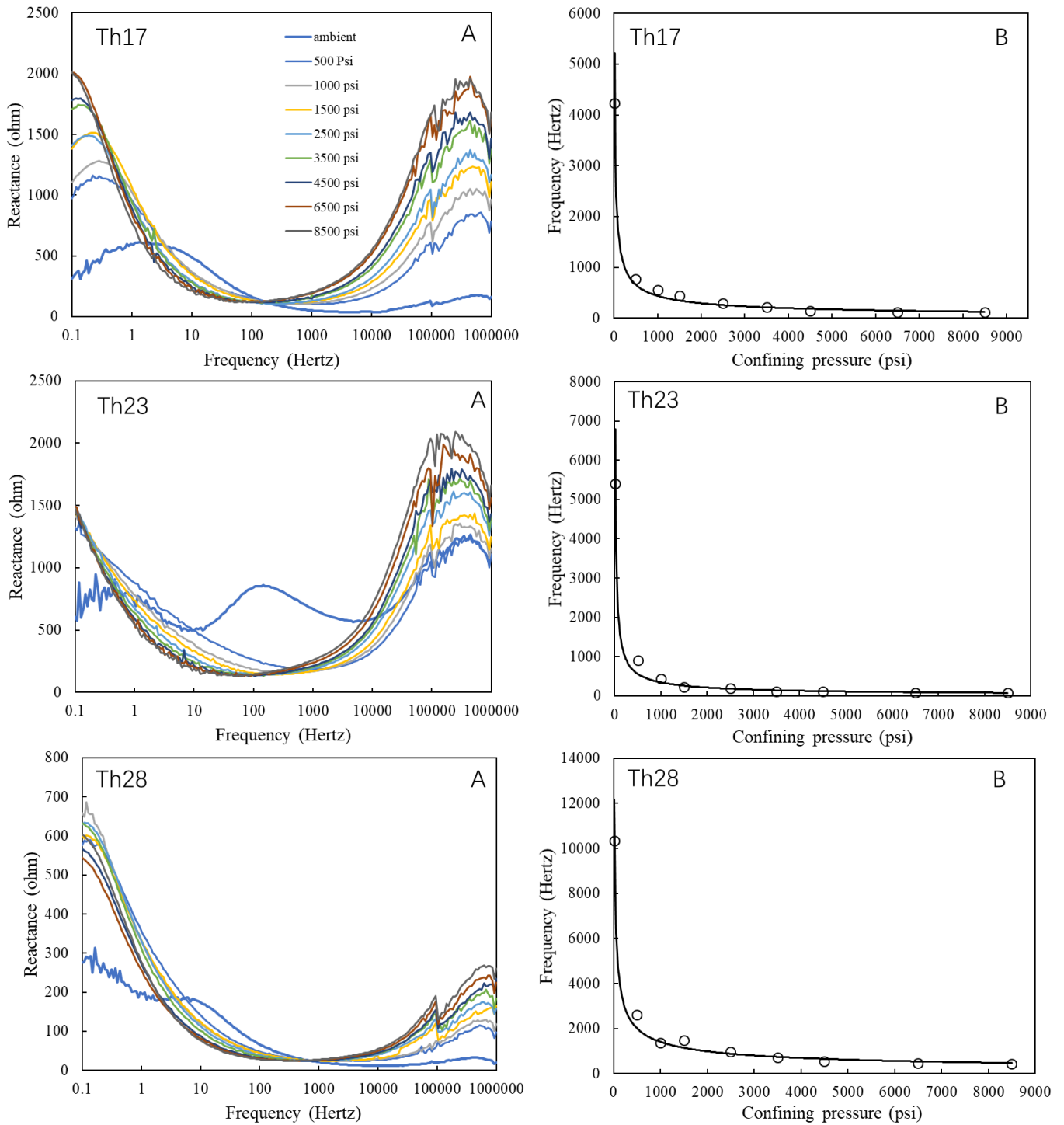


**Figure 4.6** Electrical impedance results under confining pressure in Group 2 samples: (A) Reactance spectrum under different confining pressure; (B) Mean characteristic frequency under different confining pressures.

### 4.3.5.2 Resistivity and Formation Factor

Figure 4.7 shows the electrical resistivity and corresponding formation factor values under different confining pressures for all the tested samples using a constant pore water salinity with a resistivity of  $R_w = 0.042$  ohm.m. The data of resistivity (and formation factor) for all the samples show similar trends, indicating exponential changes with a rapid increase in resistivity under low pressure and slower changes under higher confining pressure. Samples Th24, Th25 and Th28 present lower resistivity from 24.15 to 86.63 ohm-m (formation factor from 575.08 to 2062.71) than samples Th17 and Th23 with resistivity values from 66.18 to 374.56 ohm-m (or formation factor from 1575.82 to 8918.16). However, the observed resistivity slow-down under higher confining pressure ( $> 1000$  psi) is much less intense when the sample has an intrinsic high resistivity to begin with. In other words, the higher the resistivity, the greater the pressure necessary to reach a constant resistivity trend.

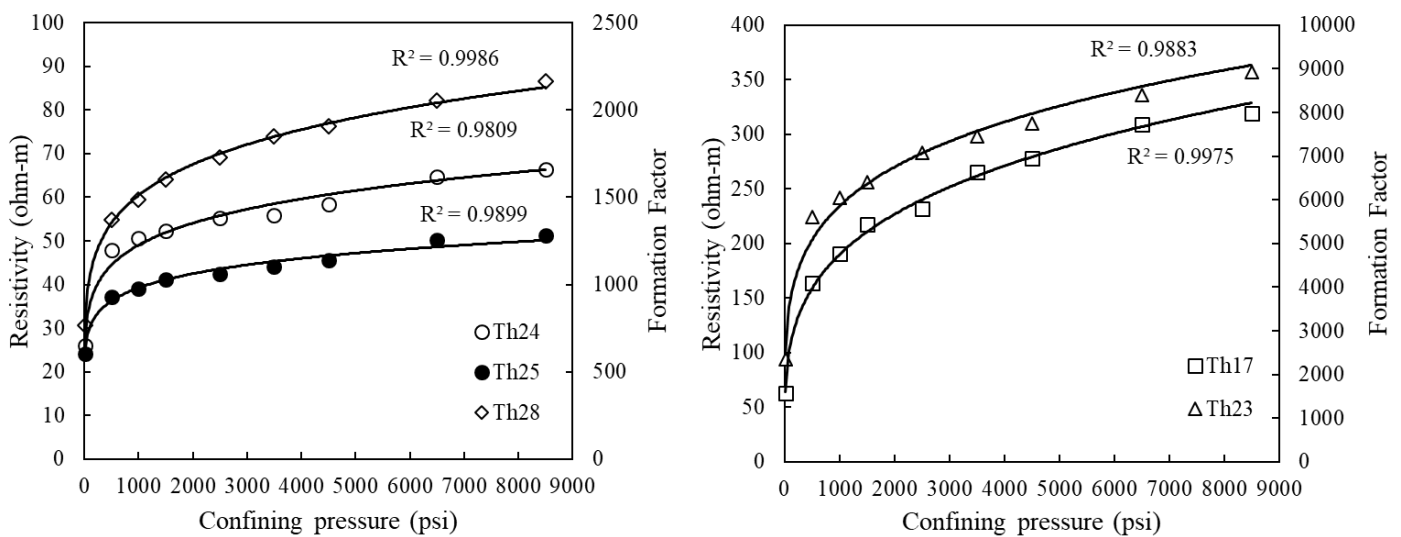


**Figure 4.7** Resistivity and formation factor under increasing confining pressure for all tested samples. Tested samples show similar variation trends with a rapid increase under low pressure and slower changes under higher confining pressure.

---

## 4.4 Discussion

### 4.4.1 Effective porosity from saturation and NMR methods

The effective porosity determined using the NMR method is consistently higher (1.46–2.85%) than that determined by the saturation method for the Group 1 samples (Th24, Th25), as indicated by the similar decreasing trends in Figure 4.1. The similar porosity gap between the NMR method and the saturation method could be explained as an incorrect estimation of CBW by the NMR method. As shown in Table 4.2, CBW porosities derived from NMR  $T_2$  on the 60°C dried samples and derived from NMR  $T_2$  cutoff at 0.25 ms in saturated state show similar values. However, these values are underestimated with respect to porosity derived from the saturation method. Unlike the hydrogen signals in macropores and microfractures, signals in micropores (and CBW) show a very short relaxation time in the NMR  $T_2$  spectrum (Nikolaev and Kazak, 2019), possibly reaching the limits of the 2 MHz NMR instrument. This means the resolution is not high enough to accurately define the limited CBW volume (usually less than 2 ml amount of water within the samples) in the NMR GeoSpec2 apparatus. One other possible issue is that CBW is related to clay minerals that carry most of the paramagnetic signal in shales. Paramagnetic minerals are known to enhance the NMR relaxation, leading to underestimation of CBW (Foley et al., 1996). Since the tested samples have the same amount of clay content/type, it is not surprising to see a similar offset of CBW between NMR and saturation methods. As for Yuan's theory, a  $T_2$  cutoff at 0.25ms may not be an accurate threshold to define the CBW in our study due to differences in mineralogy between Yuan's samples and Theia samples. Therefore, this study prefers the effective porosity derived by the saturation method.

### 4.4.2 Pore size distribution variation under different pressure

The variation in porosity and pore size distribution with increasing pressure was monitored using the NMR  $T_2$  spectrum along with the reactance characteristic frequency. As the confining pressure is increased from ambient up to 500 psi, porosity decreased from 7.06% to 6.84% for sample Th24 and 7.92% to 7.38% for sample Th25. The change in the NMR  $T_2$  spectrum for  $T_2 > 100$  ms is related to a change in porosity caused by the closure of water-filled microfractures with increasing confining pressure (Figure 4.4). However, the NMR  $T_2$  signal from  $T_2 = 0.1$ –100 ms, which is sensitive to water in macropores, mesopores, and micropores, remains unchanged in the same pressure range. As the confining pressure is increased from 500 to 8500 psi, the effective porosity continues to decrease, from 6.84% to 6.48% for sample Th24 and 7.38% to 6.99% for sample Th25

---

(Figure 4.2). However, the NMR  $T_2$  spectrum above 100 ms indicates that the change in porosity from 500–8500 psi is no longer caused by the closure of microfractures (Figure 4.4). The small reduction in porosity and the shift towards shorter NMR  $T_2$ , from the mesopores ( $1 \leq T_2 \leq 20$  ms) and macropores ( $20 \leq T_2 \leq 100$ ms), support a pore body size reduction of those pores under the increasing confining pressure (Figure 4.4). The combination of both porosity reduction (Figure 4.2) and pore size distribution changes (Figure 4.4) under pressure suggests that the compliant nature of clay minerals controls the deformation of pores, leading to the observed porosity reduction when the shales are subjected to confining pressure  $> 500$  psi. The micropores ( $T_2 < 1$  ms) showed a slight  $T_2$  shortening under increasing pressure. A previous study ([Ju et al., 2018](#)), using SEM observations, reported unconnected organic pores could deform and become connected at higher pressure. Such a phenomenon could explain the changes observed in pore size distributions from NMR  $T_2$  spectrum  $< 1$  ms. This does not necessarily mean that the recorded micropore size reduction can be reflected in the 2 MHz NMR  $T_2$  spectrum. Indeed, such very short  $T_2$  relaxation time could be incorrectly recorded by the NMR machine due to: (i) unresolved pore size from the machine itself ( $T_2$  too short to be detectable) and/or (ii) due to the paramagnetic  $T_2$  enhancement from the clay–water interface, which could also change under pressure. Therefore, effective porosity from micropores was regarded as the same regardless of confining pressure.

The characteristic reactance frequency of the samples under different pressure also suggests a change in pore size distribution consistent with the POLARIS model. Figure 4.6 shows the decrease of characteristic frequency under increasing pressure for Th17, Th23 and Th28. All the tested samples show a similar exponential decreasing trend of the characteristic frequency under increasing confining pressure.

In conclusion, as the porosity decrease of Th24 and Th25 shows a rapid drop below 500 psi and a gentle decrease at 500–3500 psi before becoming steady  $> 3500$  psi, it is believed that closure of microfractures dominates the porosity decrease below 500 psi. The subsequent porosity drop at 500–8500 psi is related to the macropore and mesopore size decrease. The micropores or CBW were disregarded as NMR machine limits and/or paramagnetic signal from clay might prevent accurate detection of their pore size reduction.

---

### 4.4.3 Stress sensitivity of resistivity

#### 4.4.3.1 The effects of residual oil on the resistivity

Although all the shale samples were collected from the Goldwyer Formation with nearly similar mineralogy, samples Th17 and Th23 show much higher resistivity than other samples (Figure 4.7). NMR  $T_1$ - $T_2$  results demonstrated the presence of residual oil within the tested samples (Figure 4.5). The uncleaned samples, Th23 and Th17, show oil signals in the NMR  $T_1$ - $T_2$  (Figure 4.5-A), while it is not recorded in the cleaned sample (Th24, Th25, Th28) (Figure 4.5-B). It is believed that high resistivity values might arise from residual oil in Th17 and Th23, even if in trace amounts. Indeed, residual oil as a non-conductive material occupies the pore spaces and blocks the conductive channels, leading to overestimation of the rock resistivity, formation factor and Archie's parameter  $m$ . However, the normalised resistivity under different confining pressure (Figure 4.8) shows similar variation trends (exponential law) for both cleaned samples and uncleaned samples. Similar trends indicate the residual oil is not the dominant influence on how resistivity changes with the increasing pressure, which is instead controlled by the variation of the pore size distribution (as discussed in 4.4.2).

#### 4.4.3.2 The effects of pore size changes on the resistivity

As for the correlation of the porosity reduction with the increase of pressure, the resistivity correlates with porosity changes such that resistivity increases when the porosity decreases (Figure 4.2 and Figure 4.7). Combining the changes of pore size distribution in section 4.2, the rapid variation in both porosity and resistivity below 500 psi seems to correspond to microfractures closure. From 500–3500 psi, the resistivity continues to increase (albeit more slowly) due to the mesopore and macropore size-reduction indicated by the corresponding NMR spectrum and shortening of  $T_2$  ( $1 \text{ ms} \leq T_2 \leq 100 \text{ ms}$ ; Figure 4.4). Beyond 3500 psi confining pressure, the resistivity increase is controlled by the remaining compliant pores up to the maximum pore elasticity regime. The resistivity seems to plateau for some of the samples at 8500 psi confining pressure, while the effective porosity does not change (Figure 4.1). A further increase in confining pressure would likely induce plastic deformation or cause the shale to enter into a brittle regime, where irreversible mechanical damage occurs within the shale. A few of the samples recorded a small, steady increase in resistivity up to the maximum confining pressure of 8500 psi, but the effective porosity changed very little ( $< 0.2\%$ ), corresponding to the remaining compliant pores and pore-throats being able to close.

In all cases, the percolation threshold (where deformation and mechanical damage begins to occur) was not reached. The onset of percolation is usually characterised by a sharp increase in resistivity as the pore-throats collapse, causing a disconnection between the pores (and pore water) which are responsible for the majority of conduction. The change in resistivity during percolation usually occurs simultaneously with a barely detectable change in porosity because the pore-bodies do not collapse ([Pimienta et al., 2017](#)). This phenomenon was not observed during the experiments.

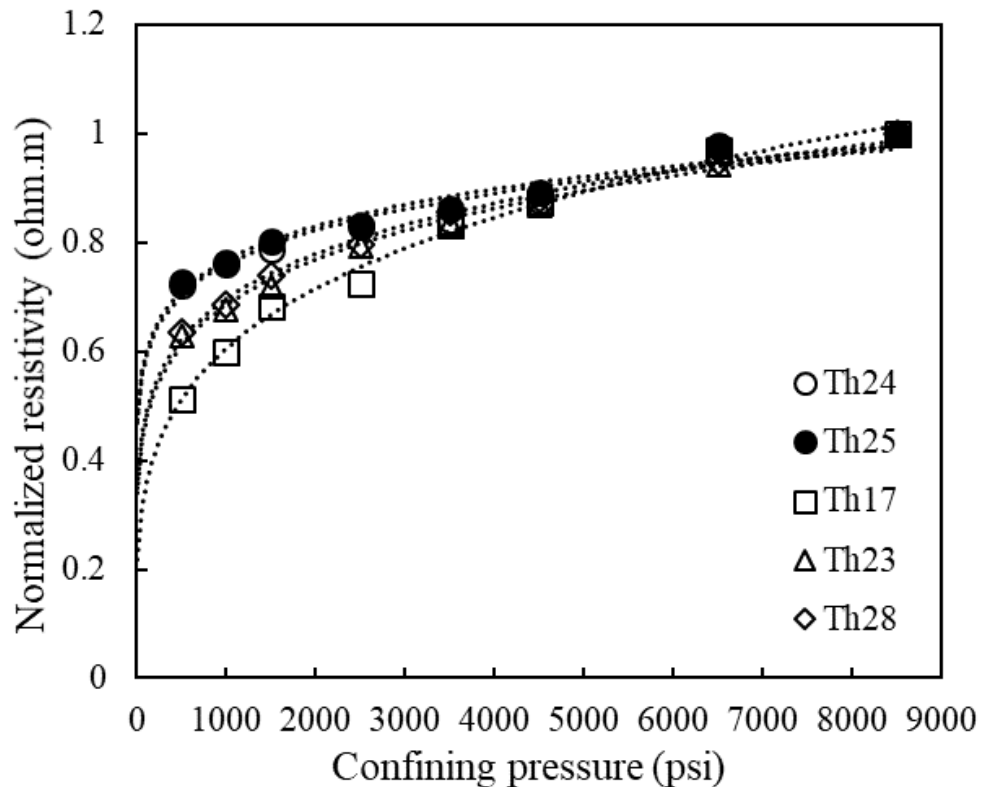


**Figure 4.8** Normalized resistivity under different confining pressure. There is a monotonic increase in normalized resistivity with increasing confining pressure. The increase in normalized resistivity occurs rapidly from 0–500 psi confining pressure but then the rate of increase is less from 500–8500 psi.

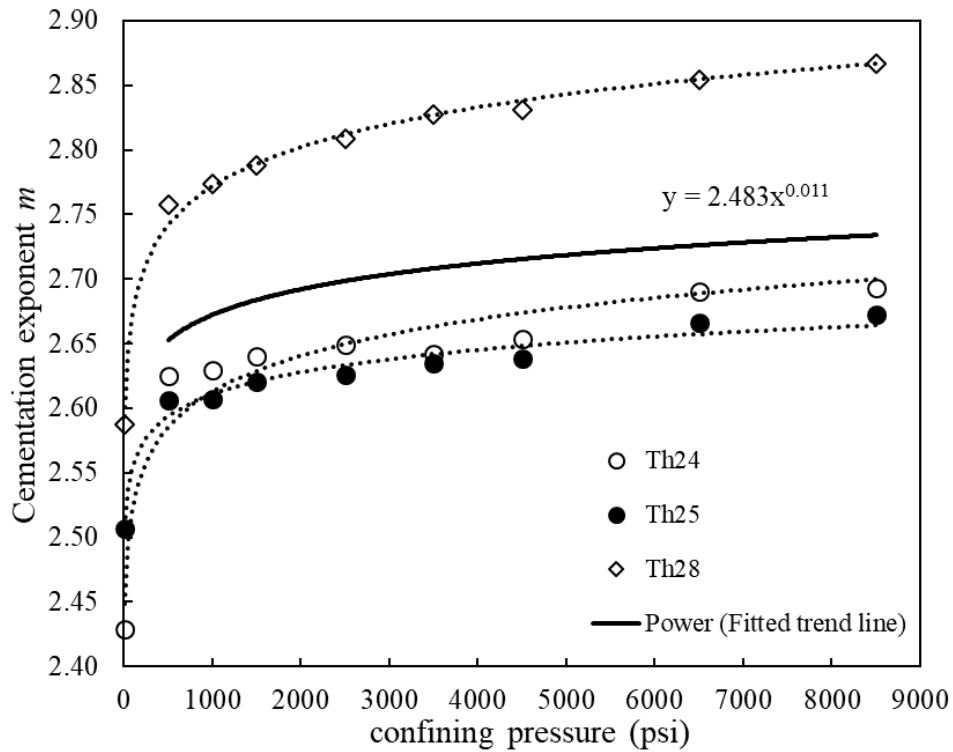


**Figure 4.9** Archie cementation exponent  $m$  under increasing confining pressure for cleaned samples (no residual oil). The increase in cementation exponent  $m$  is rapid from 0–500 psi confining pressure but then the rate of increase is less from 500–8500 psi.

#### 4.4.3.3 Stress sensitivity of Archie cementation exponent

To minimise manual error in resistivity measurements during the sample transfer from each pressure step, continuous measurement of the resistivity was performed on Group 2 samples (Th17, Th23, Th28). In this case, without taking samples out of the core holder during the resistivity measurements the porosity variation under different pressure cannot be obtained for Group 2 samples. We modelled porosity variation during the resistivity measurements based on stress sensitivity of the porosity from Th24 and Th25 (Group 1; Figure 4.1), the porosity data on fully saturated states, and the porosity data measured after the resistivity tests under 8500 psi for Archie's cementation exponent calculation.

Figure 4.9 shows the changes in the calculated Archie's cementation exponent for the cleaned samples with no residual oil under increasing confining pressure with Archie's  $m$  ranging from 2.43 to 2.87. Archie's  $m$  is inevitably higher (typically 2.85 to 3.54) on uncleaned shales, as the

---

residual oil leads to an approximately twofold increase in resistivity compared to the cleaned shales. We remove the  $m$  dataset from confining pressure  $< 500$  psi as they correspond to microfracture response, which leads to the inaccurate porosity and Archie's  $m$  calculation. The general stress sensitivity of Archie  $m$  is similar among the tested cleaned samples, as:

$$m_p = (2.483)P^{0.011} \quad (4.2)$$

where  $P$  is the confining pressure (in psi) and  $m_p$  is the cementation exponent  $m$  under the confining pressure  $P$ .

The relationship for deriving the stress-sensitive Archie's exponent  $m$  (Equation 4.2) from the confining pressure was established using accurate effective porosity determined by saturation method using 2000 psi brine saturation and continuous monitoring of resistivity whilst varying confining pressure. The NMR-helped to narrow the pore topology at work when applying pressure on shales associated with resistivity response. Further studies will help to validate the stress-sensitive Archie's  $m$  relationship provided in Equation 4.2 and will enhance understanding of shale petrophysical characteristics with regards to clay content, clay type, and pore structure. A long-term experimental approach will hopefully address the stress sensitivity of Archie's cementation  $m$  scaled to residual oil signature so that  $m$  can be accurately computed under reservoir conditions for any type of shales, including oil and gas shales.

---

## 4.5 Conclusion

In this study, shales from the Ordovician Goldwyer Formation in the Canning Basin (Australia) were selected for laboratory stress sensitivity measurements of electrical resistivity, porosity and pore-size distribution, as they have very homogeneous clay content at 20–46% illite. Laboratory NMR and electrical resistivity tools were used under controlled confining pressure and shale hydration state to help accurately record the effective porosity (i.e. total porosity excluding clay-bound water porosity) and then compute Archie's cementation exponent  $m$  under reservoir conditions. Induced microfractures from reservoir stress relaxation, sample handling and cleaning processes are fully closed at 500 psi confining pressure. Stress-sensitive electrical properties should be determined for shales at no less than 500 psi. Mesopores/macropores are particularly sensitive to confining pressure range from 500 to 3500 psi due to pore size reduction. Beyond 3500 psi, the pore size change is negligible. Residual oil within the samples increases resistivity but does not affect the pore size distribution under different confining pressure. The variation in shale resistivity at different confining pressure seems to correlate with the closure of microfractures below 500 psi (strong and rapid resistivity response), followed by mesopores/macropores size reduction at 500–3500psi. Above 3500 psi, the few remaining compliant pores and pore-throat reduction slowly change the resistivity/Archie's  $m$  responses. Plastic/brittle regimes are not yet reached at 8500 psi confining pressure with respect to the observed steady slow increase of resistivity with pressure. Archie's  $m$  stress sensitivity shows a similar trend among the tested samples. An empirical formula is developed to predict Archie's  $m$  under different reservoir pressures for cleaned shales as:  $m_p = (2.483)P^{0.011}$  with pressure  $P$  in psi.

---

## **Chapter 5**

# **The salinity dependence of electrical conductivity and Archie's cementation exponent for shale**

---

---

## 5.1 Introduction

One of the best solutions to the global energy shortage is the production of unconventional resources ([Tahmasebi, 2018](#)), including shale gas and oil ([Rezaee, 2015](#)). Many studies have characterised shale physical properties ([Hu et al., 2017](#); [Josh et al., 2019](#); [Josh et al., 2012](#); [Wu et al., 2019](#); [Yang et al., 2020](#); [Zou et al., 2017](#); [Zou et al., 2018](#)). However, in relation to electrical properties gaps in our understanding remain. As a common petrophysical parameter, electrical resistivity is often used to evaluate reservoir fluid saturation in conventional reservoir rock types; however, these procedures are not well suited to shales. For example, [Archie \(1942\)](#) developed a simple model to estimate the water saturation of clean sandstone by using parameters ( $a$ ,  $m$  and  $n$ ) that relate to rock and fluid properties. Cementation exponent  $m$  (a dimensionless factor) is difficult to define because it varies for different rock types ([Abdassah et al., 1998](#)) and is believed to vary with the shape and size of grain particles ([Friedman, 2005](#); [Jackson et al., 1978](#)). For this reason,  $m$  may range from 1.6 to 2.3 for sandstones and 2.3 to 3 for carbonates ([Moradzadeh and Bakhtiari, 2011](#)).

Apart from pore geometry, the surface conductivity of the grains plays an important role in shale matrix conductivity ([Revil et al., 1998](#); [Waxman and Smits, 1968](#)). This factor is believed to be the main reason Archie's equation is less accurate for shaly formations. However, when the pore water salinity increases, the conductivity of pore water becomes more significant than the surface conductivity, and the relationship between rock conductivity and pore water conductivity becomes linear ([Cherubini et al., 2019](#); [Coperey et al., 2019](#); [Rembert et al., 2020](#); [Waxman and Smits, 1968](#)). Therefore, the contribution from surface conductivity is reduced by increasing the pore water salinity and Archie's equation becomes more applicable. By applying the same theory, our previous work has derived the cementation exponent for Goldwyer shale by suppressing the surface conductivity under high pore water salinity (250,000ppm) ([Zhong et al., 2021](#)). However, the relationship between surface conduction, bulk rock conductivity and the formation water salinity remains unclear. The purpose of this study is to compare the electrical conductivity, formation factor and cementation exponent for shales of different mineralogy, and evaluate the significance of surface conductivity on the shale conductivity.

## 5.2 Volume averaging approach theory

The volume averaging approach ([Revil and Glover, 1997](#); [Revil, Soueid Ahmed, et al., 2018](#)) was developed based on previous studies ([Johnson et al., 1986](#); [Johnson and Sen, 1988](#); [Pride, 1994](#); [Waxman and Smits, 1968](#)) for the electrical conductivity of porous media in the non-linear region depicted in Figure 5.1. This approach also defines the concept of an iso-conductivity point, which is a specific case whereby the surface conductivity equals the pore water conductivity. Two equations corresponding to high salinities (i.e. pore water salinity higher than the iso-conductivity point) and low salinities (i.e. pore water salinity lower than the iso-conductivity point) are then divided for the comparison.

The volume averaging approach starts with the situation that the solid phase is insulating, which means surface conductivity is temporary and is not considered. The electrical conductivity and formation factor in Equation 2.2 can be expressed as the summing of local Joule dissipation of energy:

$$\sigma \left( \frac{\Delta\psi}{L} \right)^2 = \frac{1}{V} \int_{V_p} \sigma_w |e_b|^2 dV_p \quad (5.1)$$

$$\frac{1}{F} = \frac{1}{V} \int_{V_p} |\nabla \Gamma_b|^2 dV_p \quad (5.2)$$

where  $\Delta\psi$  (in V) corresponds to the difference in local electrical potential,  $L$  (in m) denotes the length of cylindrical,  $V$  (in  $m^3$ ) is the total volume,  $V_p$  (in  $m^3$ ) is the volume of the interconnected pore space,  $e_b$  is the distribution of the electrical field, and  $\Gamma_b$  denotes the normalised electrical potential for a cylindrical. The  $\nabla \Gamma_b$ -field is strong in pore throats and null in pore dead-ends, indicating that the formation factor would be higher in less connective pore structures and even approach infinity when pores are disconnective ([Revil, Soueid Ahmed, et al., 2018](#)).

To discuss the impact of the extra surface conductivity provided by the electrical double layer on the mineral surface, the local electrical conductivity distribution can be written as follows:

$$\sigma_{(x)} = \sigma_w + \sum_s \delta_{(x)} \quad (5.3)$$

where  $\sigma_{(x)}$  is the local conductivity,  $\sum_s$  is the surface conductivity in S, and  $\delta_{(x)}$  is the delta function characterising the position of the mineral surface. When the salinity of pore water is high, the local conductivity  $\sigma_{(x)}$  can be replaced by the conductivity of pore water  $\sigma_w$  regarding the

normalised local electrical potential, while  $\Gamma_b$  (unitless) remains roughly the same (Figure 5.2-A). Therefore, the conductivity can be expressed as follows:

$$\sigma \left( \frac{\Delta\psi}{L} \right)^2 = \frac{\sigma_w}{V} \int_{V_p} |e_b|^2 dV_p + \frac{\Sigma_s}{V} \int_S |e_b|^2 dS \quad (5.4)$$

$$\sigma = \frac{\sigma_w}{V} \int_{V_p} |\nabla\Gamma_b|^2 dV_p + \frac{\Sigma_s}{V} \int_S |\nabla\Gamma_b|^2 dS \quad (5.5)$$

Similarly, as seen in Figure 5.2-B, under low salinity situations – where the pore water salinity is lower than the iso-conductivity point – the conductivity can be expressed by the local electrical potential  $\Gamma_s$  (unitless) of the distribution of the electrical field  $e_s$  (in  $\text{V m}^{-1}$ ):

$$\sigma \left( \frac{\Delta\psi}{L} \right)^2 = \frac{\sigma_w}{V} \int_{V_p} |e_s|^2 dV_p + \frac{\Sigma_s}{V} \int_S |e_s|^2 dS \quad (5.6)$$

$$\sigma = \frac{\Sigma_s}{V} \int_S |\nabla\Gamma_s|^2 dS \left[ 1 + \frac{\sigma_w \int_{V_p} |\nabla\Gamma_s|^2 dV_p}{\Sigma_s \int_S |\nabla\Gamma_s|^2 dS} \right] \quad (5.7)$$

Comparing with Archie's law  $F = \Phi^{-m}$  with  $m \geq 1$  (equation 2.2 when  $a=1$ ), the volume averaging approach postulates a parameter equivalent to Archie's law, called the surface formation factor  $f$  (i.e.  $f = (V_p/S\Phi)^p$  with  $p \geq 1$ ). Then equation 5.8 and 5.9 are developed since Joule dissipation of energy can be minimised by the electrical conduction ([Revil and Glover, 1997](#)):

$$\frac{\Sigma_s}{V} \int_S |e_b|^2 dS \geq \frac{\Sigma_s}{V} \int_S |e_s|^2 dS \quad (5.8)$$

$$\frac{\sigma_w}{V} \int_{V_p} |e_s|^2 dV_p \geq \frac{\sigma_w}{V} \int_{V_p} |e_b|^2 dV_p \quad (5.9)$$

By comparing equation 5.8 and equation 5.9 with equation 5.3, we can conclude that under the same pore structure conditions,  $f_h$  (surface formation factor  $f$  at high-salinity pore water)  $\geq f_l$  (surface formation factor  $f$  at low-salinity pore water), and  $F_l$  (formation factor  $F$  at low-salinity pore water)  $\geq F_h$  (formation factor  $F$  at high-salinity pore water).

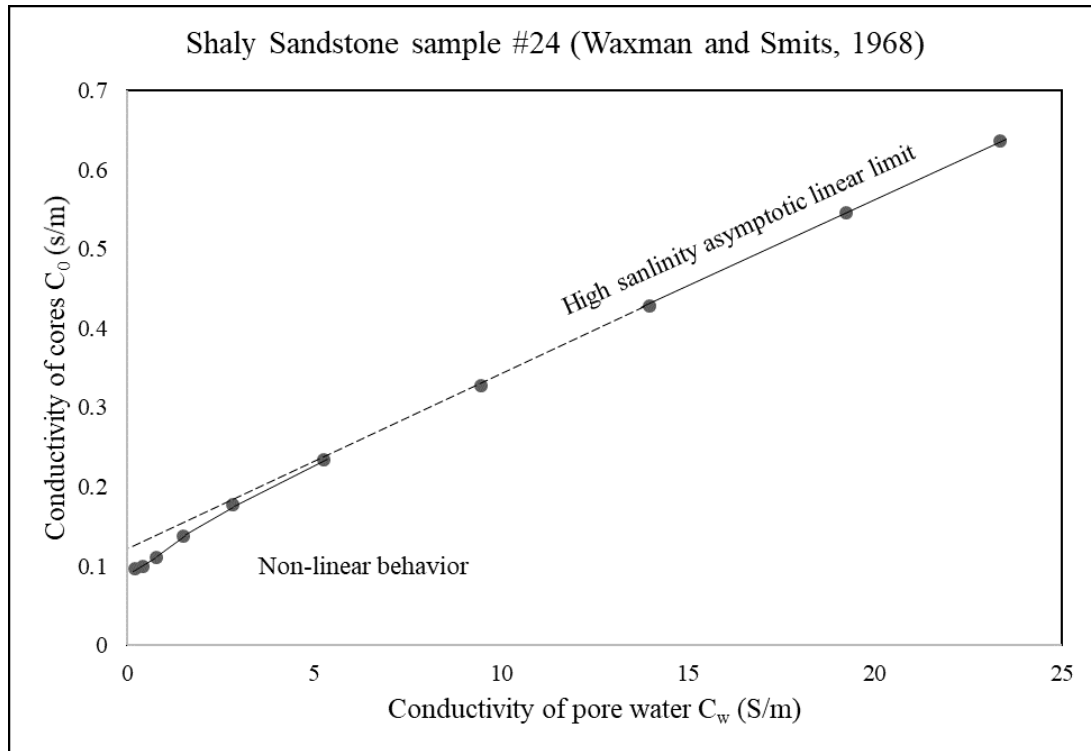


**Figure 5.1** The non-linear behavior between the conductivity of saturated cores and its pore water. The dashed line is the extension of the asymptotic line at high salinities called Archie's line in this paper. The tested data below Archie's line. Data from [Waxman and Smits \(1968\)](#).

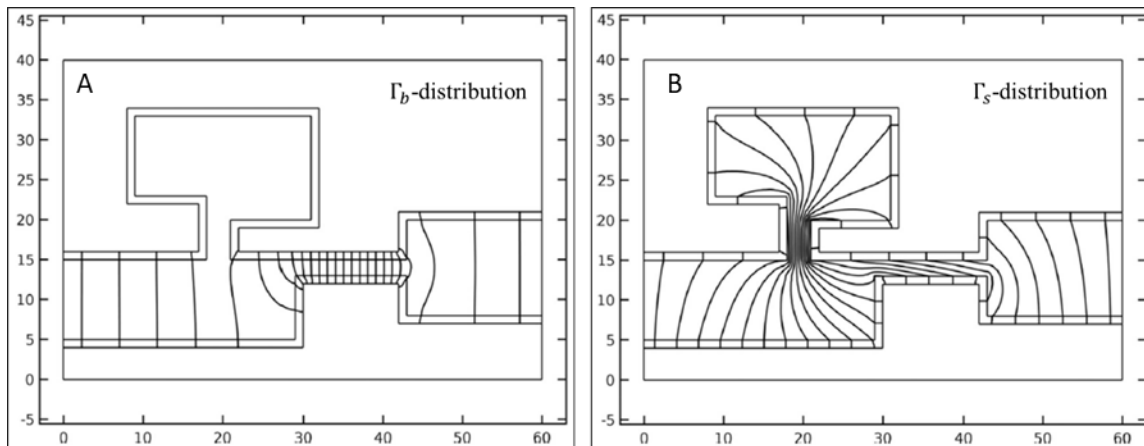


**Figure 5.2** A-Normalised potential  $\Gamma_b$  distribution under high salinity conditions. The local electrical field is strong within the pore throat while negligible in the dead-ends; B-Normalised potential  $\Gamma_s$  distribution under low salinity conditions. Figures from ([Revil, Soueid Ahmed, et al., 2018](#))

---

## 5.3 Methodology

A total of 6 unpreserved disc shales were recovered: (i) 4 samples from the Ordovician Goldwyer Formation of Theia#1 from the Canning Basin, Australia, from a depth of about 1500 m, (ii) one sample from the Eagle Ford shale outcrop from Western Gulf Basin, America. X-ray diffraction (Table 5.1) data are collected from similar depths from the XRD database of the Government of Western Australia Department of Mines, Industry Regulation and Safety, and the experimental results provided by Kocurek Industries INC from which we obtained the outcrop samples. The XRD data show that the Theia#1 samples are illite-rich shale, the Eagle Ford sample is calcite-rich shale.

The experimental procedures are as follows. 1) The unpreserved samples were dried under 60°C for over 48 hours to remove the weakly bound water while maintaining the clay-bound water (CBW), and the dried sample weights were then recorded; 2) Samples were air-vacuumed for 24 hours in the saturation cells before injection and saturation with NaCl brine at 2000 psi hydrostatic confining pressure, maintaining the constant fluid pressure with ISCO syringe pump. Our previous study has shown that the shale sample can be maximally saturated within 7–14 days. Since samples in this study are disc samples with short lengths, 7 days were chosen to saturate all the samples. The weights of saturated samples were then recorded. 3) The samples were transferred into the Viton jacket with electrode platens in contact on the sample end surfaces and placed in a pressure vessel between two hydraulic pistons separated by PEEK plugs for electrical insulation (Figure 2.2-B). 4) We selected 2800 psi as the confining pressure for the tests based on the depth of Theia#1 samples and three measured principal stresses in the Canning Basin under this depth ([Bailey and Henson, 2019](#)). The impedances were recorded in potentiostatic mode with constant 1 V excitation and 1 kHz frequency using an LCR-819 spectrometer (Gw Instek Ltd.) under room temperature (25°C) when the data stabilised. This usually takes 12–14 hours, which has been verified by our previous work. 5) Procedures 1–4 were then repeated while saturating the samples with increasing NaCl brine salinity (i.e. 35 g/l, 50 g/l, 70 g/l, 120 g/l and 250 g/l). Nuclear magnetic resonance (NMR) was measured for the maximally saturated samples to detect the pore-size distribution. The NMR  $T_2$  spectrum was measured using Carr, Purcell, Meilboom and Gill (CPMG) pulse sequence ([Carr and Purcell, 1954](#); [Kenyon et al., 1995](#); [Meiboom and Gill, 1958](#)), with 114  $\mu$ s inter-echo spacing (TE), 500 ms inter-experiment delay, 4389 number of echoes and a minimum of 100 signal-to-noise ratio (SNR).

**Table 5.1** Shale mineralogy

Sample ID	Quartz (%)	Kaolinite (%)	Illite/Mica (%)	Smectite (%)	Chlorite (%)	Total Clay (%)	Carbonate (%)	Pyrite (%)	Other minerals (%)
Th24	18.34	0.3	24.34	0.98	5.64	31.26	35.57	2.32	12.51
Th25									
Th37	21.61	0.15	45.47	0.71	N/A	46.33	14.21	2.42	15.43
Th39	18	1	56	N/A	3	60	7	3	12
EF1	11	2	2	N/A	3	7	78	1	3

## 5.4. Results

### 5.4.1 Effective porosity calculation

Table 5.2 shows the sample characteristics and the weight differences between before and after saturation conditions of all tested samples. Clay-bound water must be excluded from the total porosity to define effective porosity ([Ellis and Singer, 2007](#)). Therefore, effective saturation porosity was used as the input for Archie's equation.

**Table 5.2** Dimensions, weight, and saturation porosity of the studied samples.

Shale formation	Sample ID	Depth (m)	Plug diameter (mm)	Plug length (mm)	Plug volume (cm <sup>3</sup> )	Dry Weight (g)	Brine saturated weight (g)	Effective porosity
GOLDWYER	Th24D	1510.54	38.38	10.22	11.8	28.79	29.79	8.47%
	Th25D	1512.7	38.38	10.39	12.08	29.36	30.31	7.87%
	Th37D	1554.73	38.38	10.38	12.19	29.3	30.29	8.12%
	Th39D	1563.3	38.38	10.25	12	29.1	30.08	8.14%
Eagle Ford	EF1	Outcrop	37.8	11.1	12.46	31	31.25	2.10%

## 5.4.2 Nuclear magnetic resonance (NMR)

Previous studies have shown that the NMR  $T_2$  relaxation is related to the pore-size distribution of micropores ( $T_2 < 1$  ms), mesopores (1–20 ms), and macropores ( $T_2 > 20$  ms);  $T_2 > 100$  ms can be regarded as fracture signals (Song and Kausik, 2019; Tang et al., 2016; Zhang et al., 2017). As shown in Figure 5.3, for most of the samples (excluding EF1), the largest proportion of the signals comes from the micropores (i.e.  $T_2 < 1$  ms). The signals of mesopores (1–20 ms) and macropores ( $T_2 > 20$  ms) are still considerable, while only limited microfracture signals can be found beyond 100 ms. Sample EF1 shows a higher proportion of mesopores and macropores than micropores, but the signals for microfracture are less significant, which is similar to other samples.

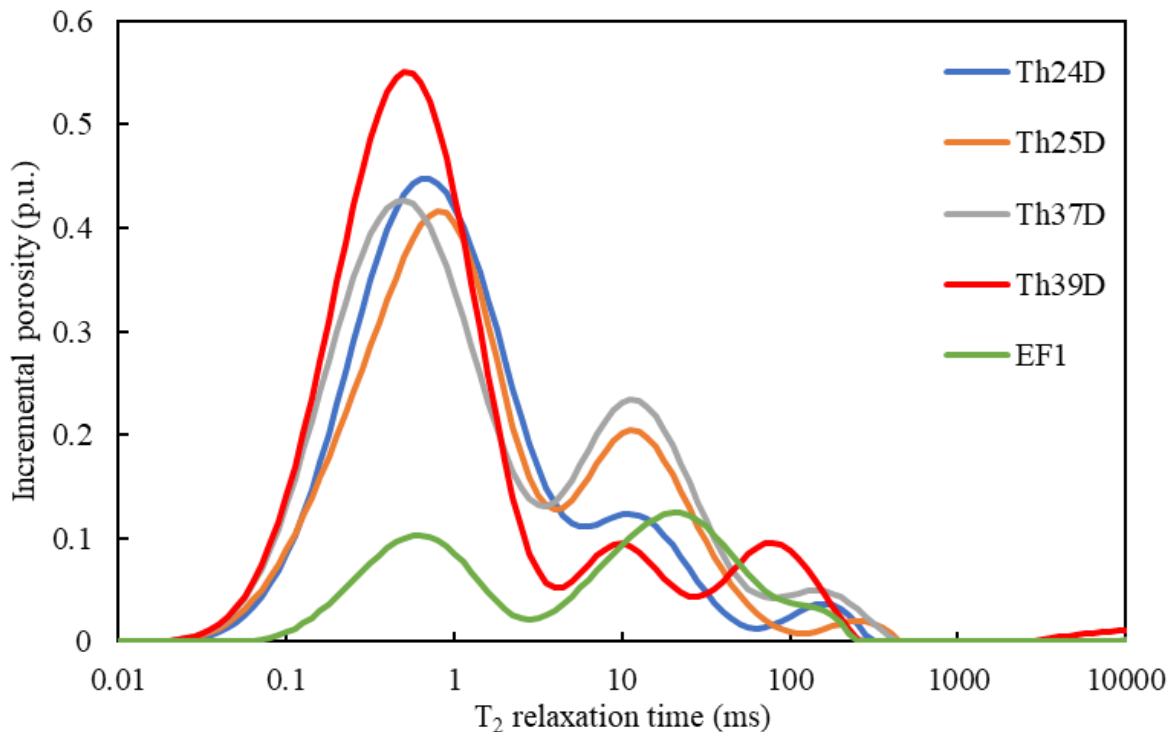


**Figure 5.3** Pore-size distribution by NMR  $T_2$  spectrum for the studied samples.

## 5.4.3 Electrical conductivity and apparent formation factor

Figure 5.4 illustrates the variation trends of the electrical conductivity of samples saturated with different brine salinity, and Figure 5.5 correspondingly shows the calculated apparent formation factor under different salinity; the raw data are posted in Table 5.3. Notably, resistivity data shown in Table 5.3 are reciprocal to those applied in Figure 5.4. For the accuracy of data, we kept three decimal places for resistivity. However, the number of decimal places for these data becomes very large when we derive electrical conductivity. Therefore, we chose to present resistivity rather than

electrical conductivity in Table 5.3. For the convenience of comparison with previous studies, the figures are presented as electrical conductivity.

As indicated in Figure 5.4, the electrical conductivity of saturated samples increases with the increasing pore water salinity, as expected. While all the trend lines are concave, the slopes indicating the reciprocal of apparent formation factor  $F_a$  (based on Equation 2.5) increase at low salinity and remain more linear at high salinity. Figure 5.5 shows these trends more clearly; decreasing trends can be found at low salinity from 35000 ppm to 50000 ppm (except for EF1, where the apparent formation factor decreased until 70000 ppm) and these trends increase constantly at higher salinity.

**Table 5.3** Summary of resistivity and apparent formation factor for samples saturated with different pore water salinities. Eagle Ford sample presents higher resistivity and correspondingly apparent formation factor than other samples.

Sample ID	Salinity	35000 ppm (35g/l)	50000 ppm (50g/l)	70000 ppm (70g/l)	120000 ppm (120g/l)	250000 ppm (250g/l)
Th24	$R_0$ (ohm.m)	278.81	189.61	138.56	93.03	73.35
Th25		275.48	180.83	138.41	95.87	68.59
Th37		780.19	573.89	445.60	333.25	247.43
Th39		562.43	454.64	354.97	262.76	194.93
EF1		1314.30	920.01	394.80	261.85	207.56
Th24	Apparent Formation Factor	1593.22	1354.37	1385.58	1476.64	1746.52
Th25		1574.15	1291.64	1384.06	1521.76	1633.11
Th37		4458.23	4099.18	4456.00	5289.73	5891.23
Th39		3213.87	3247.41	3549.74	4170.79	4641.08
EF1		7510.27	6571.49	3947.95	4156.33	4941.86

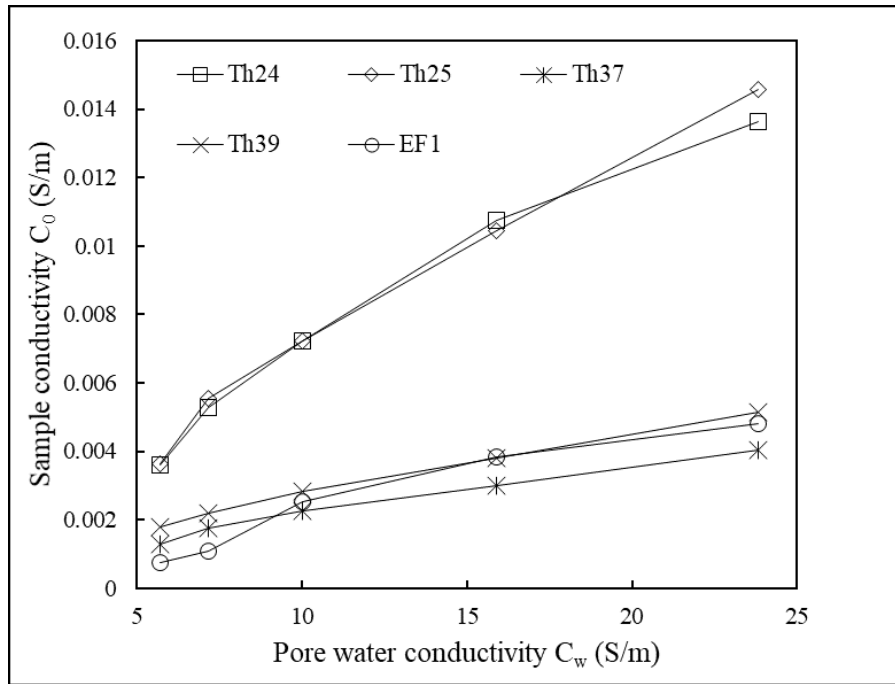


**Figure 5.4** The electrical conductivity of saturated samples  $C_0$  (S/m) at different pore water salinity  $C_w$  (S/m). The sample conductivity increases monotonically with increasing pore-water conductivity for all of the samples, and in some cases (Th24, and Th25) the relationship is more rapid as the pore water conductivity increases from 5–7 S/m but rolls off at higher pore-water conductivity.

## 5.5 Discussion

### 5.5.1 The variation of electrical conductivity at different salinities

As the example shown in the high salinity case (over 15 S/m) in Figure 5.1, the relationship between the pore water conductivity and fully saturated core conductivity is linear, for all of the different types of rocks ([Fayyaz et al., 2019](#); [Revil et al., 1998](#); [Revil et al., 2017](#); [Waxman and Smits, 1968](#); [Waxman and Thomas, 1972](#)). These linear trends indicate that Archie's equation is applicable at high salinity, where the excess conductivity from CEC is negligible ([Ellis and Singer, 2007](#); [Revil et al., 1998](#)) and, therefore, the dominant conductive contribution is water-filled pore channels (Table 5.3 and Figure 5.4). For the convenience of the presentation, we use rock resistivity in Table 5.3, while these values are converted into conductivity in the Figures to better compare with previous studies. At low salinity, the surface conductivity theory predicts the bulk conductivity of the sample above the Archie line (the dashed line in Figure 5.1), because the surface conductivity dominates the overall rock conductivity ([Ghorbani et al., 2018](#); [Komori et al., 2013](#); [Revil and](#)

Florsch, 2010; Revil, Soueid Ahmed, et al., 2018). The data presented in Figure 5.4 indicates that the sample bulk conductivities are below the Archie line and in contradiction to the surface conductivity theory.

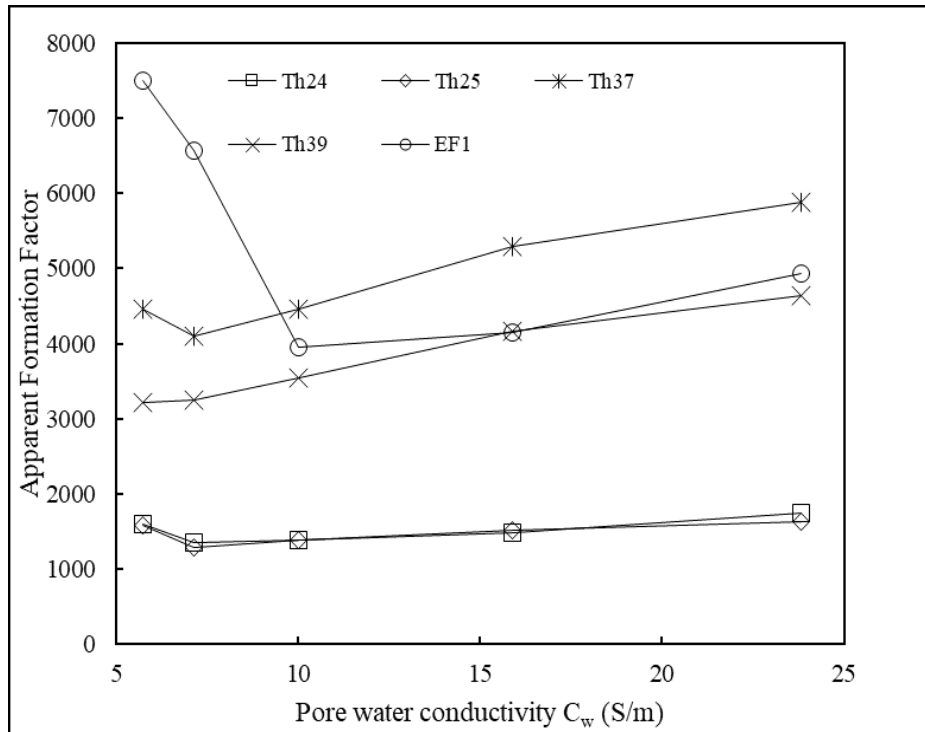


**Figure 5.5** The calculated apparent formation factor  $F_a$  (unitless) under different pore water conductivity,  $C_w$  (S/m). The samples typically exhibit two distinct conduction regimes. In the vicinity of  $C_w = \sim 7\text{--}10\text{S/m}$ , the relationship between the Apparent formation factor and the Pore-water conductivity transition from a decreasing relationship to an increasing relationship. For each sample, the transition occurs at a different pore water conductivity. For sample EF1 this transition occurs at  $C_w = 10\text{ S/m}$  (relatively high) and for Th39 it is not apparent within the measurement range.

The concave trend lines in Figure 5.4 are a result of the variation of electrically conductive channels at different salinity, explained by the volume averaging approach. In the high salinity case, the electrical behaviour is linear. Conduction is via the effective pore channels rather than from water in dead-end pores (Figure 5.2-A). The surface conductivity can be treated as a part of pore water conductivity sharing the same conductive channels, but only provides a limited contribution to the total conductivity. The significance of surface conductivity is weak compared to that of the pore water conductivity.

In the low salinity case, the observed rock conductivity is lower than expected relative to the Archie line. This is caused by, electrical conduction bypassing the dead-end and otherwise less connected pores, whilst the surface conductivity is still passing along the mineral surfaces, including those of the dead-end pores (Figure 5.2-B). Surface conductivity is comparatively strong and contributes the rock bulk conductivity. However, both surface and pore-water conduction take place through less connected pore structures resulting in longer conduction pathways at low salinity, leading to a reduction of the bulk conductivity of the saturated rock. Notably, the model described in the volume averaging approach ([Revil, Soueid Ahmed, et al., 2018](#)) has two boundary conditions: (i) low pore-water salinity ( $\sim 0.01$  S/m, i.e. lower than the iso-conductivity point at 0.09 S/m) and (ii) high pore water salinity (10 S/m). Our study starts with the seawater salinity (around 5.71 S/m), which is a much higher salinity than that of the low boundary situation. However, we still believe the volume averaging approach is applicable in our study for two main reasons: 1) pore structure in our case is smaller in scale (nanometer to micrometer scale) and more complex than shaly sandstones discussed in the model. Such shale complexity leads to less effective pore structures at the cost of more expected dead-end pores, which can only be neglected for higher pore-water salinity. 2) the tested shale samples have much higher clay content than the sandstone for which the volume averaging theory applies. Therefore, the surface conductivity is expected to be stronger in shales. In this case, surface conductivity is much higher, and can only be neglected when the pore water salinity is as high as 200,000 ppm ([Keelan and McGinley, 1979](#)).

### **5.5.2 The variation of apparent formation factor at different salinities**

As seen in Figure 5.5, the apparent formation factor decreases at low salinities and then stabilises at high salinities. As described by Waxman and Smits ([Waxman and Smits, 1968](#)), the apparent formation factor ( $F_a$ ) is contributed to by the intrinsic formation factor of pore geometry ( $F$ ) and surface conductivity ( $\sigma_s$ ). The electrical contribution of surface conductivity was then postulated as the surface formation factor ( $f$ ) equivalent to Archie's law by the volume averaging approach ([Revil, Soueid Ahmed, et al., 2018](#)). In this case, the apparent formation factor ( $F_a$ ) is controlled by the pore channel formation factor ( $F$ ) and the surface formation factor ( $f$ ).

At low salinities, the apparent formation factor ( $F_a$ ) decreases with the increasing pore water salinity (Figure 5.5) due to the mixed effects of the pore channel formation factor ( $F$ ) decrease and the surface formation factor ( $f$ ) increase. In this case, both surface conductivity and pore water conductivity pass around the dead-end pores (Figure 5.2-B). When the pore water salinity increases,

electrical paths shift to more effective pores. The surface conductivity and pore water conductivity in the dead-end pores become insignificant to total conductivity. As seen in Figure 5.5, the decrease of  $F_a$  for sample EF1 stopped at pore water salinity 10 S/m, while that of the other samples stopped at 7.143 S/m. This results from the differences in pore-size distribution, as indicated by the NMR  $T_2$  spectrum (Figure 5.3) showing a higher proportion of macropores (10–100 ms) in EF1, while other samples are dominated by micropores (0.1–1 ms). We assume that all the pore channels are nearly the same size while EF1 has larger dead-end pores due to a higher proportion of macropores. The electrical conductivity of the dead-end pore with a smaller pore size is much easier to neglect than that of the effective pore channel. For the electrical contribution of the pore water in larger dead-end pores, higher pore water salinity states are needed to limit the electrical contribution of larger size dead-end pores. Notably, as described in the volume averaging approach, the apparent formation factor ( $F_a$ ) shows overall decreasing trends with the surface formation factor ( $f$ ) increase and the pore channel formation factor ( $F$ ) decrease, indicating that the significance of  $F$  outweighs  $f$ .

At high pore water salinity conditions, the apparent formation factor ( $F_a$ ) increases and becomes more stable (Figure 5.5). In this conduction regime, conduction occurs via the connected pores (Figure 5.2-A). As the salinity is increased, the contribution of pore channel formation factor ( $F$ ) dominates the surface formation factor ( $f$ ), indicated by a more linear trendline of apparent formation factor at high salinity (Figure 5.5). In this case, Equation 2.2 can be simplified to classic Archie's equation (Equation 2.1) showing the intrinsic formation factor at high salinity ([Revil et al., 1998](#)). Therefore, especially for the shaly sandstone, the intrinsic formation factor can be derived usually in two ways: 1) the slope of the linear relationship between rock conductivity vs pore water conductivity at high salinity, and 2) the apparent formation factor at extremely high salinity. Previous studies ([André Revil et al., 2014](#); [Revil et al., 2013](#); [Waxman and Smits, 1968](#)) for conventional rocks found a constant variation of apparent formation factor at around 1- 10 S/m. However, for the shales investigated in this study, the apparent formation factor is still increasing in the pore water salinity range up to 250g/L (Figure 5.4).

### **5.5.3 The variation of Archie's cementation exponent $m$ at different salinities**

Unlike bulk rock conductivity, Archie's cementation exponent,  $m$ , exhibits insignificant dependence on pore-water salinity (Table 5.4 and Figure 5.6). The Theia#1 samples (Th24, Th25, Th37, Th39), all exhibit a similar porosity of approximately around 8 %, and a relatively high Archie Exponent

---

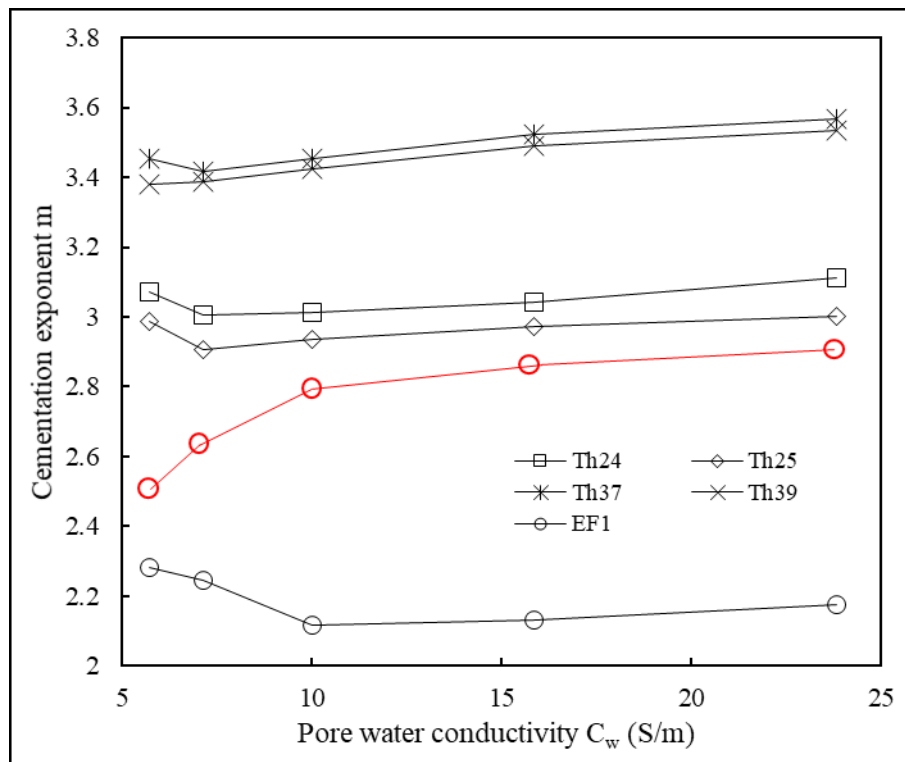
of  $m = 2.9\text{--}3.6$ , compared with the Eagle Ford sample due to its high  $F_a$  (Figure 5.5), showing a low Archie Exponent of approximately  $m = 2.2$ . The discrepancy in  $m$  values for the studied shale samples could be related to the variation in mineralogical composition and the presence of minor conductive minerals. Theia#1 samples show higher content of conductive minerals like pyrite than EF1, leading to lower rock resistivity and higher  $m$ . The increased clay content of the Theia samples compared with the outcrop sample leads to an increased  $m$ . These phenomena indicate that mineralogy affects the cementation exponent. The origin of the mineralogy and associated texture (detrital versus authigenic minerals, diagenetic fluid history) might also govern to some extent the cementation exponent.

In shaly formations, the Waxman & Smits or the Simandoux models are typically preferred to the Archie model because they are better suited to well log interpretation when the clay is present. However, our study indicates that CEC associated with clays is not the primary effect on Archie's cementation exponent  $m$  in shale formations supported by the limited changes of cementation exponent  $m$  (0.1–0.15) under increasing pore water salinities. The CEC increases the rock conductivity. Its effect is weaker at high salinity (70,000ppm–250,000ppm) indicated by the minor change of  $m$  (Figure 5.6) when most of the dead-end pores are neglected (as discussed in 5.1). At low salinity (35000ppm–50000ppm) where CEC is considerable, the CEC contribution to the rock conductivity is overlapped by the conductive contribution of dead-end pores, leading to an overall decrease in  $m$  as the pore water salinity is increased.

In conclusion, we believe the surface conductivity provided by CEC has only limited effects on the calculation of the cementation exponent for shale samples. The CEC effects are outweighed by the variation in conductive channels at low salinity. Additionally, the increase in Archie's  $m$  from low salinities to high is not obvious.

**Table 5.4** Calculated Archie's cementation exponent

Sample ID	Salinity	35000	50000	70000	120000	250000
		ppm (35g/l)	ppm (50g/l)	ppm (70g/l)	ppm (120g/l)	ppm (250g/l)
	$C_w$ (S/m)	5.714	7.143	10	15.873	23.81
Th24D		3.072	3.004	3.014	3.04	3.11
Th25D		2.986	2.906	2.934	2.973	3.001
Th37D	Cementation exponent $m$	3.452	3.418	3.452	3.523	3.567
Th39D		3.381	3.386	3.423	3.491	3.535
EF1		2.281	2.247	2.117	2.13	2.174

**Figure 5.6** The variation of Archie's cementation exponent at different pore water salinity.

Archie's cementation exponent  $m$  is decreasing with increasing pore-water salinity up to a transition value of typically  $C_w = 7\text{--}10$  S/m, above which  $m$  is monotonically increasing with

---

increasing pore water conductivity. The transition value of  $C_w$  is different for each sample, but the Eagle Ford sample, EF1 exhibits the highest transition  $C_w$  of  $\sim 10$  S/m. The expected relationship between cementation exponent and pore-water conductivity should be monotonically increasing (similar to the red line presented) if the presence of CEC associated with clays were in fact the dominating the bulk conduction.

#### 5.5.4 Limitations

We discussed the influence of CEC on shale resistivity and the calculation of Archie's  $m$  in this study. Our study did not plan to start from the pore water salinity as low as the iso-conductivity (0.09S/m) due to the consideration of sample damages during multiple re-drying and re-saturation. For the same reason, we did not set sufficient tests on the high salinity to form the trend line to derived the intrinsic formation factor. Therefore, how exactly rock conductivity changes at different pore water salinity and whether CEC effects for shale results in similar changes as other types of rock filled with pore water under the iso-conductivity still need more tests. Besides, readers should be aware that this paper aims to investigate how Archie's  $m$  vary under different pore water salinities to guide the well-log interpretation, and our tested samples were oil-shale without a cleaning procedure. Therefore, Archie's  $m$  in this study is overestimated because of the residual oil contents. The evidence of the residual oil existence and applicable Archie's  $m$  to the well-log should refer to our previous work ([Zhong et al., 2021](#)).

---

## 5.6 Conclusion

A collection of 4 shale samples from the Goldwyer formation and 1 outcrop sample (from Eagle Ford) provide the basis for a study of electrical conductivity response against pore water salinity. The sample collections contain carbonate-rich shale and clay-rich shale. The samples were dried and then re-saturated with ranges of different brine salinities and investigated with NMR to evaluate the pore size distribution. A comprehensive study of the electrical properties indicates that the bulk electrical conductivity of the samples decreases as the pore-water salinity increases up to a pore-water salinity of typically 7–10 S/m, above which the bulk electrical conductivity begins to increase with increasing pore-water conductivity. The formation factor,  $F$ , and Archie cementation exponent,  $m$ , correspondingly show similar, but reversed trends determined from the calculation.

The currently accepted reason why the Archies equation does not correctly interpret resistivity logs in shaly units is that the presence of clay provides additional conduction pathways via CEC and surface conduction. Our investigation demonstrates that although CEC increases bulk rock conductivity but it has a minor influence on Archies cementation exponent  $m$  (0.1–0.15). We observed a decreasing relationship between  $m$  and the pore-water salinity,  $C_w$ , for values up to approximately  $C_w = 7–10$  S/m. This contradicts the commonly held belief that that CEC dominates conduction, for which case, Archies cementation exponent,  $m$ , should be monotonically increasing with increasing pore-water salinity.

---

## **Chapter 6**

# **Application for Archie cementation exponent in well-log interpretations of shale reservoirs**

---

---

## 6.1 Introduction

Archie's model was originally validated for clean sandstone, to fit this model, we analysed the clay mineral influences to the Archie cementation exponent  $m$  for shale from the pressure-sensitivity aspect and its pore water salinity dependency. We tried to simplify our approach by excluding the influence of conductive clay-bound water (surface conductivity developed by CEC) using high pore water salinities (250,000 ppm). In high salinity the only conductive contributor would be pore water filling the effective pores, therefore, the volume of clay-bound water should be excluded. Our cementation exponent was derived based on the effective porosity (clay-bound water excluded porosity), however, in the formation evaluation cases, clay-bound water is hard to be precisely calculated and excluded from total porosity leading to inaccurate well-log interpretation. Archie's cementation exponent is a complex parameter that depends on many factors such as pore geometry and rock composition. As to the relationship between rock resistivity and rock mineralogy, [Kadkhodaie and Rezaee \(2016\)](#) suggest that, unlike clay minerals that introduce some excessive conductivity to the rock, total organic carbon (TOC) does the opposite job. A similar finding was reached for shaly sandstones ([Shumskayte and Glinskikh, 2016](#)). [Han et al. \(2007\)](#) discussed the effects of pore-size distribution on rock resistivity by controlling the water saturation of the sandstones. For carbonate, samples with equal porosity showed varying resistivities explained by the density of the pore network. The size of pores and the size of pore throats affect the resistivity by limiting the electric flow ([Verwer et al., 2011](#)). The relationship between specific surface areas, CEC and complex conductivity has been discussed ([Revil, Coperey, et al., 2018](#)), and supported by the dynamics simulations of a montmorillonite/water interface ([Tournassat et al., 2009](#)).

In this chapter, we verify the applicability of the findings of previous studies regarding the relationship between rock resistivity and rock mineralogy to our shale samples. Also, the cementation exponent derived from both total porosity and effective porosity was compared, these parameters were then applied in different water saturation models. The discussion guides the readers on how should they define cementation exponent on the samples with different components and how should they choose proper water saturation models by using these cementation exponents.

## 6.2 Results

### 6.2.1 Shale composition

The mineralogical composition of the studied samples is shown in Table 2.2. X-ray diffraction shows all the samples are illite-rich shale. Theia#1 samples contain 14.94–21.61 wt% quartz, 24.3–55.8 wt% mixed illite, a negligible amount of kaolinite and smectite (Database of Government of Western Australia Department of Mines, Industry Regulation and Safety). The Encounter#1 shales' average mineral composition is 25 wt% quartz, 10 wt% kaolinite, 35 wt% mixed-layer illite–mica, and 17 wt% mixed-layer illite–smectite (Josh et al., 2016). Table 6.1 shows the organic geochemical properties of the samples through rock-Eval pyrolysis. The TOC of tested samples ranges from around 1–3 wt%.

**Table 6.1** Rock-eval data for tested samples

ID	S1 - (mg/g)	S2 - (mg/g)	S3 - (mg/g)	PI	Tmax(°C)	HI	OI	TOC(wt%)	MINC(%)
Th24	3.73	4.3	0.44	0.46	445	145	15	2.96	0.62
Th25	3.35	4.04	0.52	0.45	436	173	22	2.34	1.92
Th37	2.84	5.23	0.24	0.35	449	217	10	2.41	1.03
Th39	3.78	6.1	0.33	0.38	445	190	10	3.21	0.87
Th40	1.97	1.2	0.36	0.62	448	117	35	1.03	0.69
Th45	0.16	0.27	0.24	0.37	459	77	69	0.35	0.45
En4441	0.11	0.13	0.2	0.46	607	4	6	3.18	0.54
En4455	0.58	0.21	0.25	0.73	605	13	15	1.62	1.08
En4457	0.26	0.14	0.25	0.65	604	5	8	3.07	0.6

### 6.2.2 Resistivity, formation factor, and Archie's cementation exponent

The resistivity experimental results from fully saturated samples (Th24, Th25, Th40, Th45, En41, En55, En57) at 250,000 ppm under 2800 psi are discussed in Chapter 3. The resistivity was calculated using a constant 1V excitation voltage in potentiostatic mode at 1kHz using an LCR-819 spectrometer (Gw Instek Ltd.) and Autolab PGSTAT30 potentiostat/galvanostat (Metrohm).

The resistivity data, calculated formation factors and Archie's cementation exponent are collected from Chapter 3 and Chapter 5 as presented in Table 6.2.

**Table 6.2** The resistivity, Formation Factor and Archie's cementation exponent at 250,000 ppm NaCl under 2800 psi confining pressure

ID	Ro(ohm-m)	F	m
Th24	57.64	1377.68	3.07
Th25	42.40	1013.41	3.11
Th37D	247.43	5891.23	3.57
Th39D	194.93	4641.08	3.54
Th40	40.29	963.02	3.11
Th45	25.93	619.68	2.96
En4441	217.58	5200.26	2.73
En4455	234.37	5601.50	2.55
En4457	266.50	6369.57	2.61

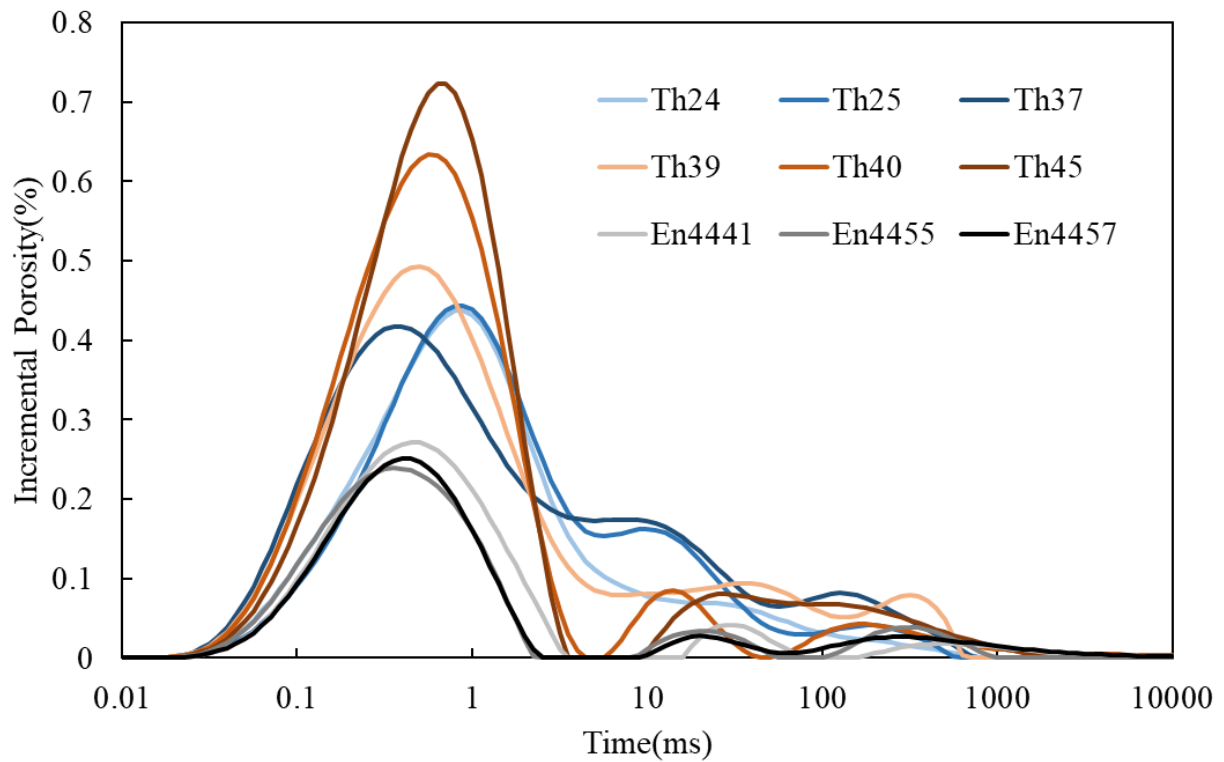


**Figure 6.1** The pore-size distribution by NMR.

### 6.2.3 Pore-size distribution (PSD)

Pore-size distribution was measured based on different relaxation times of the NMR  $T_2$  spectrum. The NMR  $T_2$  spectrum can be divided into three pore size populations corresponding to micropores ( $T_2 < 1$  ms), mesopores (1–20 ms) and macropores ( $T_2 > 20$  ms), with  $T_2 > 100$ ms regarded as fracture signals (Song and Kausik, 2019; Tang et al., 2016; Zhang et al., 2017). Figure 6.1 shows the incremental porosity at different relaxation times and Figure 6.2 calculates the proportion of different pores. As can be seen in Figure 6.2 micropores are the main pore type for all the tested samples. Under 2800 psi confining pressure, most of the microfractures are closed presented by the negligible signals  $>100$  ms (Figure 6.1). For this reason, the microfractures are not considered in Figure 6.2.

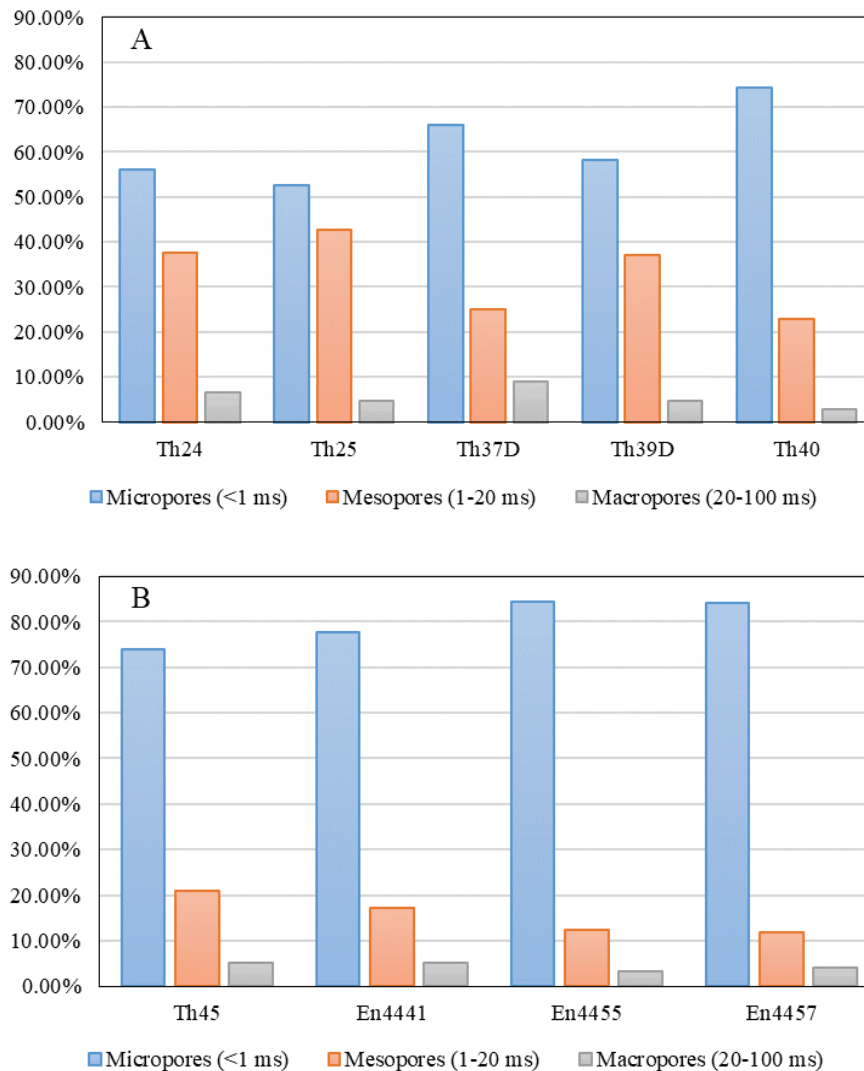


**Figure 6.2** The calculated proportion of micropores (<1 ms), mesopores (1–20 ms), and macropores(20–100 ms) defined by NMR

---

## 6.3 Discussion and conclusion

### 6.3.1 Effects of shale composition on Archie's cementation exponent

As seen from Figure 6.3, a negative correlation is found between quartz content and the Archie cementation exponent  $m$ . While no solid relationship can be found between total clay contents and Archie's  $m$ , likewise to the relationship between illite and Archie's  $m$ . For most of the clean sandstone, Archie's  $m$  is reported close to 2. In our cases, this value is around 2.5 for the samples with 50% quartz contents, and Archie's  $m$  increases from 2.5 with a lower quartz proportion. It is then reasonable to regard quartz as the matrix of the rock controlling the main pore channels, while other particles complex the channels leading to higher  $m$ . However, the increasing complexity can not be explained by different clay components as shown in Figure 6.3B, subject to its dominant clay type (illite) as indicated in Figure 6.3C. This could be because rock electrical conductivity is a very complex parameter controlled by multiple factors including not only the clay particles contribution but also the contributions of other particles (i.e. pyrite, TOC, and carbonate). Organic matters (OM) richness were measured by Rock-eval pyrolysis indicated by total organic carbon (TOC). [Firdaus \(2015\)](#) separated the kerogen from samples and tested the electrical resistivity of the kerogen with different maturity. He concluded that kerogen is a resistive component within the rocks before it becomes over-mature at very high temperatures. In our cases, Tmax data indicates the Theia's samples are within the oil window whereas Encounter's samples are overmature (Table 6.1). In other words, OMs in Theia's samples are insulator whereas they are conductive material in Encounter samples. This finding can be further supported by the correlation between TOC and  $m$  in Figure 6.3D. All the Theia's samples (except for Th45 with low TOC contents) with high resistive OM included in set A show a positive correlation. While an opposite correlation is found for Encounter's samples together with sample Th45 in set B. Besides, conductive OM may result in the underestimation of  $m$  for Encounter samples, since the conductive nature of OM will increase the bulk rock's resistivity. In this case, electrical currents shortcut their pathway resulting in less tortuous pore channels and thus low  $m$ , which can no longer represent the pore structure property in shale. In summary, we find quartz contents and conductive OM are negatively correlated to Archie's  $m$  for shale, while high resistive OM is positively correlated to  $m$ , and no obvious correlation was found for clay minerals.

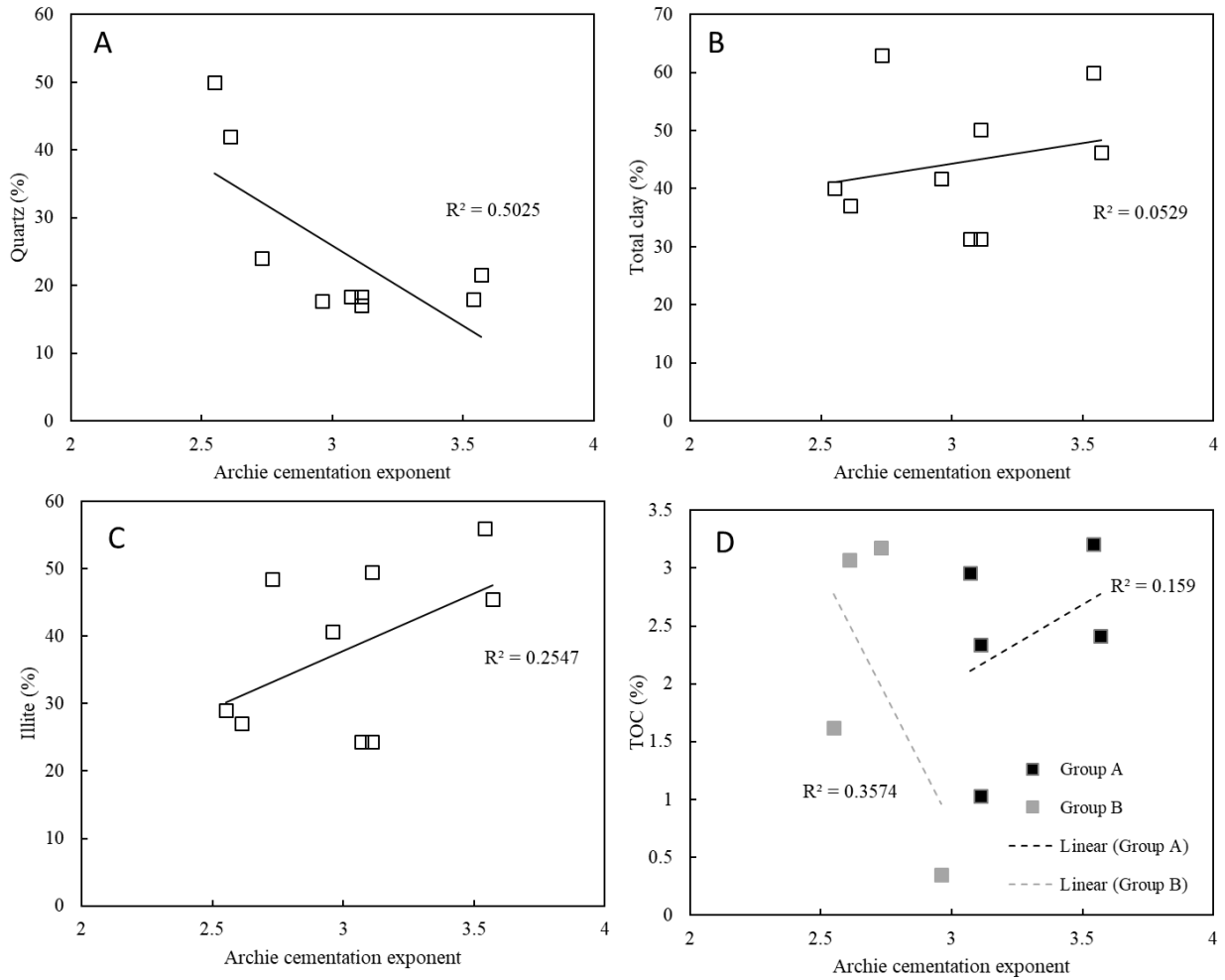


**Figure 6.3** Correlations between A-quartz proportion and Archie's  $m$ ; B-total clay proportion and Archie's  $m$ ; C-illite proportion and Archie's  $m$ ; D-TOC and Archie's  $m$ . Set A includes samples Th24, Th25, Th37D, Th39D, Th40 (black square and black dashed line). Set B is for samples Th45, En4441, En4455, En4457 (grey square and grey dashed line).

### 6.3.2 Effects of PSD on Archie's cementation exponent

To investigate the effects of shale pore-size distribution on Archie's cementation exponent, saturated samples were tested by NMR. We choose the proportion of different pore size rather than the absolute volume of different pores for two reasons: (i) all the tested samples have different porosities, leading to the insignificance of the absolute values for the different size of pores; and (ii) the Archie cementation exponent is not related to the volume of pores but is a normalised parameter with the porosity and formation factor. By correlating the proportion of the pores with Archie's  $m$  (Figure 6.4), we observed negative correlations between the proportion of micropores and Archie's  $m$ , while mesopores and macropores show opposite trends. A previous study on the tortuosity of the samples with spherical particles but different particle size ratios by applying the

discrete element method (DEM) concludes that the number of large particles increases the maximum tortuosity values regardless of the particle distribution (Zharbossyn et al., 2020). This conclusion explains our observation that shale samples with a high micropore proportion are less tortuous showing lower Archie's  $m$ , and samples with a higher proportion of mesopores and macropores are more tortuous with higher Archie's  $m$ . Another explanation could be the existence of organic pores in micropore size. As we discussed in 6.3.1, set B samples are more mature than set A samples and showing a higher proportion of micropores in set B samples (Figure 6.2). When the rock becomes mature, more organic pores developed leading to a higher proportion of micropore in shale samples. Meanwhile, conductive OM results in lower rock resistivity and lower  $m$ . This could be the reason with increasing the proportion of micropores  $m$  decreases. Notably, although the coefficient of determination is not high in Figure 6.4, the correlations between PSD and Archie'  $m$  are still acceptable because PSD is not the only factor controlling Archie's  $m$  but related to clay mineralogy, TOC, etc. (King Jr et al., 2015; Liu et al., 2018; Yuan et al., 2019).

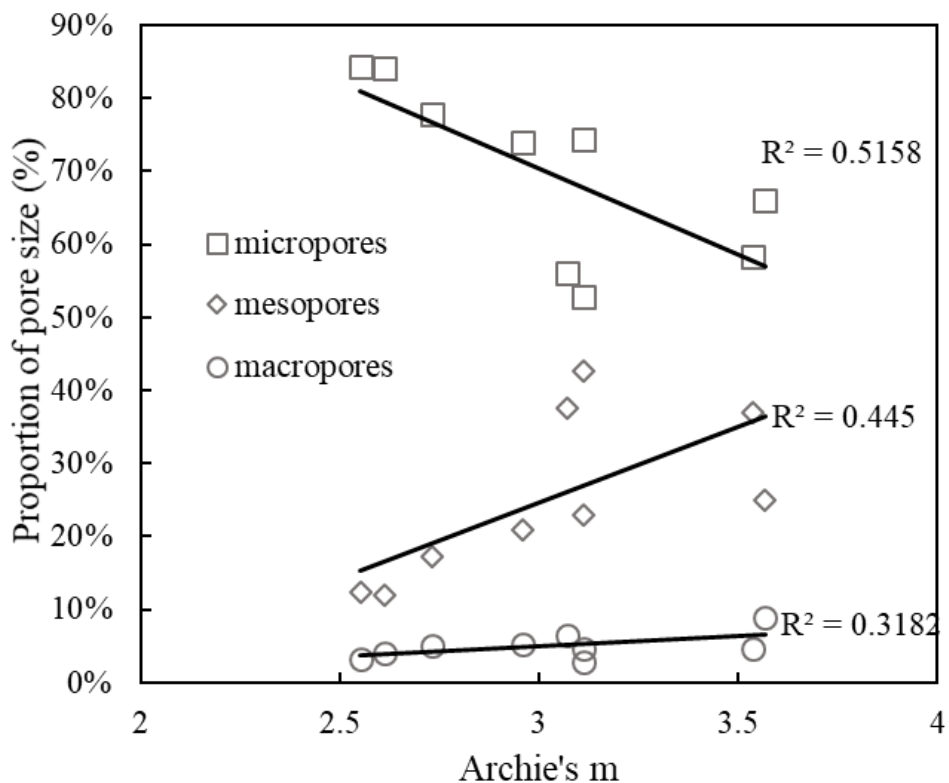


**Figure 6.4** Correlations between the proportion of micropores, mesopores and macropores with Archie's  $m$ .

### 6.3.3 Total porosity and effective porosity based cementation exponent

Figure 6.5 compares the fitted trend lines of Archie cementation exponent  $m$  for samples Th24, Th25, and Th28 based on the NMR total porosities and effective porosities (Figure 4.9). The Archie cementation exponent calculated by total porosity (4) expressed as a function of confining pressure:  $mT = (2.811)P^{0.012}$ , and the Archie cementation exponent calculated by effective porosity (mE) expressed as  $mE = (2.483)P^{0.011}$ . Noticeably, the confining pressure,  $P$ , is at the experimental conditions with no pore pressure applied, which is the effective pressure by its petrophysical meaning. In formation evaluation cases, with the existence of pore pressure, effective pressure instead of confining pressure should be considered when using these equations. Also, the variation of Archie's  $m$  under low salinity cases as discussed in Chapter 5 is not considered for two reasons: (1) the CEC effects cannot be neglect under low salinity cases; (2) the electrical contribution of dead-end pores at low salinity cases is not relevant to Archie's  $m$ , which is originally defined to describe the pore structures of the effective pores. Due to the limited understanding of the surface conductive mechanism in shale, Archie(mE) and Archie(mT) should be used differently based on the models and their petrophysical meanings. Indeed, if one is using a water saturation equation with total porosity as input then Archie(mT) needs to be used and in the case of using effective porosity then Archie(mE) needs to be used in the equation.

If we think surface conductivity share the conductive channels with pore water, surface conductivity can be regarded as a part of pore water conductivity. This case fits the classic Archie equation model can be expressed as follow:

$$\sigma = (\sigma_w + \sigma_s)/F = \Phi^m(\sigma_w + \sigma_s) \quad (7.1)$$

Where  $\sigma$  is rock conductivity in S/m,  $\sigma_w$  is pore water conductivity in S/m,  $\sigma_s$  is the surface conductivity in S/m. Noticeably, the applied Archie's  $m$  should couple with corresponding porosities. For example, by applying Archie(mT) should use total porosity ( $\Phi_t$ ) meaning that all the pores contribute to the conductivity. While applying Archie(mE) should use effective porosity ( $\Phi_e$ ) meaning that only effective pores contribute to the conductivity

However, if we believe the conductive channels of surface conductivity differ from pore water, the classic Archie equation should only be capable to indicated the pore water electrical contribution and the surface conductivity should be considered separately as fellow:

$$\sigma = \frac{1}{F} \sigma_w + \sigma_s = \Phi^m \sigma_w + \sigma_s \quad (7.2)$$

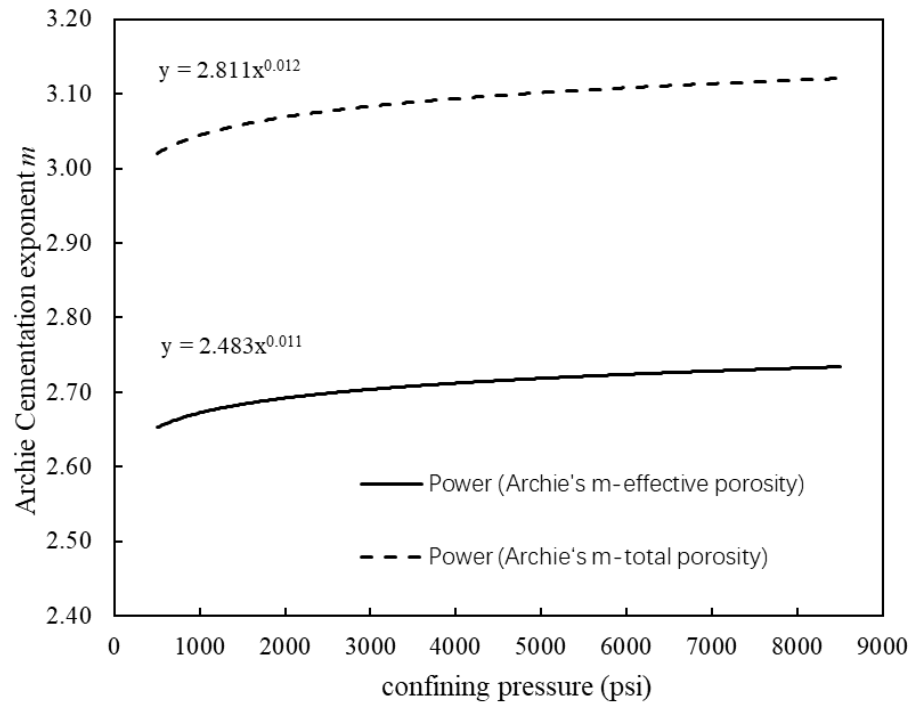


**Figure 6.5** The Archie cementation exponent derived based on total porosities shows higher values than those calculated by effective porosities in Figure 4.9. Either of these calculated  $m$  values can be used depending on what type of porosity (total or effective) has been used for the water saturation calculation.

### 6.3.4 Water saturation (SW) calculation

Figure 6.6 analysed the water saturation of Theia-1 from the depth ranges 900m to 1600m. The confining pressure was calculated based on previous work ([Bailey and Henson, 2019](#)) on the same basin ranging from 1240psi (900m) to 2930psi (1600m). The varying confining pressure was put into the equations shown in Figure 6.5 to calculate Archie-mT and Archie-mE. For the well-log data, total porosity (PHIT) calculated from neutron density logs. Effective porosity (PHIE) is based on defining the CBW from its corresponding clay content as discussed in Chapter 4.3 and shown in Table 2.2 (3% CBW for the rocks with 60% clay contents). SwT-S(mT) is the water saturation calculated by Simandoux equation with PHIT, Archie-mT,  $n=2$  and  $a=1$ , SwE-S(mE) is the water saturation calculated by Simandoux equation with PHIE, Archie-mE,  $n=2$ , and  $a=1$ . SwT-WS is the water saturation calculated by Waxman & Smits equation using Interactive Petrophysics (IP) with PHIT, Archie-mT,  $n=2$ , and  $Q_v$  calculated considering CEC=40 meg/100g for our illite-rich shale.

As seen in Figure 6.6, SwT-S(mT) and SwE-S(mE) almost overlapped each other presenting accurate water saturation estimation, which is supported by the water saturation measurement on the as-received samples by Waterford laboratories (yellow dots). SwT-WS show high SW than the results by the Simandoux equation at the same depth. The prediction of SwT-S(mT) and SwE-S(mE) conclude that the Archie-based Simandoux equation is acceptable for well-log interpretation. While Waxman & Smits equation show less accuracy than the Simandoux equation may result from our inaccurate  $Q_v$  simulation. Also, SwT-S(mT) and SwE-S(mE) show similar water saturation, indicating both PHIT and PHIE with corresponding Archie's cementation exponent (Archie(mT) and Archie(mE)) can be used in the formation evaluation.

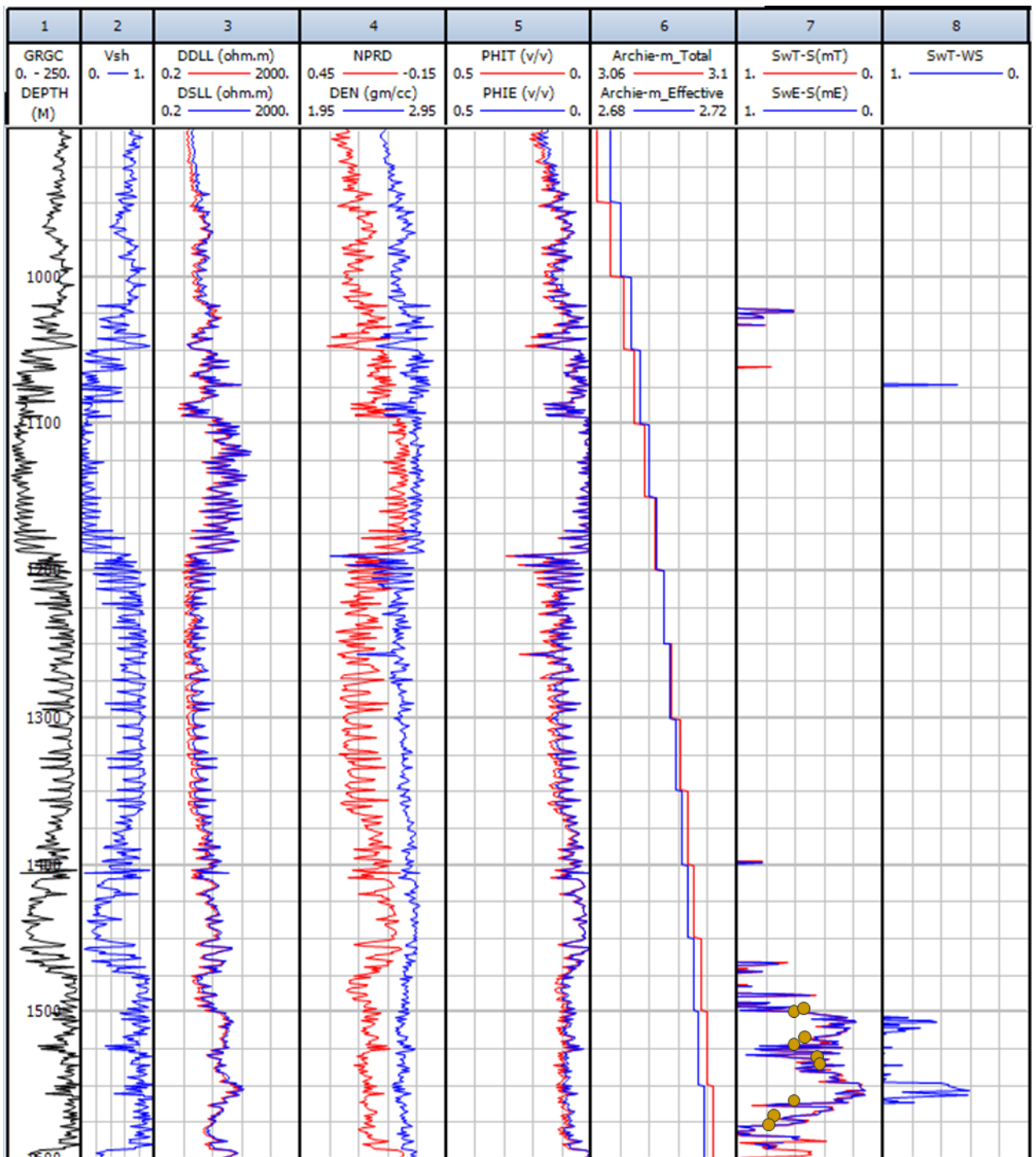


**Figure 6.6** The water saturation calculation by applying Archie cementation exponent on Simandoux and Waxman & Smits equations. The water saturation prediction of the Simandoux equation fits the measured water saturation from lab work (yellow dots).

---

## **Chapter 7**

## **Conclusion**

---

---

Faced with shortages of energy derived from conventional resources, unconventional natural resources have garnered increasing attention, especially shale gas. For shale gas exploration, well-log interpretation is the most effective method, within which resistivity logging is significant. However, the interpretation models applied for conventional formations turn out to be less effective for unconventional formations. To improve the resistivity models for shale formation, it is essential to investigate the mechanisms of electrical conduction in shale. In this study, we analysed the electrical resistivity and intrinsic formation factor by applying high salinity brine and derived the averaged Archie's  $m$  for shales from different formations. The results revealed that various factors control the electrical resistivity and Archie's  $m$  of shales. The controlling factors of confining pressure and pore water salinity were isolated and analysed to discuss their effects on Archie's cementation exponent. A prediction model for Archie's  $m$  under different confining pressure was developed, which makes it possible to estimate Archie's  $m$  in well-log interpretations of shale formations. Based on these experiments, supplemented with other tests (i.e. Rock-eval, XRD, etc.), the internal factors of shales on the electrical resistivities and Archie's factors were analysed, including organic matter contents, clay mineral composition, and pore-size distributions. The modified Archie cementation exponents considering the above factors were applied in models to predict the water saturation. Although our detailed conclusions were addressed in each chapter, here comes the highlighted conclusions and understanding about Archie's  $m$  in shale.

## 7.1 Conclusions of studies

Determination of Archie's exponent  $m$  in shales is challenging due to clay surface conductivity, which dominates the resistivity response and prevents proper measurement of the true resistivity. A new method for determining Archie exponent  $m$  in shale reservoirs was tested. After a thorough cleaning of the shales using toluene and methanol solvents to remove residual oil and salts, a very saline brine (250,000 ppm NaCl) was injected for two weeks under 2000 psi hydrostatic pressure to saturate the shales. The high salinity was designed to cancel the strong cationic exchange capacity from clays and so remove the surface conductivity from clays. Nuclear magnetic resonance (NMR) was used to check the development of microfractures, which was found to be negligible (< 5%), and to record the effective porosity used to compute Archie's  $m$  exponent. After the saturation, the resistivity of the shales was measured under atmospheric conditions (including 50 psi axial pressure for better sample–electrode surface contact) and under reservoir conditions (2800 psi confining and axial pressures) for the comparison. The averaged computed Archie's  $m$

exponent was found at 2.48 under ambient conditions and increases to 2.70 under reservoir conditions using formation factor  $F$  - porosity  $\Phi$  log-log method.

Shales from the Ordovician Goldwyer Formation in the Canning Basin (Australia) were selected for laboratory stress sensitivity measurements of electrical resistivity, porosity and pore-size distribution, as they have very homogeneous clay content at 20–46% illite. Laboratory NMR and electrical resistivity tools were used under controlled confining pressure and shale hydration state to help accurately record the effective porosity (i.e. total porosity without clay-bound water (CBW) porosity) and then compute Archie's cementation exponent  $m$  under reservoir conditions. Micropores (including CBW) are the dominant pore size in the Goldwyer shale formation. The small pore size of CBW and the strong paramagnetic clay signal in shales render accurate measurement of absolute CBW porosity from the NMR 2 MHz apparatus challenging. It is recommended absolute CBW porosity measurement be performed using sample mass change between dried shale at 60°C and fully dried sample at 105°C. Stress-sensitive electrical properties should be determined for shales at no less than 500 psi since the induced microfractures from reservoir stress relaxation, sample handling and cleaning processes are fully closed at 500 psi confining pressure. Mesopores/macropores are particularly sensitive to confining pressure range from 500 to 3500 psi due to pore size reduction. Beyond 3500 psi, the pore size change is negligible. Residual oil within the samples increases the rock resistivity but does not affect the pore-size distribution under different confining pressures. The variation in shale resistivity at different confining pressures appears to correlate with the closure of microfractures below 500 psi (strong and fast resistivity response), followed by the mesopores/macropores size reduction at 500–3500psi. Above 3500 psi, the few remaining compliant pores and pore-throat reduction slowly change the resistivity/Archie's  $m$  responses. Plastic/brittle regimes are not yet reached at 8500 psi confining pressure with respect to the observed steady slow increase of resistivity with pressure. Archie's  $m$  stress sensitivity shows a similar trend among the tested samples. An empirical formula is developed to predict Archie's  $m$  under different reservoir pressures for cleaned shales as:  $m_P = (2.483)P^{0.011}$  with pressure  $P$  in psi.

The sample collections containing carbonate-rich shale, quartz-rich shale and clay-rich shale were dried and resaturated at various salinities (35 g/l, 50 g/l, 70 g/l, 120 g/l and 250 g/l) before measuring the NMR and electrical conductivity of fully saturated samples at 2800 psi confining pressure. The electrical conductivity response at increasing pore water salinity shows concave trends; the formation factor and Archie's  $m$  correspondingly show similar but reversed trends under the calculation. This phenomenon is a result of the suppression of CEC effects and the shifting of

---

the conductive channel. The changes of the conductive channel that lead to the variation in formation factor and surface formation factor outweigh the effects of CEC at low salinities, as indicated by the lower rock conductivity versus the extended trend line at high salinity states. CEC thus may not be the main reason Archie's  $m$  in shale differs from the standard cementation exponent, given the observation that  $m$  does not vary much at different pore water salinities (0.1–0.15).

The electrical resistivities and Archie's  $m$  test under different samples are comprehensively compared with the results of XRD, Rock-eval, and NMR. We did not find a strong correlation between clay mineral contents and Archie's  $m$ . While a higher quartz component shows lower Archie's  $m$ , explained as the increasing pore structure complexity with lower quartz proportion. The electrical resistivity of organic matter relates to its maturity. The organic matter in Encounter's samples is believed to be more mature and less resistive than Theia's based on the Tmax from Rock-eval. Also, better development of organic pores in micropore size leads to higher micropore proportion in Encounter's samples. The higher proportion of micropores decrease the pore tortuosity as well as Archie's  $m$  while macropores and mesopores do the opposite. The derived  $m$  of Encounter's samples may be underestimated due to the conductive nature of mature organic matters.

The cementation exponent  $m$  derived on both total porosity( $mT$ ) and effective porosity( $mE$ ) was applied to the Archie equation, the Simandoux and Waxman & Smits equations expressed as  $mT = (2.811)P^{0.012}$  and  $mE = (2.483)P^{0.011}$  respectively. A less accurate water saturation prediction was found by applying the Waxman & Smits equation on well log interpretation software IP. On the contrary, the same input parameters work well in the Simandoux equation.

---

## 7.2 Recommendations for future research

Given the complexity of shale's petrophysical properties and the controlling factors for its electrical resistivity, additional parameters need to be investigated for a better understanding of the shale electrical properties, and more studies are needed for shale samples with various composition.

- The electrical resistivity of illite-rich samples was investigated in this study under various confining pressures and pore water salinities. Although quartz-rich and carbonate-rich shale were investigated and showed similar variation trends, the lower Archie's  $m$  data requires more studies to verify and to further explain the differences.
- To derive the effective porosities for shale samples, the CBW volume needs to be accurately identified. This study applied and compared the NMR methods and saturation methods for the CBW calculation; however, these need to be further tested given the low resolution of NMR for short relaxation times and the potential for manual error in saturation methods.
- The confining pressure effects show microfractures are maximally closed under 500 psi, but we do not know exactly which range of confining pressure is sufficient for fracture closure. More precise NMR tests are needed to resolve this problem and eventually improve the predicted model of Archie's  $m$  in this study.
- The confining pressure effects on Archie's  $m$  were investigated up to 8500psi without damage to the shale samples. A lower increase was found for Archie's  $m$  beyond 3500 psi. We concluded these changes result from the closure of the pore throat, based on NMR data and previous references; however, more evidence is needed for a solid conclusion and similar tests may produce different data in other shales.
- Our study reveals the changes in rock conductivity and Archie's parameters from seawater salinity to super-high salinity. Although the cementation exponent calculated by intrinsic formation factor at superhigh salinity was not greatly different from that calculated by apparent formation factor at seawater salinity, exactly how the apparent formation factor changes require further study.
- Our study was not designed to measure the effects of pore water salinities as low as iso-conductivity (0.09 S/m) due to concerns about sample damage during multiple re-drying

---

and re-saturation. For the same reason, we did not set sufficient tests for high salinity to derive the intrinsic formation factor. Therefore, how exactly rock conductivity changes at different pore water salinity, and whether CEC effects produce similar changes for shale as for other types of rock around iso-conductivity requires more study.

---

## References

- Abdassah, D., Permadi, P., Sumantri, Y. and Sumantri, R., 1998. Saturation exponent at various wetting condition: fractal modeling of thin-sections. *Journal of Petroleum Science and Engineering*, 20(3): 147-154.
- Al Hinai, A., Rezaee, R., Esteban, L. and Labani, M., 2014. Comparisons of pore size distribution: a case from the Western Australian gas shale formations. *Journal of Unconventional Oil and Gas Resources*, 8: 1-13.
- Alreshedan, F. and Kantzas, A., 2016. Sensitivity Analysis of the Effect of Pore Structure and Geometry on Petrophysical and Electrical Properties of Tight Media: Random Network Modeling. *Journal of Petroleum Science and Technology*, 6(1): 28-45.
- Archie, G.E., 1942. The Electrical Resistivity Log as an Aid in Determining Some Reservoir Characteristics. SPE-942054-G, 146(01): 54-62.
- Bailey, A.H. and Henson, P., 2019. Variation of vertical stress in the onshore Canning Basin, Western Australia. *The APPEA Journal*, 59(1): 364-382.
- Bernabe, Y., 1991. Pore geometry and pressure dependence of the transport properties in sandstones. *Geophysics*, 56(4): 436-446.
- Beti, D.R. and Ring, T.A., 2019. Programmed Temperature Pyrolysis: Alterations to the Standard Method, *Encyclopedia of Petroleum Geoscience*. Springer International Publishing, pp. 1-12.
- Bohác, P., Delavernhe, L., Zervas, E., Königer, F., Schuhmann, R. and Emmerich, K., 2019. Cation exchange capacity of bentonite in a saline environment. *Applied Geochemistry*, 100: 407-413.
- Bouton, J.C., Drack, E.D., Gardner, J.S. and Prammer, M.G., 1996. Measurements Of Clay-bound Water And Total Porosity By Magnetic Resonance Logging. SPWLA-1996-v37n6a3, 37(06): 22.
- Carr, H.Y. and Purcell, E.M., 1954. Effects of Diffusion on Free Precession in Nuclear Magnetic Resonance Experiments. *Physical Review*, 94(3): 630-638.
- Carroll, D., 1959. Ion exchange in clays and other minerals. *Geological Society of America Bulletin*, 70(6): 749-779.
- Carvajal-Ortiz, H. and Gentzis, T., 2018. Geochemical screening of source rocks and reservoirs: The importance of using the proper analytical program. *International Journal of Coal Geology*, 190: 56-69.
- Chakraborty, N., Karpyn, Z.T., Liu, S. and Yoon, H., 2017. Permeability evolution of shale during spontaneous imbibition. *Journal of Natural Gas Science and Engineering*, 38: 590-596.
- Cherubini, A., Garcia, B., Cerepi, A. and Revil, A., 2019. Influence of CO<sub>2</sub> on the Electrical Conductivity and Streaming Potential of Carbonate Rocks. *Journal of Geophysical Research: Solid Earth*, 124(10): 10056-10073.
- Chiu, Y.C., Huang, L.N., Uang, C.M. and Huang, J.F., 1990. Determination of cation exchange capacity of clay minerals by potentiometric titration using divalent cation electrodes. *Colloids and Surfaces*, 46(2): 327-337.
- Clarkson, C.R., Solano, N., Bustin, R.M., Bustin, A., Chalmers, G., He, L., Melnichenko, Y.B., Radliński, A. and Blach, T.P., 2013. Pore structure characterization of North American shale gas reservoirs using USANS/SANS, gas adsorption, and mercury intrusion. *Fuel*, 103: 606-616.
- Clavier, C., Coates, G. and Dumanoir, J., 1984. Theoretical and experimental bases for the dual-water model for interpretation of shaly sands. SPE-1863-A, 24(02): 153-168.

- 
- Clerke, E.A. and Martin, P., 1994. Absolute  $q_v$ : cost effective Juhasz correlations for shaly sand evaluation from integrated analysis of multiple lab measurements, SPWLA 35th Annual Logging Symposium. Society of Petrophysicists and Well-Log Analysts.
- Comisky, J.T., Santiago, M., McCollom, B., Buddhala, A. and Newsham, K.E., 2011. Sample size effects on the application of mercury injection capillary pressure for determining the storage capacity of tight gas and oil shales, Canadian unconventional resources conference. Society of Petroleum Engineers.
- Coperey, A., Revil, A., Abdulsamad, F., Stutz, B., Duvillard, P.A. and Ravanel, L., 2019. Low-Frequency Induced Polarization of Porous Media Undergoing Freezing: Preliminary Observations and Modeling. *Journal of Geophysical Research: Solid Earth*, 124(5): 4523-4544.
- Dashtian, H., Yang, Y. and Sahimi, M., 2015. Nonuniversality of the Archie exponent due to multifractality of resistivity well logs. *Geophysical Research Letters*, 42(24): 10,655-10,662.
- David, E. and Zimmerman, R.W., 2012. Pore structure model for elastic wave velocities in fluid-saturated sandstones. *Journal of Geophysical Research: Solid Earth*, 117(B7).
- Delle Piane, C., Bourdet, J., Josh, M., Clennell, M.B., Rickard, W.D., Saunders, M., Sherwood, N., Li, Z., Dewhurst, D.N. and Raven, M.D., 2018. Organic matter network in post-mature Marcellus Shale: Effects on petrophysical properties. *AAPG Bulletin*, 102(11): 2305-2332.
- Dewhurst, D.N., Piane, C., Esteban, L., Sarout, J., Josh, M., Pervukhina, M. and Clennell, M.B., 2018. Microstructural, geomechanical, and petrophysical characterization of shale caprocks, Geological carbon storage. Wiley Online Library, pp. 1-30.
- Dillinger, A. and Esteban, L., 2014. Experimental evaluation of reservoir quality in Mesozoic formations of the Perth Basin (Western Australia) by using a laboratory low field Nuclear Magnetic Resonance. *Marine and Petroleum Geology*, 57: 455-469.
- Doveton, J.H., 2014. Principles of mathematical petrophysics, 9. Oxford University Press, USA.
- Dunn, K.-J., Bergman, D.J. and LaTorraca, G.A., 2002. Nuclear magnetic resonance: Petrophysical and logging applications. Elsevier.
- Dvorkin, J., Mavko, G. and Nur, A., 1995. Squirt flow in fully saturated rocks. *Geophysics*, 60(1): 97-107.
- Ellis, D.V. and Singer, J.M., 2007. Well logging for earth scientists, 692. Springer.
- Espitalié, J., Laporte, J.L., Madec, M., Marquis, F., Leplat, P., Paulet, J. and Boutefeu, A., 1977. Méthode rapide de caractérisation des roches mères, de leur potentiel pétrolier et de leur degré d'évolution. *Rev. Inst. Fr. Pét.*, 32(1): 23-42.
- Fayyaz, K., Jafary, S., Bakhshi, P. and Madani, M., 2019. Accurate prediction of electrical conductivity of ionic liquids+ propylene carbonate binary mixtures. *Journal of Molecular Liquids*, 279: 400-410.
- Fertl, W.H., 1975. Shaly Sand Analysis In Development Wells, SPWLA 16th Annual Logging Symposium.
- Fertl, W.H. and Chilingarian, G.V., 1990. Type and distribution modes of clay minerals from well logging data. *Journal of Petroleum Science and Engineering*, 3(4): 321-332.
- Firdaus, G., 2015. Laboratory Measurements of Electrical Resistivity of Kerogen in Organic-Rich Mudrocks. Master's thesis, Texas A & M University.
- Fleury, M., Kohler, E., Norrant, F., Gautier, S., M'Hamdi, J. and Barré, L., 2013. Characterization and quantification of water in smectites with low-field NMR. *The Journal of Physical Chemistry C*, 117(9): 4551-4560.
- Fleury, M. and Romero-Sarmiento, M., 2016. Characterization of shales using T1–T2 NMR maps. *Journal of Petroleum Science and Engineering*, 137: 55-62.
- Foley, I., Farooqui, S. and Kleinberg, R., 1996. Effect of paramagnetic ions on NMR relaxation of fluids at solid surfaces. *Journal of Magnetic Resonance, Series A*, 123(1): 95-104.

- 
- Folk, R.L., 1974. Petrology of sedimentary rocks: Hemphill Pub. Co., Austin, Texas, 63.
- Friedman, S.P., 2005. Soil properties influencing apparent electrical conductivity: a review. *Computers and electronics in agriculture*, 46(1-3): 45-70.
- Ghorbani, A., Gailler, L.-S., Gresse, M., Cluzel, N., Panwar, N. and Sharma, R., 2018. Electrical conductivity and induced polarization investigations at Kilauea volcano, Hawai'i. *Journal of Volcanology and Geothermal Research*, 368.
- Han, M., Fleury, M. and Levitz, P., 2007. Effect of the pore structure on resistivity index curves, *International Symposium of the Society of Core Analysts*. Society of Core Analysts Canada.
- Han, T., 2018. An effective medium approach to modelling the pressure-dependent electrical properties of porous rocks. *Geophysical Journal International*, 214(1): 70-78.
- Han, T., Best, A.I., Sothcott, J. and MacGregor, L.M., 2011. Pressure effects on the joint elastic-electrical properties of reservoir sandstones. *Geophysical Prospecting*, 59(3): 506-517.
- Hendershot, W., Lalonde, H. and Duquette, M., 1993. Ion exchange and exchangeable cations. *Soil sampling and methods of analysis*, 19: 167-176.
- Hill, H.J., Klein, G.E., Shirley, O.J., Thomas, E.C. and Waxman, W.H., 1979. Bound Water In Shaly Sands - Its Relation To Q And Other Formation Properties. SPWLA-1979-vXXn3a1, 20(03): 17.
- Hu, Q., Zhang, Y., Meng, X., Li, Z., Xie, Z. and Li, M., 2017. Characterization of micro-nano pore networks in shale oil reservoirs of Paleogene Shahejie Formation in Dongying Sag of Bohai Bay Basin, East China. *Petroleum Exploration and Development*, 44(5): 720-730.
- Jackson, P.D., Smith, D.T. and Stanford, P.N., 1978. RESISTIVITY-POROSITY-PARTICLE SHAPE RELATIONSHIPS FOR MARINE SANDS. *Geophysics*, 43(6): 1250-1268.
- Jing, X., Daltaban, T. and Archer, J., 1989. Experimental measurements on the effects of pressure and temperature on electric properties of natural and synthetic rocks, *ISRM International Symposium*. International Society for Rock Mechanics and Rock Engineering.
- Jing, X.D., Archer, J.S. and Daltaban, T.S., 1992. Laboratory study of the electrical and hydraulic properties of rocks under simulated reservoir conditions. *Marine and Petroleum Geology*, 9(2): 115-127.
- Johnson, D.L., Plona, T.J. and Kojima, H., 1986. Probing porous media with 1st sound, 2nd sound, 4th sound and 3rd sound. *Physics and Chemistry of Porous Media*, 2: 243-277.
- Johnson, D.L. and Sen, P.N., 1988. Dependence of the conductivity of a porous medium on electrolyte conductivity. *Physical Review B*, 37(7): 3502-3510.
- Johnston, D.H., 1987. Physical properties of shale at temperature and pressure. *GEOPHYSICS*, 52(10): 1391-1401.
- Jones, P.J., Al-Shafei, E.N., Halpern, H.I., Al-Dubaisi, J.M., Ballay, R.E. and Funk, J.J., 2004. Pyrolytic oil-productivity index method for predicting reservoir rock and oil characteristics. Google Patents.
- Jones, P.J. and Tobey, M.H., 1999. Pyrolytic oil-productivity index method for characterizing reservoir rock. Google Patents.
- Josh, M., 2014. Dielectric permittivity: A petrophysical parameter for shales. *Petrophysics*, 55(04): 319-332.
- Josh, M., Clennell, B., Cauchefert, M. and Han, T., 2016. Dielectric permittivity and anisotropy of intact multi-saturated organic shales, SPWLA 57th Annual Logging Symposium (Reykjavik 25-29 June 2016), pp. 1-14.
- Josh, M., Delle Piane, C., Esteban, L., Bourdet, J., Mayo, S., Pejčić, B., Burgar, I., Luzin, V., Clennell, M.B. and Dewhurst, D.N., 2019. Advanced laboratory techniques characterising solids, fluids and pores in shales. *Journal of Petroleum Science and Engineering*, 180: 932-949.

- 
- Josh, M., Esteban, L., Delle Piane, C., Sarout, J., Dewhurst, D.N. and Clennell, M.B., 2012. Laboratory characterisation of shale properties. *Journal of Petroleum Science and Engineering*, 88-89: 107-124.
- Ju, Y., Sun, Y., Tan, J., Bu, H., Han, K., Li, X. and Fang, L., 2018. The composition, pore structure characterization and deformation mechanism of coal-bearing shales from tectonically altered coalfields in eastern China. *Fuel*, 234: 626-642.
- Kadkhodaie, A. and Rezaee, R., 2016. A new correlation for water saturation calculation in gas shale reservoirs based on compensation of kerogen-clay conductivity. *Journal of Petroleum Science and Engineering*, 146: 932-939.
- Kahr, G. and Madsen, F.T., 1995. Determination of the cation exchange capacity and the surface area of bentonite, illite and kaolinite by methylene blue adsorption. *Applied Clay Science*, 9(5): 327-336.
- Kaselow, A. and Shapiro, S.A., 2004. Stress sensitivity of elastic moduli and electrical resistivity in porous rocks. *Journal of Geophysics and Engineering*, 1(1): 1-11.
- Kausik, R., Fellah, K., Rylander, E., Singer, P.M., Lewis, R.E. and Sinclair, S.M., 2016. NMR relaxometry in shale and implications for logging. *Petrophysics*, 57(04): 339-350.
- Keelan, D.K. and McGinley, D.C., 1979. Application of cation exchange capacity in a study of the Shannon sand of Wyoming, SPWLA 20th Annual Logging Symposium. Society of Petrophysicists and Well-Log Analysts.
- Keller, G.V. and Carmichael, R., 1982. Electrical properties of rocks and minerals. *CRC handbook of physical properties of rocks*, 1: 217-293.
- Kennedy, W.D. and Herrick, D.C., 2012. Conductivity models for Archie rocks. *Geophysics*, 77(3): WA109-WA128.
- Kenyon, B., Kleinberg, R., Straley, C., Gubelin, G. and Morriss, C., 1995. Nuclear magnetic resonance imaging - technology for the 21st century. *Oilfield Review*, 7(3): 19-33.
- Khatibi, S., Ostadhassan, M., Xie, Z.H., Gentzis, T., Bubach, B., Gan, Z. and Carvajal-Ortiz, H., 2019. NMR relaxometry a new approach to detect geochemical properties of organic matter in tight shales. *Fuel*, 235: 167-177.
- Khilar, K.C. and Fogler, H.S., 1984. The existence of a critical salt concentration for particle release. *Journal of colloid and interface science*, 101(1): 214-224.
- King Jr, H.E., Eberle, A.P., Walters, C.C., Kliewer, C.E., Ertas, D. and Huynh, C., 2015. Pore architecture and connectivity in gas shale. *Energy & Fuels*, 29(3): 1375-1390.
- Koch, K. and Holliger, K., 2012. Is it the grain size or the characteristic pore size that controls the induced polarization relaxation time of clean sands and sandstones? *Water Resources Research*, 48.
- Komori, S., Kagiya, T., Takakura, S., Ohsawa, S., Mimura, M. and Mogi, T., 2013. Effect of the hydrothermal alteration on the surface conductivity of rock matrix: Comparative study between relatively-high and low temperature hydrothermal systems. *Journal of Volcanology and Geothermal Research*, 264: 164-171.
- Konoshonkin, D. and Parnachev, S., 2015. Existing approaches to tight rock laboratory petrophysics: a critical review, IOP Conference Series: Earth and Environmental Science. IOP Publishing, pp. 012042.
- Kuila, U., McCarty, D.K., Derkowski, A., Fischer, T.B. and Prasad, M., 2014. Total porosity measurement in gas shales by the water immersion porosimetry (WIP) method. *Fuel*, 117: 1115-1129.
- Kurniawan, F., 2005. Shaly sand interpretation using CEC-dependent petrophysical parameters.
- Labani, M.M., Rezaee, R., Saeedi, A. and Al Hinai, A., 2013. Evaluation of pore size spectrum of gas shale reservoirs using low pressure nitrogen adsorption, gas expansion and mercury porosimetry: A case study from the Perth and Canning Basins, Western Australia. *Journal of Petroleum Science and Engineering*, 112: 7-16.

- 
- Leveaux, J. and Poupon, A., 1971. Evaluation of water saturation in shaly formations. SPWLA-1985-vXXVIn1a2, 12(04).
- Li, H., Zhang, Z. and Shi, Y., 2016. New characterization on the petrophysical characteristics of tight sandstone reservoirs in Yanchang Formation Ordos Basin China. *Energy Exploration & Exploitation*, 34(6): 844-864.
- Liu, K., Ostadhassan, M., Zou, J., Gentzis, T., Rezaee, R., Bubach, B. and Carvajal-Ortiz, H., 2018. Nanopore structures of isolated kerogen and bulk shale in Bakken Formation. *Fuel*, 226: 441-453.
- Luffel, D. and Guidry, F., 1992. New core analysis methods for measuring reservoir rock properties of Devonian shale. SPE-20571-PA, 44(11): 1,184-1,190.
- Mahmood, S.M., Maerefat, N.L. and Chang, M.M., 1991. Laboratory Measurements of Electrical Resistivity at Reservoir Conditions. SPE-18179-PA, 6(03): 291-300.
- Malekimostaghim, E., Gholami, R., Rezaee, R., Asef, M.R., Zhong, Z. and Sarmadivaleh, M., 2019. A laboratory-based approach to determine Archie's cementation factor for shale reservoirs. *Journal of Petroleum Science and Engineering*, 183: 106399.
- McGlade, C., Speirs, J. and Sorrell, S., 2013. Unconventional gas – A review of regional and global resource estimates. *Energy*, 55: 571-584.
- McPhee, C., Reed, J. and Zubizarreta, I., 2015. *Core analysis: a best practice guide*. Elsevier.
- Mehana, M. and El-monier, I., 2016. Shale Characteristics Impact on Nuclear Magnetic Resonance (NMR) Fluid Typing Methods and Correlations. *Petroleum*, 2.
- Meiboom, S. and Gill, D., 1958. Modified Spin-Echo Method for Measuring Nuclear Relaxation Times. *Review of Scientific Instruments*, 29(8): 688-691.
- Moradzadeh, A. and Bakhtiari, M.R., 2011. Methods of water saturation estimation: Historical perspective. *Journal of Petroleum and Gas Engineering*, 3(2): 45-53.
- Musa, S.D., Zhonghua, T., Ibrahim, A.O. and Habib, M., 2018. China's energy status: A critical look at fossils and renewable options. *Renewable and Sustainable Energy Reviews*, 81: 2281-2290.
- Nabawy, B.S., Rochette, P. and Géraud, Y., 2010. Electric pore fabric of the Nubia sandstones in south Egypt: Characterization and modelling. *Geophysical Journal International*, 183(2): 681-694.
- Nikolaev, M.Y. and Kazak, A., 2019. Liquid saturation evaluation in organic-rich unconventional reservoirs: A comprehensive review. *Earth-Science Reviews*, 194.
- Niu, Q. and Revil, A., 2016. Connecting complex conductivity spectra to mercury porosimetry of sedimentary rocks. *GEOPHYSICS*, 81(1): E17-E32.
- Nottenburg, R.N., Rajeshwar, K., Rosenvold, R.J. and DuBow, J.B., 1979. Temperature and stress dependence of electrical and mechanical properties of Green River oil shale. *Fuel*, 58(2): 144-148.
- Patchett, J.G., 1975. An investigation of shale conductivity, SPWLA 16th Annual Logging Symposium. Society of Petrophysicists and Well-Log Analysts.
- Patnode, H.W. and Wyllie, M.R.J., 1950. The Presence of Conductive Solids in Reservoir Rocks as a Factor in Electric Log Interpretation. *Journal of Petroleum Technology*, 2(02): 47-52.
- Peters, K.E., 1986. GUIDELINES FOR EVALUATING PETROLEUM SOURCE ROCK USING PROGRAMMED PYROLYSIS. *American Association of Petroleum Geologists Bulletin*, 70(3): 318-329.
- Pimienta, L., Sarout, J., Esteban, L., David, C. and Clennell, M.B., 2017. Pressure-dependent elastic and transport properties of porous and permeable rocks: Microstructural control. *Journal of Geophysical Research: Solid Earth*, 122(11): 8952-8968.
- Pride, S., 1994. Governing equations for the coupled electromagnetics and acoustics of porous media. *Physical Review B*, 50(21): 15678-15696.

- 
- Quirein, J., Witkowsky, J., Truax, J.A., Galford, J.E., Spain, D.R. and Odumosu, T., 2010. Integrating core data and wireline geochemical data for formation evaluation and characterization of shale-gas reservoirs, SPE Annual Technical Conference and Exhibition. Society of Petroleum Engineers.
- Ramirez, M.O., 1990. Cation Exchange Capacity Data Derived from Well Logs, SPE Latin America Petroleum Engineering Conference. Society of Petroleum Engineers.
- Ramirez, T.R., Klein, J.D., Bonnie, R. and Howard, J.J., 2011. Comparative study of formation evaluation methods for unconventional shale gas reservoirs: Application to the Haynesville shale (Texas), North American Unconventional Gas Conference and Exhibition. Society of Petroleum Engineers.
- Rembert, F., Jougnot, D. and Guarracino, L., 2020. A fractal model for the electrical conductivity of water-saturated porous media during mineral precipitation-dissolution processes. *Advances in Water Resources*, 145: 103742.
- Revil, A., Cathles, L.M., Losh, S. and Nunn, J.A., 1998. Electrical conductivity in shaly sands with geophysical applications. *J Geophys Res-Sol Ea*, 103(B10): 23925-23936.
- Revil, A., Coperey, A., Deng, Y., Cerepi, A. and Seleznev, N., 2018. Complex conductivity of tight sandstones. *Geophysics*, 83(2): E55-E74.
- Revil, A. and Florsch, N., 2010. Determination of permeability from spectral induced polarization in granular media. *Geophysical Journal International*, 181(3): 1480-1498.
- Revil, A., Florsch, N. and Camerlynck, C., 2014. Spectral induced polarization porosimetry. *Geophysical Journal International*, 198(2): 1016-1033.
- Revil, A. and Glover, P., 1997. Theory of ionic-surface electrical conduction in porous media. *Physical review B*, 55(3): 1757.
- Revil, A., Kessouri, P. and Torres-Verdín, C., 2014. Electrical conductivity, induced polarization, and permeability of the Fontainebleau sandstone. *GEOPHYSICS*, 79(5): D301-D318.
- Revil, A., Le Breton, M., Niu, Q., Wallin, E., Haskins, E. and Thomas, D., 2017. Induced polarization of volcanic rocks–1. Surface versus quadrature conductivity. *Geophysical Journal International*, 208(2): 826-844.
- Revil, A., Soueid Ahmed, A. and Matthai, S., 2018. Transport of water and ions in partially water-saturated porous media. Part 3. Electrical conductivity. *Advances in Water Resources*, 121: 97-111.
- Revil, A., Wu, Y., Karaoulis, M., Hubbard, S.S., Watson, D.B. and Eppheimer, J.D., 2013. Geochemical and geophysical responses during the infiltration of fresh water into the contaminated saprolite of the Oak Ridge Integrated Field Research Challenge site, Tennessee. *Water Resources Research*, 49(8): 4952-4970.
- Rezaee, R., 2015. *Fundamentals of gas shale reservoirs*. John Wiley & Sons.
- Rezaee, R., Saedi, A. and Clennell, B., 2012. Tight gas sands permeability estimation from mercury injection capillary pressure and nuclear magnetic resonance data. *Journal of Petroleum Science and Engineering*, 88: 92-99.
- Romero-Sarmiento, M.-F., Pillot, D., Letort, G., Lamoureux-Var, V., Beaumont, V., Huc, A.-Y. and Garcia, B., 2016. New Rock-Eval method for characterization of unconventional shale resource systems. *Oil & Gas Science and Technology–Revue d'IFP Energies nouvelles*, 71(3): 37.
- Rouquerol, J., Avnir, D., Fairbridge, C., Everett, D., Haynes, J., Pernicone, N., Ramsay, J., Sing, K. and Unger, K., 1994. Recommendations for the characterization of porous solids (Technical Report). *Pure and applied chemistry*, 66(8): 1739.
- Ruhovets, N. and Fertl, W.H., 1982. Digital shaly sand analysis based on Waxman-Smiths model and log-derived clay typing. *The Log Analyst*, 23(03).
- Salem, H.S. and Chilingarian, G.V., 1999. The cementation factor of Archie's equation for shaly sandstone reservoirs. *Journal of Petroleum Science and Engineering*, 23(2): 83-93.

- 
- Scherdel, C., Reichenauer, G. and Wiener, M., 2010. Relationship between pore volumes and surface areas derived from the evaluation of N<sub>2</sub>-sorption data by DR-, BET-and t-plot. *Microporous and Mesoporous Materials*, 132(3): 572-575.
- Sebag, D., Garcin, Y., Adatte, T., Deschamps, P., Ménot, G. and Verrecchia, E.P., 2018. Correction for the siderite effect on Rock-Eval parameters: Application to the sediments of Lake Barombi (southwest Cameroon). *Organic Geochemistry*, 123: 126-135.
- Shapiro, S.A., 2003. Elastic piezosensitivity of porous and fractured rocks. *Geophysics*, 68(2): 482-486.
- Shapiro, S.A. and Kaselow, A., 2005. Porosity and elastic anisotropy of rocks under tectonic stress and pore-pressure changes. *Geophysics*, 70(5): N27-N38.
- Shumskayte, M. and Glinskikh, V., 2016. Relation of NMR parameters with specific surface and resistivity of shaly sandstone and siltstone samples: experimental study. *Russian Geology and geophysics*, 57(10): 1509-1514.
- Sigal, R.F., 2015. Pore-size distributions for organic-shale-reservoir rocks from nuclear-magnetic-resonance spectra combined with adsorption measurements. *SPE Journal*, 20(04): 824-830.
- Silva, M.L.d., Martins, J.L., Ramos, M.M. and Bijani, R., 2018. Estimation of clay minerals from an empirical model for Cation Exchange Capacity: An example in Namorado oilfield, Campos Basin, Brazil. *Applied Clay Science*, 158: 195-203.
- Simandoux, P., 1963. Dielectric measurements on porous media, application to the measurements of water saturation: study of behavior of argillaceous formations. *Revue de l'Institut Francais du Petrol*, 18(suppl): 93-215.
- Sohag, K., Taşkın, F.D. and Malik, M.N., 2019. Green economic growth, cleaner energy and militarization: Evidence from Turkey. *Resources Policy*, 63: 101407.
- Song, Y.-Q. and Kausik, R., 2019. NMR application in unconventional shale reservoirs—A new porous media research frontier. *Progress in nuclear magnetic resonance spectroscopy*, 112: 17-33.
- Soucémarianadin, L., Cécillon, L., Chenu, C., Baudin, F., Nicolas, M., Girardin, C. and Barré, P., 2018. Is Rock-Eval 6 thermal analysis a good indicator of soil organic carbon lability? – A method-comparison study in forest soils. *Soil Biology and Biochemistry*, 117: 108-116.
- Tahmasebi, P., 2018. Nanoscale and multiresolution models for shale samples. *Fuel*, 217: 218-225.
- Tan, M., Mao, K., Song, X., Yang, X. and Xu, J., 2015. NMR petrophysical interpretation method of gas shale based on core NMR experiment. *Journal of Petroleum Science and Engineering*, 136: 100-111.
- Tang, Z., Zhai, C., Zou, Q. and Qin, L., 2016. Changes to coal pores and fracture development by ultrasonic wave excitation using nuclear magnetic resonance. *Fuel*, 186: 571-578.
- Testamanti, N. and Rezaee, R., 2017. Determination of NMR T<sub>2</sub> cut-off for clay bound water in shales: A case study of Carynginia Formation, Perth Basin, Western Australia. *Journal of Petroleum Science and Engineering*, 149: 497–503.
- Tissot, B. and Welte, D., 1984. *Petroleum formation and occurrence*, Springer-Verlag. Berlin, Germany.[Google Scholar].
- Tod, S., 2002. The effects of stress and fluid pressure on the anisotropy of interconnected cracks. *Geophysical Journal International*, 149(1): 149-156.
- Tournassat, C., Chapron, Y., Leroy, P., Bizi, M. and Boulahya, F., 2009. Comparison of molecular dynamics simulations with triple layer and modified Gouy–Chapman models in a 0.1 M NaCl–montmorillonite system. *Journal of Colloid and Interface Science*, 339(2): 533-541.
- Verwer, K., Eberli, G.P. and Weger, R.J., 2011. Effect of pore structure on electrical resistivity in carbonates. *AAPG bulletin*, 95(2): 175-190.
- Wallace, W.E., 1965. Abnormal Subsurface Pressures Measured From Conductivity Or Resistivity Logs. *The Log Analyst*, 5(04).

- 
- Wang, J., Liu, M., Bentley, Y., Feng, L. and Zhang, C., 2018. Water use for shale gas extraction in the Sichuan Basin, China. *Journal of Environmental Management*, 226: 13-21.
- Wang, S., Javadpour, F. and Feng, Q., 2016. Confinement correction to mercury intrusion capillary pressure of shale nanopores. *Scientific reports*, 6(1): 1-12.
- Wang, W., Li, J., Fan, M. and Abedi, S., 2017. Characterization of electrical properties of organic-rich shales at nano/micro scales. *Marine and Petroleum Geology*, 86: 563-572.
- Wang, X., Zhang, B., He, Z., He, L., Yang, K., Huang, T., Luo, F., Tang, J. and Gan, L., 2016. Electrical properties of Longmaxi organic-rich shale and its potential applications to shale gas exploration and exploitation. *Journal of Natural Gas Science and Engineering*, 36: 573-585.
- Washburn, K.E., Anderssen, E., Vogt, S.J., Seymour, J.D., Birdwell, J.E., Kirkland, C.M. and Codd, S.L., 2015. Simultaneous Gaussian and exponential inversion for improved analysis of shales by NMR relaxometry. *Journal of Magnetic Resonance*, 250: 7-16.
- Waxman, M.H. and Smits, L.J.M., 1968. Electrical Conductivities in Oil-Bearing Shaly Sands. SPE-1863-A, 8(02): 107-122.
- Waxman, M.H. and Thomas, E.C., 1972. Electrical Conductivities in Shaly Sands - I. The Relation Between Hydrocarbon Saturation and Resistivity Index; II. The Temperature Coefficient of Electrical Conductivity, Fall Meeting of the Society of Petroleum Engineers of AIME. Society of Petroleum Engineers, San Antonio, Texas, pp. 41.
- Weller, A., Nordsiek, S. and Debschütz, W., 2010. Estimating permeability of sandstone samples by nuclear magnetic resonance and spectral-induced polarization. *Geophysics*, 75(6): E215-E226.
- Wong, P.-z., Koplik, J. and Tomanic, J., 1984. Conductivity and permeability of rocks. *Physical Review B*, 30(11): 6606.
- Worthington, P.F., 1985. The Evolution Of Shaly-sand Concepts In Reservoir Evaluation. *The Log Analyst*, 26(01).
- Worthington, P.F., 1993. The uses and abuses of the Archie equations, 1: The formation factor-porosity relationship. *Journal of Applied Geophysics*, 30(3): 215-228.
- Wu, Y., Tahmasebi, P., Lin, C., Ren, L. and Dong, C., 2019. Multiscale modeling of shale samples based on low- and high-resolution images. *Marine and Petroleum Geology*, 109: 9-21.
- Wyllie, M. and Rose, W.D., 1950. Some theoretical considerations related to the quantitative evaluation of the physical characteristics of reservoir rock from electrical log data. *Journal of Petroleum Technology*, 2(04): 105-118.
- Wyllie, M. and Southwick, P., 1954. An experimental investigation of the SP and resistivity phenomena in dirty sands. *Journal of Petroleum Technology*, 6(02): 44-57.
- Yale, D., 1984. Network modeling of flow storage and deformation in porous rocks: PhD's thesis. Stanford University, California.
- Yang, K., Connolly, P.R.J., Li, M., Seltzer, S.J., McCarty, D.K., Mahmoud, M., El-Husseiny, A., May, E.F. and Johns, M.L., 2020. Shale rock core analysis using NMR: Effect of bitumen and water content. *Journal of Petroleum Science and Engineering*, 195: 107847.
- Yuan, Y. and Rezaee, R., 2019. Comparative Porosity and Pore Structure Assessment in Shales: Measurement Techniques, Influencing Factors and Implications for Reservoir Characterization. *Energies*, 12: 2094.
- Yuan, Y., Rezaee, R., Al-Khdheawi, E.A., Hu, S.-Y., Verrall, M., Zou, J. and Liu, K., 2019. Impact of composition on pore structure properties in shale: implications for micro-/mesopore volume and surface area prediction. *Energy & Fuels*, 33(10): 9619-9628.
- Yuan, Y., Rezaee, R., Verrall, M., Hu, S.-Y., Zou, J. and Testmanti, N., 2018. Pore characterization and clay bound water assessment in shale with a combination of NMR and low-pressure nitrogen gas adsorption. *International Journal of Coal Geology*, 194: 11-21.

- 
- Yue, W.Z. and Tao, G., 2013. A new non-Archie model for pore structure: numerical experiments using digital rock models. *Geophysical Journal International*, 195(1): 282-291.
- Zhang, P., Lu, S., Li, J., Zhang, J., Xue, H. and Chen, C., 2017. Comparisons of SEM, Low-Field NMR, and Mercury Intrusion Capillary Pressure in Characterization of the Pore Size Distribution of Lacustrine Shale: A Case Study on the Dongying Depression, Bohai Bay Basin, China. *Energy & Fuels*, 31(9): 9232-9239.
- Zharbossyn, A., Berkinova, Z., Boribayeva, A., Yermukhambetova, A. and Golman, B., 2020. Analysis of Tortuosity in Compacts of Ternary Mixtures of Spherical Particles. *Materials*, 13(20): 4487.
- Zhong, Z., Rezaee, R., Esteban, L., Josh, M. and Feng, R., 2021. Determination of Archie's cementation exponent for shale reservoirs; an experimental approach. *Journal of Petroleum Science and Engineering*, 201: 108527.
- Zimmerman, R.W., 1990. *Compressibility of sandstones*. Elsevier.
- Zou, J., Rezaee, R. and Liu, K., 2017. Effect of Temperature on Methane Adsorption in Shale Gas Reservoirs. *Energy & Fuels*, 31(11): 12081-12092.
- Zou, J., Rezaee, R., Xie, Q., You, L., Liu, K. and Saedi, A., 2018. Investigation of moisture effect on methane adsorption capacity of shale samples. *Fuel*, 232: 323-332.

# Appendix

Paper: Determination of Archie's cementation exponent for shale reservoirs; an experimental approach. Journal of Petroleum Science and Engineering, Volume 201, June 2021

Zhiqi Zhong<sup>a</sup>, Reza Rezaee<sup>a</sup>, Lionel Esteban<sup>b</sup>, Matthew Josh<sup>b</sup>, Runhua Feng<sup>a</sup>

a. Western Australian School of Mines: Minerals, Energy and Chemical Engineering, Curtin University

b. CSIRO-Energy, Energy Resources, Perth, Australia

Name	conception and design	Acquisition of data & method	Data conditioning & manipulation	Analysis & statistical method	Interpretation & discussion	Final approval
Reza Rezaee	<input checked="" type="checkbox"/>	<input type="checkbox"/>	<input type="checkbox"/>	<input checked="" type="checkbox"/>	<input checked="" type="checkbox"/>	<input checked="" type="checkbox"/>
I acknowledge that these represent my contribution to the above research output. Signed						
Lionel Esteban	<input type="checkbox"/>	<input checked="" type="checkbox"/>	<input checked="" type="checkbox"/>	<input checked="" type="checkbox"/>	<input type="checkbox"/>	<input type="checkbox"/>
I acknowledge that these represent my contribution to the above research output. Signed						
Matthew Josh	<input type="checkbox"/>	<input type="checkbox"/>	<input type="checkbox"/>	<input checked="" type="checkbox"/>	<input checked="" type="checkbox"/>	<input type="checkbox"/>
I acknowledge that these represent my contribution to the above research output. Signed						
Runhua Feng	<input type="checkbox"/>	<input type="checkbox"/>	<input type="checkbox"/>	<input type="checkbox"/>	<input checked="" type="checkbox"/>	<input type="checkbox"/>
I acknowledge that these represent my contribution to the above research output. Signed						

Paper: The pressure dependence of Archie's cementation exponent for samples from the Ordovician Goldwyer shale formation in Australia.

Zhiqi Zhong<sup>a</sup>, Lionel Esteban<sup>b</sup>, Reza Rezaee<sup>a</sup>, Matthew Josh<sup>b</sup>, Runhua Feng<sup>a</sup>

a. Western Australian School of Mines: Minerals, Energy and Chemical Engineering, Curtin University

b. CSIRO-Energy, Energy Resources, Perth, Australia

Name	conception and design	Acquisition of data & method	Data conditioning & manipulation	Analysis & statistical method	Interpretation & discussion	Final approval
Lionel Esteban	<input checked="" type="checkbox"/>	<input type="checkbox"/>	<input type="checkbox"/>	<input checked="" type="checkbox"/>	<input checked="" type="checkbox"/>	<input type="checkbox"/>
I acknowledge that these represent my contribution to the above research output. Signed						
Reza Rezaee	<input type="checkbox"/>	<input checked="" type="checkbox"/>	<input checked="" type="checkbox"/>	<input checked="" type="checkbox"/>	<input type="checkbox"/>	<input checked="" type="checkbox"/>
I acknowledge that these represent my contribution to the above research output. Signed						
Matthew Josh	<input type="checkbox"/>	<input type="checkbox"/>	<input type="checkbox"/>	<input checked="" type="checkbox"/>	<input checked="" type="checkbox"/>	<input type="checkbox"/>
I acknowledge that these represent my contribution to the above research output. Signed						
Runhua Feng	<input type="checkbox"/>	<input type="checkbox"/>	<input type="checkbox"/>	<input type="checkbox"/>	<input checked="" type="checkbox"/>	<input type="checkbox"/>
I acknowledge that these represent my contribution to the above research output. Signed						

---

Paper: The salinity dependence of Archie's cementation exponent for shale reservoir

Zhiqi Zhong<sup>a</sup>, Reza Rezaee<sup>a</sup>, Matthew Josh<sup>b</sup>, Lionel Esteban<sup>b</sup>,

a. Western Australian School of Mines: Minerals, Energy and Chemical Engineering, Curtin University

b. CSIRO-Energy, Energy Resources, Perth, Australia

Name	conception and design	Acquisition of data & method	Data conditioning & manipulation	Analysis & statistical method	Interpretation & discussion	Final approval
Reza Rezaee	<input checked="" type="checkbox"/>	<input type="checkbox"/>	<input type="checkbox"/>	<input checked="" type="checkbox"/>	<input checked="" type="checkbox"/>	<input checked="" type="checkbox"/>
I acknowledge that these represent my contribution to the above research output. Signed						
Matthew Josh	<input type="checkbox"/>	<input checked="" type="checkbox"/>	<input checked="" type="checkbox"/>	<input checked="" type="checkbox"/>	<input type="checkbox"/>	<input type="checkbox"/>
I acknowledge that these represent my contribution to the above research output. Signed						
Lionel Esteban	<input type="checkbox"/>	<input type="checkbox"/>	<input type="checkbox"/>	<input checked="" type="checkbox"/>	<input checked="" type="checkbox"/>	<input type="checkbox"/>
I acknowledge that these represent my contribution to the above research output. Signed						

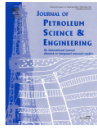
## B. Copyright Agreement

The Copyright Agreements between the journals and author to reuse the published papers in this thesis are listed as following



RightsLink

[Home](#) | [Help](#) | [Live Chat](#) | [Zhiqi Zhong](#)



**Determination of Archie's cementation exponent for shale reservoirs; an experimental approach**

Author: Zhiqi Zhong, Rezaee, Lionel Esteban, Matthew Josh, Runhua Feng

Publication: Journal of Petroleum Science and Engineering

Publisher: Elsevier

Date: June 2021

© 2021 Elsevier B.V. All rights reserved.

**Journal Author Rights**

Please note that, as the author of this Elsevier article, you retain the right to include it in a thesis or dissertation, provided it is not published commercially. Permission is not required, but please ensure that you reference the journal as the original source. For more information on this and on your other retained rights, please visit: <https://www.elsevier.com/about/our-business/policies/copyright#author-rights>

BACK
CLOSE WINDOW

© 2021 Copyright - All Rights Reserved | Copyright Clearance Center, Inc. | [Privacy statement](#) | [Terms and Conditions](#)  
Comments? We would like to hear from you. Email us at [customercare@copyright.com](mailto:customercare@copyright.com)

### GENERAL INFORMATION

Request ID	600048698	Request Date	21 Jul 2021
Request Status	Accepted	Price	0.00 AUD <span style="font-size: 0.8em; color: #0070C0;">?</span> <a href="#">Special Terms</a>

▼ **ALL DETAILS**

ISSN:	1086-055X	Publisher:	THE SOCIETY,
Type of Use:	Republish in a thesis/dissertation	Portion:	Chapter/article

### LICENSED CONTENT

Publication Title	SPE JOURNAL - RICHARDSON-	Country	United States of America
Author/Editor	SOCIETY OF PETROLEUM ENGINEERS (...)	Rightsholder	Society of Petroleum Engineers (SPE)
Date	01/01/1996	Publication Type	Journal

### REQUEST DETAILS

Page range(s)	38-56	Distribution	Worldwide
Total number of pages	18	Translation	Original language of publication
Format (select all that apply)	Electronic	Copies for the disabled?	No
Who will republish the content?	Author of requested content	Minor editing privileges?	No
Duration of Use	Life of current edition	Incidental promotional use?	No
Lifetime Unit Quantity	Up to 99,999	Currency	AUD
Rights Requested	Main product		

### NEW WORK DETAILS

Title	Assessment of Archie Parameters in S...	Institution name	Curtin University
Instructor name	Zhiqi Zhong	Expected presentation date	2021-07-21

### ADDITIONAL DETAILS

Order reference number	N/A	The requesting person / organization to appear on the license	Zhiqi Zhong
------------------------	-----	---	-------------

### REUSE CONTENT DETAILS

Title, description or numeric reference of the portion(s)	The Pressure Dependence of the Archi...	Title of the article/chapter the portion is from	Assessment of Archie Parameters in S...
Editor of portion(s)	Zhiqi Zhong	Author of portion(s)	SOCIETY OF PETROLEUM ENGINEERS (...)
Volume of serial or monograph	N/A	Publication date of portion	2021-07-21
Page or page range of portion	38-56		